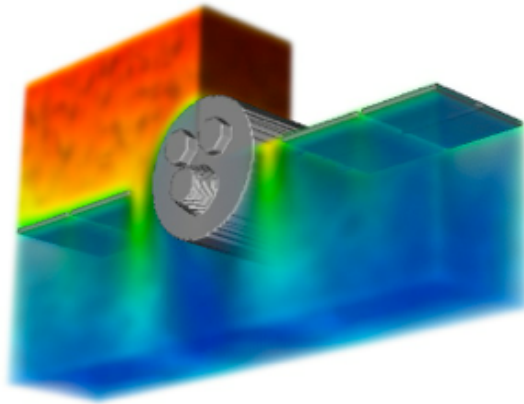# Faster-than-Realtime Electrostatic Force and Torque Modeling for SSA Applications

(Final Project Report)

Principal Investigators:

Hanspeter Schaub[1] (PI)
University of Colorado, Boulder, CO 80309-0431

October 14, 2018

[1]Professor, Glenn L. Murphy Chair, hanspeter.schaub@colorado.edu, (303) 492-2767

Table of Contents

Chapter 1

Award Administration

1.1 Project Overview

This 3-year research study completed completed successfully on Sept. 14, 2018. The goal was to research faster-than-realtime electrostatic force and torque models for prototype GEO spacecraft shapes through continued development of the Multi-Sphere-Method (MSM). SSA tracking and identification of passive space objects or debris requires accurate modeling of the associated astrodynamics. In the GEO regime objects naturally can charge to 10's of kilo-Volts, which can result in considerable charge accumulation. Interactions with the Earth's magnetic field will cause both translational and rotational perturbations. To improve long-term SSA tracking and identification of such objects, novel force modeling methods are required. Electrostatic fields can be evaluated through commercial finite element code, but such solutions can take minutes to evaluate. This project expands the recently introduced MSM modeling technique to obtain approximate electrostatic forces and torques many orders of magnitude faster than finite elements, at the cost of a reduced accuracy. However, this signifiant computational speed-up allows the new force models to be used in SSA propagators that need to track thousands of objects.

   The proposed work had 3 overarching research thrusts. First, MSM model development was enhanced to function on more general conducting shape prototypes than the existing cylinder model. This resulted in a new MSM setup routine that uses E-fields and is more robust and precise to develop. Further, a novel study was concluded how the method of moments method compares to the surface MSM method, and methods of moments can be used to create non-homogenous surface MSM methodologies. Finally, this thrust also created new analytical expansions of the electrostatic forces and torques called the Appropriate fidelity models. These are able to approximate the electrostatic interactions between multiple charged bodies with general shapes. Second, several GEO debris objects are expected to be flexible thermal blankets, and the MSM suitability to modeling deformable shapes is investigated. The MSM methodology has been expanded to include time varying space object shapes. Many vacuum chamber experiments were conducted in the third year to study the charged deflection of membranes and see how well the flexible MSM model can capture this motion. Third, the MSM methodology was expanded to consider hybrid conducting and dielectric surfaces. A comprehensive paper has been written that outlines how point charge models can be used to augment the MSM methodology to simulate surfaces that are either conducting or dielectric. On top of the modeling technique improvements, a study was completed on how the natural charging impacts lightweight orbital debris in the GEO regime. The conclusion was that while charging can have a measurable impact on the debris perturbations, it is very sensitive to the orientation making it very difficult to use charged astrodynamics to predict

actual perturbations. All proposed work tasks have been completed, and this report provides a final overview of the successful project studying faster than realtime electrostatic force and torque modeling.

1.2   Research Staff Support Over the 3 Project Years

The research grant supported both phd graduate researchers and undergraduate researchers over the years. The list below itemizes the students that were supported by this grant.

- Joseph Hughes, Ph.D. student. Joe has undergraduate degrees in aerospace engineering, physics and a minor in applied math. He is supported full-time on this project and has become my lead researcher on this grant. He has been on this project since the beginning, and worked full-time on this grant over the summer as well. He is leading the novel analytical electrostatic force and torque evaluation methods. Joe has interned at AFRL with the spacecraft charging group.

- Jordan Maxwell, Ph.D. student. Jordan started at CU as a graduate research assistant on August 1, 2016. He has a physics background and is earning a phd in aerospace engineering. He has extensive experience with vacuum chamber experiments and instrument development, and will be working on this research grants for the remaining project years. Jordan has interned at AFRL with the spacecraft charging group and won the Dr. Charles Stein Outstanding Scholar Award for his summer 2018 work.

- Philip Chow, former Ph.D. student. He was a first year Ph.D. student in my research and supported this project in the fall and spring. During the spring he decided that the phd track was not form him, and he left the project by the end of the spring to focus on his course work to achieve a MS degree.

- Christine Reilly, undergraduate researcher. She worked with Trevor as her advisor last academic year, and helped with some Matlab based validation software for the MSM models. In fact, Christine won the top DLA award last year with her presentation entitle "May the Electrostatic Force be With You: Charge Spacecraft Models."[1]

- Mahdi Ghanei, Undergraduate Researcher. Mahdi joined the AVS Lab as a Discovery Learning Apprentice in the fall of 2017. This is a program at CU where they support undergraduate researchers, and he helped Jordan with the development and running of the charged actuation experiments.

The next list contains students who supported the research represented in this report, but were not directly financially supported by this research grant. These students were supported by national fellowships or alternate funding and were interested in contributing to the work being performed.

- Trevor Bennett, Ph.D. student. He is supported through a separate NASA NSTRF fellowship, but provided part-time assistance as the MSM modeling of complex shapes is of interest in his dissertation work.

---

[1] http://hanspeterschaub.info/Papers/grads/ChristineReilly.pdf

- Kieran Wilson, a Ph.D. student who started in the fall of 2017. He is also interested in the charged astrodynamics research and was assigned to help Jordan with the complex simulation and experimental work.

- Miles Bengtson, a Ph.D. student who started in the fall of 2017. He has a NDSEG fellowship that covers his salary and came to my lab specifically to perform spacecraft charging experiments. He assisted with the setup and planning of the vacuum chamber experiments.

1.3   Associated Publications

The following comprehensive list contains the research grant related papers that have been created thus far, or are in progress.

1.3.1   Conference Papers

1. J. Hughes and H. Schaub, "Appropriate Fidelity Electrostatic Force Evaluation Considering A Range Of Spacecraft Separations," AAS Spaceflight Mechanics Meeting, Napa Valley, California, February 14–18, 2016. Paper No. 16-486.

2. P. Chow, J. Hughes and H. Schaub, "Automated Sphere Geometry Optimization For The Volume Multi-Sphere Method," AAS Spaceflight Mechanics Meeting, Napa Valley, California, February 14–18, 2016. Paper No. 16-472.

3. J. Hughes and H. Schaub, "Charged Geosynchronous Debris Perturbation Using Rapid Electromagnetic Force and Torque Evaluation," Advanced Maui Optical and Space Surveillance Technologies Conference, Maui, Hawaii, September 20–23, 2016.

4. J. Hughes and H. Schaub, "Spacecraft Electrostatic Force And Torque Expansions Yielding Appropriate Fidelity Measures,"AAS Spaceflight Mechanics Meeting, San Antonio, TX, Feb. 5–9, 2017.

5. G. Ingram, J. Hughes, T. Bennett, C. Reilly and H. Schaub, "Autonomous Volume Multi-Sphere-Model Development Using Electric Field Matching," AAS Spaceflight Mechanics Meeting, San Antonio, TX, Feb. 5–9, 2017.

6. J. Hughes and H. Schaub, "Rapid Charged Geosynchronous Debris Perturbation Modeling Of Electromagnetic Disturbances," AAS Spaceflight Mechanics Meeting, San Antonio, TX, Feb. 5–9, 2017.

7. J. Hughes and H. Schaub, "The Impact of Space Weather on GEO Space Debris Orbit Evolution," Space Weather Workshop, Broomfield, Colorado, May 1–5, 2017.

8. J. Hughes and H. Schaub, "Effects Of Charged Dielectrics On Electrostatic Force And Torque," 9th International Workshop on Satellite Constellations and Formation Flying, University of Colorado, Boulder, Colorado, June 19–21, 2017.

9. J. Maxwell and H. Schaub, "Applicability of the Multi-Sphere Method to Flexible One-Dimensional Conducting Structures," AAS/AIAA Astrodynamics Specialist Conference, Stevenson, WA, August 20–24, 2017

10. J. Hughes and H. Schaub, "Effects of Space Weather on Geosynchronous Electromagnetic Spacecraft Perturbations Using Statistical Fluxes," AGU Fall Meeting, New Orleans, Louisiana, December 11–15, 2017

11. J. Maxwell, K. Wilson and H. Schaub, "Multi-Sphere Method for Flexible Conducting Space Objects: Modeling and Experiments," AAS/AIAA Astrodynamics Specialist Conference, Snowbird, UT, August, 19–23, 2018.

12. J. Hughes and H. Schaub, "Rapid Modeling of Electrostatic Forces and Torques Considering Dielectrics," International Astronautical Congress, Bremen, Germany, October 1–5, 2018.

1.3.2 Journal Papers

- J. Hughes and H. Schaub, "Spacecraft Electrostatic Force and Torque Expansions Yielding Appropriate Fidelity Measures," Submitted to *Journal of Astronautical Sciences*.

- J. Hughes and **H. Schaub**, "Rapid Charged Geosynchronous Debris Perturbation Modeling of Electromagnetic Disturbances," *Journal of Astronautical Sciences*, Vol. 65, No. 2, 2018, pp. 135–156.
  doi:10.1007/s40295-017-0127-3

- G. Ingram, J. Hughes, T. Bennett, C. Reilly and H. Schaub, "Volume Multi-Sphere-Model Development Using Electric Field Matching," Submitted to *Journal of Astronautical Sciences* and passed review cycle.

- J. Hughes and H. Schaub, "Spacecraft Electrostatic Force and Torque Expansions Yielding Appropriate Fidelity Measures," Submitted to *Journal of Astronautical Sciences* for publication.

- J. Hughes and H. Schaub , "Space Weather Influence on Electromagnetic Geosynchronous Debris Perturbations Using Statistical Fluxes," *Space Weather*, Vol. 16, No. 4, 2018, pp. 391–405.
  doi:10.1002/2017SW00176

- J. Maxwell, K. Wilson and **H. Schaub**, "Multi-Sphere Method for Flexible Conducting Space Objects: Modeling and Experiments," *In preparation for AIAA Journal of Spacecraft and Rockets*

- J. Hughes and H. Schaub, "Heterogeneous Surface Multi-Sphere Models using Method of Moments Foundations," *In preparation for Journal of Astronautical Sciences*

- J. Hughes and H. Schaub, "Rapid Modeling of Electrostatic Forces and Torques Considering Dielectrics," *In preparation for Acta Astronautica*

Chapter 2

Technical Progress Reports

This chapter discusses the technical results achieved during the project.

2.1 Research Thrust 1: MSM Development

2.1.1 E-field based MSM Development

2.1.1.1 Multi-Sphere Method Background

MSM provides a computationally fast approximate model of a spacecraft's electrostatic properties for applications that require faster-than-realtime results. MSM solves for the force and torque on a conductor by first finding the charge on a number of virtual spheres placed within the body. The charge on the spheres is found by assuming all spheres are equipotential across a single space object and solving a linear system of equations. MSM divides into VMSM, which uses a small number of spheres placed within the *volume* of the conductor, and SMSM, which places a large number of spheres on the *surface* of the conductor. It is more difficult to generate VMSM models because the size and location of the spheres must be found using an optimizer; however, VMSM models are much faster to run once completed due to the much smaller number of sphere employed. In contrast, SMSM models are easier to set up because the sphere locations are specified, and the sphere size can be found by matching self capacitance, which is computed from commercial FEM software. Generally, SMSM models show higher accuracy when compared to FEM-generated force and torque data.[1] Although SMSM greatly reduces the effort required to create a MSM model for a given spacecraft geometry and increases the accuracy of the model, it comes at increased computational cost at runtime due to the large number of spheres.

Both the Volume Multi-Sphere Method and Surface Multi-Sphere Method represent a conducting object as N spheres, as shown in Figure 2.1. These methods only differ in the number, size and placement of the spheres used to represent the conductor. The MSM formulation currently assumes that the surface of the target craft or debris is perfectly conducting, which implies that all MSM spheres that constitute a model are equipotential.

The charge on each sphere, which may include multiple distinct spheres outside of the target model, is only a function of the sizes of the spheres in the complete model and their relative positions. Letting N_T be the total number of MSM spheres in a MSM model, computed as the sum of the number of spheres in the target model and the number of spheres outside the target model, all MSM spheres can approximated as point charges. The $N_T \times 1$ charge matrix, $\mathbf{q} = \begin{bmatrix} q_1 & q_2 & \dots & q_{N_T} \end{bmatrix}^T$, which contains the charge on each sphere of a MSM model, is related to the
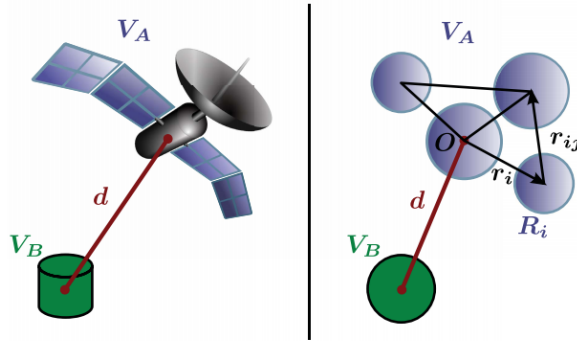
Figure 2.1: *Illustration of the MSM concept showing how two conducting space objects are decomposed into a series of body-fixed sphere with the same potential.*[2]

$N_T \times 1$ sphere voltage matrix $\mathbf{V} = \begin{bmatrix} V_1 & V_2 & \ldots & V_{N_T} \end{bmatrix}^T$ through Eq. (2.1)[3]

$$\mathbf{q} = \frac{1}{k_\text{c}} \left[C_\text{M} \right] \mathbf{V} \tag{2.1}$$

where $k_c = 1/4\pi\epsilon_0$ is the Coulomb constant, and the $N_T \times N_T$ matrix $\frac{1}{k_\text{c}} \left[C_\text{M} \right]$ is the Position Dependent Capacitance (PDC) matrix. For a general N_T sphere MSM model, the PDC matrix is difficult to produce; however, its inverse, the elastance matrix $[S]$, contains only functions of the sphere radii R_i and relative distances between spheres $r_{i,j}$. $[S]$ is formulated as shown in Eq. (2.2)[4]

$$[S] = k_\text{c} \begin{bmatrix} \frac{1}{R_1} & \frac{1}{r_{1,2}} & \cdots & \frac{1}{r_{1,N_T}} \\ \frac{1}{r_{2,1}} & \frac{1}{R_2} & \cdots & \frac{1}{r_{2,N_T}} \\ \vdots & \vdots & \ddots & \vdots \\ \frac{1}{r_{N_T,1}} & \frac{1}{r_{N_T,2}} & \cdots & \frac{1}{R_{N_T}} \end{bmatrix} \tag{2.2}$$

The charges, which lead to the force and torque, are found by solving the linear system. For an isolated conductor with a small number of spheres this can be done analytically,[5] but in the majority of cases it is done numerically. This computation is expensive if many spheres are used, and is the cause of decreased run-time performance when using the SMSM method.

The charge set $\mathbf{q}$ is calculated using Eq. (2.1). The charges, q_i, are used to calculate the electric field produced by the model, and forces and torques that an object model experiences subject to one or more external point charges. Denoting the position vector of an external point charge as $\mathbf{r}_k$ and the relative position vector of each MSM model sphere with respect to its center of mass as $\mathbf{r}_i$, the force, $\mathbf{F}$, and torque, $\mathbf{T_O}$, applied to the target model about its center of mass by all external spheres with charges q_k are given in Eqs. (2.3) and (2.4)[2]

$$\mathbf{F} = -k_\text{c} \sum_{k=1}^{M} q_k \sum_{i=1}^{N} \frac{q_i}{||\mathbf{r}_{i,k}||^3} \mathbf{r}_{i,k} \tag{2.3}$$

$$\mathbf{T_O} = -k_\text{c} \sum_{k=1}^{M} q_k \sum_{i=1}^{N} \frac{q_i}{||\mathbf{r}_{i,k}||^3} \mathbf{r}_i \times \mathbf{r}_{i,k} \tag{2.4}$$

where $\mathbf{r}_{i,k}$ is the relative position of the kth external sphere with respect to the ith internal MSM sphere as shown in Figure 2.1. Let N be the total number of spheres in the target model, while

M is the total number of spheres external to the target such that $N_T = N + M$. Adding arbitrary numbers of external spheres does not add to the complexity of MSM modeling because they can be appended to the charge and elastance matrices; however, doing so will increase computational burden–primarily due growing size of the elastance matrix, which always needs to be inverted. Whole MSM models can be appended when the calculation of force and torque between two complex geometries is desired. The electric field at any point exterior to the spheres of a MSM model is given by the superposition of the electric fields of each sphere, as shown in

$$\mathbf{E} = k_{\mathsf{c}} \sum_{i=1}^{N_T} \frac{q_i}{||\mathbf{r}_{i,l}||^3} \mathbf{r}_{i,l} \tag{2.5}$$

where l is a point of interest in the space outside of the MSM model spheres, and $\mathbf{r}_{i,l}$ is the relative position between the i-th MSM model sphere and l.

Prior VMSM model fitting methods minimize a cost function based upon the difference between the force and torque vectors predicted by a VMSM model and the force and torque vectors generated by commercial FEM software. One such cost function is given in Reference 5 by

$$J = \frac{100}{2L} \left(\sum_{l=1}^{L} \frac{||\mathbf{F}_{\mathsf{VMSM},l} - \mathbf{F}_{\mathsf{FEM},l}||}{||\mathbf{F}_{\mathsf{FEM},l}||} + \frac{||\mathbf{T}_{\mathsf{VMSM},l} - \mathbf{T}_{\mathsf{FEM},l}||}{||\mathbf{T}_{\mathsf{FEM},l}||} \right) \tag{2.6}$$

To alleviate far-field data noise effects in the optimization process, current methods utilize a self-capacitance constraint is proposed in Reference 5. Enforcing the VMSM model match the self capacitance of the target object ensures that the forces will match as the two objects get very far from each other. The self-capacitance C of a MSM model is given by[5]

$$C = \frac{Q}{V} = \frac{\sum_{i=1}^{N} q_i}{V} = \frac{1}{k_{\mathsf{c}}} \sum_{i=1}^{N} \sum_{j=1}^{N} (C_{\mathsf{M}})_{ij} \tag{2.7}$$

To enforce a self-capacitance constraint, the self-capacitance of the target geometry is calculated using FEM and the MSM model self-capacitance is matched to the FEM result– reducing the optimizer search space by one dimension. The capacitance matching can be accomplished analytically for simple models, or numerically for large models. Matlab's *fmincon* optimizer allows the self-capacitance constraint to be defined in a constraint function and enforced numerically.

2.1.1.2 Electric Field VMSM Model Fitting

2.1.1.2.1 *SMSM E-field Data Generation*

Using the current VMSM methodology, the sphere positions and radii are varied by an optimizer to best match force and torque data produced by a commercial FEM program.[2,3,5] This methodology requires significant hand-tuning of model parameters for a model that fits force and torque data accurately due to noisy FEM data in the far field, dependance on probe size, and convergence properties of the force and torque cost function. Recent work largely streamlines the process of generating VMSM models using ANSYS Maxwell 3D to generate numerical data.[5] The workflow for current VMSM model fitting starts with generating solid models for a target and probe geometry in FEM software and calculating accurate force and torque values between them at many relative positions. Self-capacitance of the target spacecraft is also calculated.

Generating the FEM truth data is by far the most time-consuming step. A complete sweep of locations for force and torque matching and validation may take hours and variations in accuracy

Weights: $\boldsymbol{w} = [w_C, w_M, w_D]$
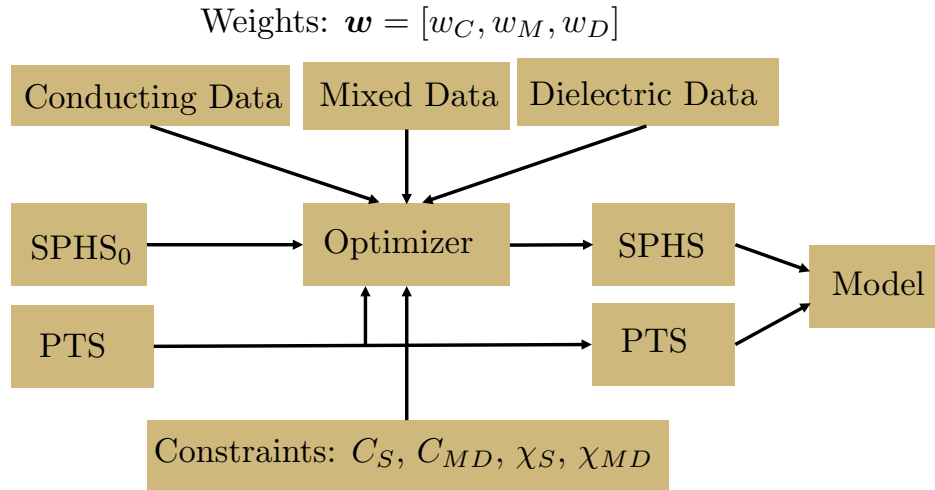
Figure 2.2: *Proposed Workflow Comparison with Previous Force and Torque Methods*

depend heavily upon how many data points are used. In addition, complicated workarounds that automatically change probe radius are required to get accurate results when the object/probe separation distance is large. Current techniques use a spherical probe which has a radius that is a function of its distance from a target. The dependence on external probe geometry for force and torque calculations is clear in the above force and torque equations. This dependence is included into VMSM model generation when a cost function based on force and torque is used.

The workflow proposed in this paper seeks to address both of these issues. The initial step in modeling is the same — a single solid model of the target spacecraft is created. However, a solid model of external probe geometry is optional, and only used to gather limited force and torque data for verification of a model. A target voltage is prescribed and FEM software is used to calculate the self-capacitance of the target.

A SMSM model of the target geometry is then generated using any appropriate method. Note that the VMSM setup process in this paper is not tied to using SMSM in this step, but other fast methods such as a boundary element method or the method of moments could be used as well. All these solutions provide fast and accurate E-field predictions about a general shape. The SMSM method is used here because it provides an infinitely smooth E-field prediction and it's simplicity to setup. One SMSM development method, appropriate for spherical and cylindrical geometries, is to use a golden spiral algorithm to distribute SMSM spheres on the surface of the geometry.[2] A method appropriate for flat geometries is to use a function like MATLAB's *meshgrid* to generate a distribution of sphere positions on the surface of a plane. This distribution can then be translated, rotated and combined with other planar distributions of spheres to form complex SMSM geometries.[6] When combining distributions, care should be taken to eliminate redundant spheres so that none overlap. Root finders like Matlab's *fsolve* can then be used with Eq. (2.7) to determine appropriate sphere radii to match the SMSM model self-capacitance to the self-capacitance of the solid model. Using the prescribed target voltage and Eq. (2.1), the charge on each SMSM sphere is calculated. Using the same equation applied to an N-sphere VMSM model optimization problem, an optimizer is used to select the optimal positions and radii of the model spheres to minimize the following cost function at sample points l

$$J\left(R_1, R_2, \ldots, R_N, \mathbf{r}_1, \mathbf{r}_2, \ldots, \mathbf{r}_N\right) = \sum_{l=1}^{L} \frac{||\mathbf{E}_{VMSM,l} - \mathbf{E}_{SMSM,l}||}{||\mathbf{E}_{SMSM,l}||} \tag{2.8}$$

where L is the total number of electric field sample points.

Using this cost function results in several major improvements to the prior methodology. The first improvement is the separation of VMSM model generations from any external probe geometry. Next, while the torques go to zero about particular symmetry axes, causing issues computing the relative MSM fit error, the E-field is always non-zero at any location relative to a charged spacecraft outside the convex hull formed by its conducting surface. The final improvement is in the time required to complete all the steps in generating a VMSM model. Although the proposed E-field fitting methodology adds the step of creating a SMSM model for a given target geometry and voltage, this process requires significantly less computational effort than computing forces and torques at many relative positions with FEM. While the FEM takes a few minutes to compute the force and torque at each position, a SMSM model with a few hundred spheres will compute the electric field at a few tens or hundreds of positions in a less than a minute. Reference 5 discusses fitting to much smaller numbers of force and torque data points; however, using the proposed method, hundreds of data points are calculated rapidly and used to create a VMSM model in much less than the time it requires to calculate one force and torque calculation using commercial FEM software. A flowchart comparing the previous force and torque optimization procedure and the proposed E-field matching method is included in Figure 2.2. The fitting speed are compared in detail in the following numerical simulation sections.

2.1.1.2.2   SMSM Validation

Before optimizing on a cost function built from a SMSM model, it is prudent to compare the accuracy of SMSM to other methods. The Method Of Images (MOI) provides an analytic infinite series solution to the problem of predicting the force between two spherical conductors.[7,8] The method consists of placing smaller and smaller image charges within the body of each sphere to balance out the potential on the surfaces. As the number of image charges increases, the solution converges.

SMSM models of spheres are made with a variable number of spheres, and the force between the two bodies is compared to that predicted by MOI. For this case, two spheres with 1 meter radius are separated by 5 meters, and charged to ±10 kV. The SMSM model is shown in Fig. 2.3(a), a cartoon for MOI showing the iterative charges is shown in Fig. 2.3(b), and the results are plotted in Figure 2.3(c).

The x-axis indicates either the number of images charges used in each sphere for the MOI, or the number of individual spheres in each SMSM sphere. The MOI converges with 40 image charges, and SMSM converges with around 100 spheres. Since both methods converge to the same value, SMSM is validated as a method for predicting forces and torques on a sphere.

Now consider a more complex shape for which there is no analytical answer to compare to. In this case SMSM must be compared to an FEM program. Force and torque accuracy of a box-and-panel SMSM model with respect to FEM analysis is shown in Figure 2.4. Average force and torque errors of the SMSM model are within a few percent of FEM-computed forces and torques.

The errors are shown via color in Figures 2.4(a) and 2.4(b) and the shell-averaged error is shown in Fig. 2.4(c). The color plots show that the error is concentrated across certain directions. For instance, the torque errors are greatest along the negative z axis. This is because the actual torque is very near zero along that direction and thus it is very susceptible to FEM grid noise. The shell-averaged errors also show some interesting structure - the errors initially drop from around 5% down to around 2.5% at near 10 meter separations, and then climb up to around 4% at 15 meters. This may be due to two opposite trends that become more or less dominant with distance. At very close distances ($\sim$ 5 meters), FEM performs very well and grid resolution is not

(a) SMSM schematic, color indicates charge

(b) MOI iterative image charge placement illustration
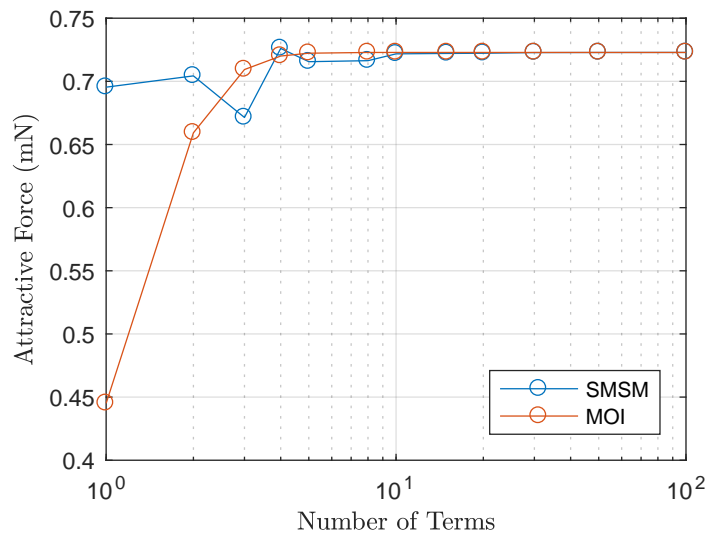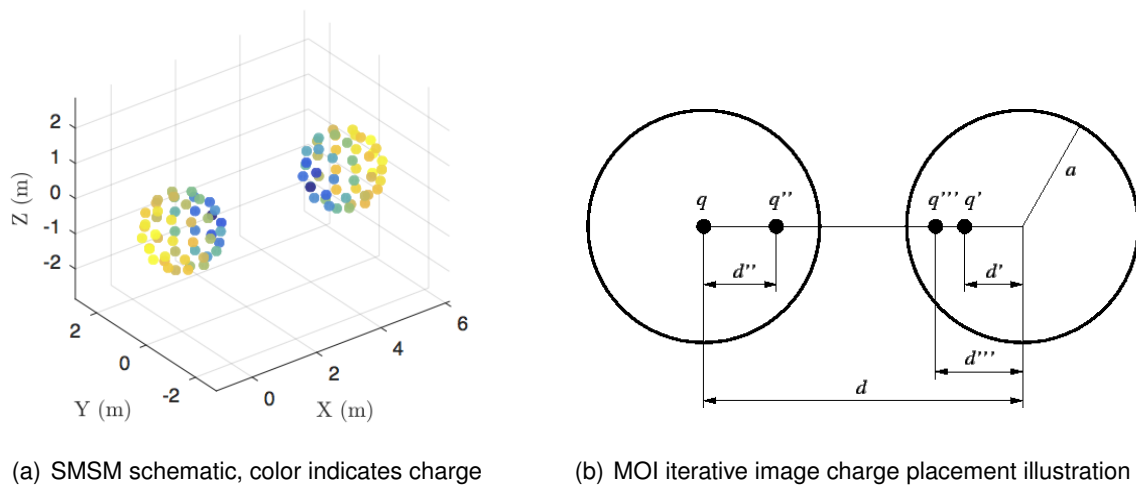
(c) Comparison Between MOI and SMSM

Figure 2.3: *Comparison of MOI and SMSM for predicting force on two spheres*

a problem, but the relatively coarse nature of SMSM gives large errors. At medium distances ($\sim$10 meters) FEM is still performing well, but the increased distance causes grid resolution problems which increase FEM grid noise and decrease the accuracy of the FEM solution, however, SMSM increases in accuracy due to the increased separation distance. At far separations ($\sim$15 meters), the grid noise is very large which causes increased differences from the truth, even though SMSM is performing very well at this distance. It is thought that the middle region near 10 meters is where the increase in SMSM accuracy from being far apart best balance out the errors in FEM accuracy from grid noise.

2.1.1.2.3 *Target Geometry, Data Generation and Optimization Methods*

Two target geometries are used to compare the proposed E-field matching method to the previous force and torque method and to establish the accuracy of models generated using E-

(a) SMSM Torque Error with Respect to FEM

(b) SMSM Force Error with Respect to FEM
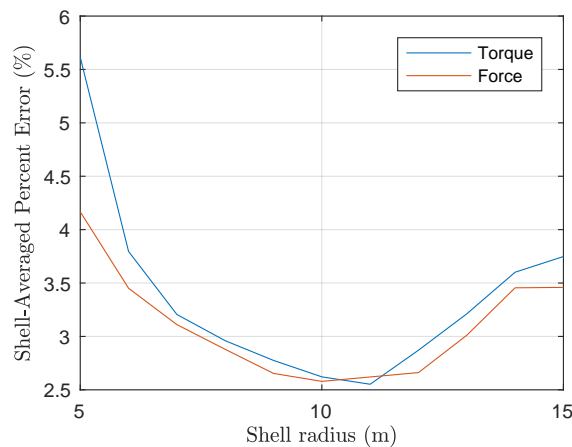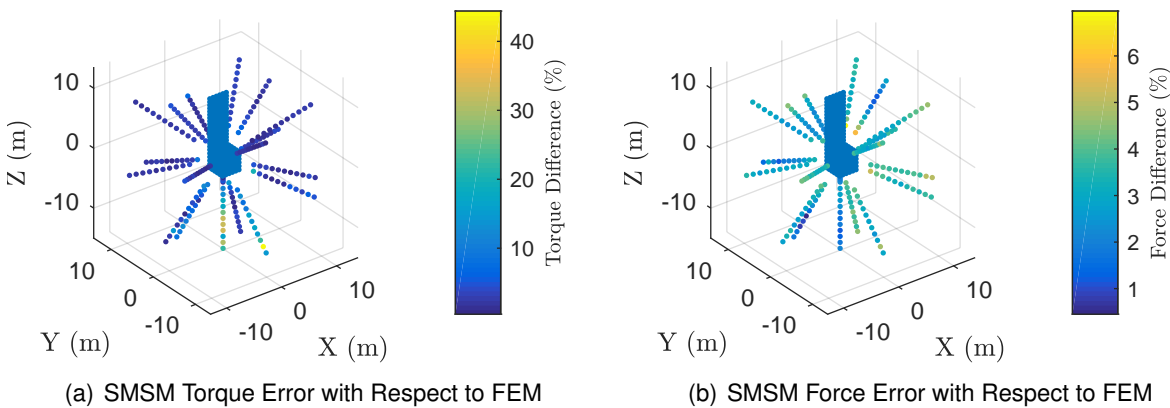
(c) SMSM Force and Torque Errors with Respect to FEM

Figure 2.4: *SMSM Force and Torque Errors*

field matching. A two-sphere VMSM model is created for a charged cylinder, with a radius of 0.5 m and a height of 3 m, centered at the origin and oriented along the y-axis using the E-field matching method. This geometry is selected for easy comparison to previous work using force and torque matching.[2,3,5]

Data for the study involving the cylinder geometry are generated at evenly spaced intervals on 90 degree arcs centered at the origin, lying in the x-y plane and in the fourth quadrant. The symmetry of the cylinder model requires data in only one quadrant for the optimization process. Force and torque data is generated using Maxwell 3D at the selected sample points. A SMSM model of the cylinder, shown in Figure 2.6, is created to generate E-field data at the same sample points. Only sample points lying on the arc of a 5 m radius circle are used for optimization, as shown in Figure 2.5(a).

Two optimization methods are used to generate cylinder VMSM models: a global optimization method using Mathematica's Differential Evolution algorithm is used to optimize the force and torque cost function of Eq. (2.6), and MATLAB's *fmincon* local optimizer is used to minimize the E-field cost function of Eq. (2.8). Self-capacitance for the cylinder is calculated using Maxwell 3D.

Since a two-sphere VMSM model is used to represent the cylinder and the cylinder has symmetry about the x-axis, the VMSM model can be parameterized by one radius value r, which is shared by both spheres, and the separation distance, ρ, between the two spheres. This model is
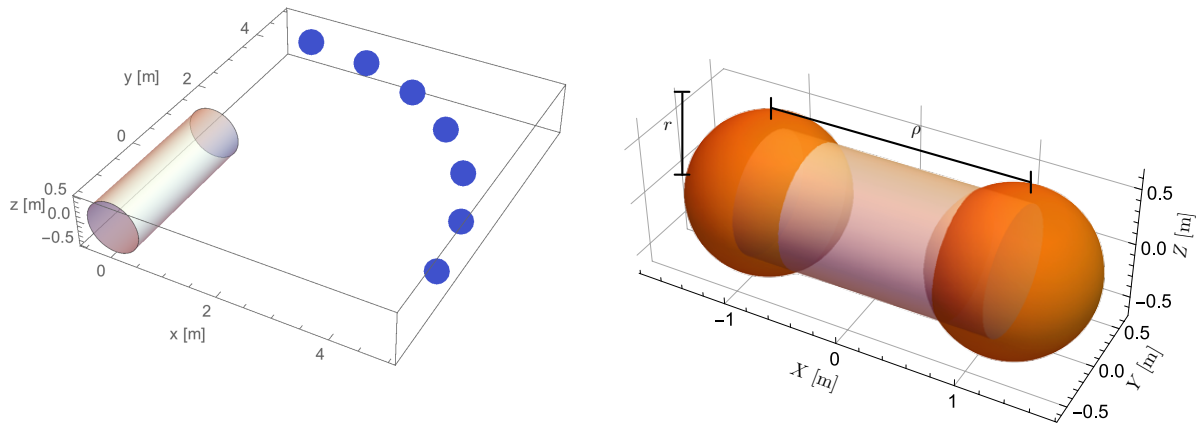
(a) Distribution of Sample Points Around Cylinder

(b) Two-Sphere VMSM Cylinder Model with Parameter Annotations[5]

Figure 2.5: *Cylinder Data Distribution and VMSM Model Parameters*
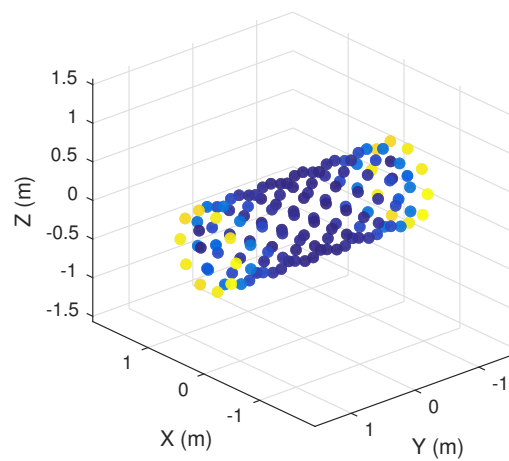
Figure 2.6: *SMSM Model of a Cylinder, Color Indicates Charge*

shown in Figure 2.5(b).

Using this model, an exact formula for the VMSM model self-capacitance can be derived[5]

$$C = \frac{1}{k_\mathsf{c}} \frac{2r\rho}{r + \rho} \tag{2.9}$$

where r and ρ are the radius and separation of the spheres as shown in Fig. 2.5(b). Imposing a self-capacitance constraint, matching the VMSM model self-capacitance to the value calculated by FEM, ensures that Lorentz forces and far-field Coulomb forces are automatically matched. In addition, it reduces the optimization problem to one dimension, because for any r value there is only one corresponding ρ value for which the constraint is met. Solving Eq. (2.9) for ρ yields[5]

$$\rho = \frac{rC_{\mathsf{mod}}}{2r - C_{\mathsf{mod}}} \tag{2.10}$$

where

$$C_{\mathsf{mod}} = k_\mathsf{c}C \tag{2.11}$$

Since C_{mod} is a scaling of the self-capacitance, it is used to impose the self-capacitance constraint in the following studies because its value is on the order of model parameters. Both the optimal r and ρ values are solved for using *fmincon* and the self-capacitance constraint is imposed numerically.

The second target spacecraft geometry that is selected for this study is a box-and-panel satellite modeled as a cube shaped bus with a long, slender panel attached. The bus width, height and depth are 3 m. The panel width is 3 m, depth is 0.2 m and height is 8.5 m. The panel is located on the top of the bus extending in the z-axis direction with one of its large faces coplanar with the positive y face of the bus. This model geometry is shown in Figure 2.7. This geometry is selected because it has significant variation from simple geometric shapes like cylinders and represents a more realistic target spacecraft. It also shows symmetry that can be used to impose additional constraints on the positions of the VMSM model spheres, and this symmetry is exploited to reduce the amount of data that is required for the optimization procedure.

A SMSM model of the box-and-panel is generated using MATLAB's *meshgrid* feature to create many rectangles which are translated and rotated to make the full spacecraft, and electric field data is generated using Eq. (2.5), at positions spread radially about the SMSM model. Sample points are generated using the golden spiral algorithm, which places equally spaced points on the surface of a sphere.[9] This radial spread of electric field data produces distributions of shells of data, which are easily selected or neglected, or reduced to hemispheres or octants for fitting, such as the one shown in Figure 2.7. Whole spherical shells of data are produced for the box-and-panel geometry; however, due to the symmetry of the model, the complete behavior of the electric field produced by the SMSM model can be captured in one hemisphere of data.

One, two and three-sphere VMSM reduced-coordinate models are created with this data using E-field matching and MATLAB's *fmincon* optimization algorithm. Various sets of data, including whole spheres, hemispheres and multiple shell sets, are used in the optimization processes. In addition, a three-sphere 4 degree-of-freedom VMSM model is generated using E-field matching and *fmincon*. Only shells with radii larger than 12 m are used for optimization to avoid overlap between sample points and SMSM spheres, which would invalidate Eq. (2.5). Like the cylinder model optimization process, the box-and-panel self-capacitance is calculated using Maxwell 3D and the self-capacitance constraints on the optimization processes are imposed numerically. Additional inequality constraints are imposed for the two and three-sphere VMSM models to ensure aesthetically pleasing models in which spheres do not overlap.
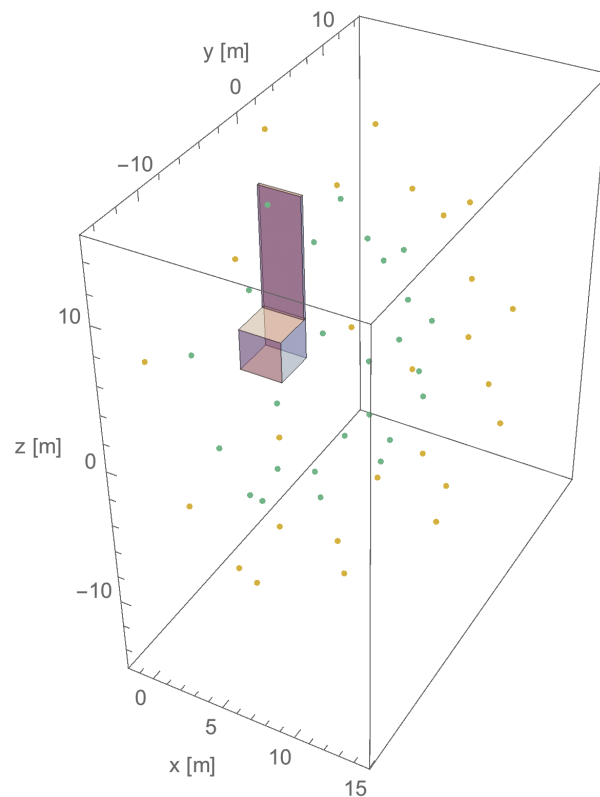
Figure 2.7: *Box-and-Panel Geometry with Data Point Distribution*

2.1.1.3   Cost Function Comparison

The cost function of Eq. (2.6) is compared with the proposed electric field cost function of Eq. (2.8) to compare their characteristics. Both cost functions are used to generate two-sphere VMSM models for a perfectly conducting cylinder charged to 30 kV. Maxwell 3D is used to determine a cylinder self-capacitance value of 106.8345 pF. Noting a potential singularity in Eq. (2.10) when r is one half C_{mod}, the cost function values, shown in Figures 2.8(a) and 2.8(b), along the intersection with the self-capacitance constraint surface are plotted against r for which ρ is positive. The force and torque cost function is evaluated across one quadrant and shell of FEM-generated force and torque predictions. The E-field cost function is evaluated across the same quadrant and shell, but using SMSM-generated E-field predictions.

The r values minimizing both cost functions are nearly identical, differing by only 0.2%. Investigating the cost function sensitivities near both minima suggests that force and torque errors are more sensitive to model parameters than E-field errors are. The proposed E-field cost function shows desirable characteristics, particularly for a local optimization algorithm like *fmincon*. It is generally smooth when compared with the force and torque cost function, and apart from a small region near the singularity in ρ, approaches its minimum unimpeded.

2.1.1.4   Constrained and Unconstrained Box-and-Panel VMSM Models

One, two and three-sphere box-and-panel VMSM models are generated with and without a self-capacitance constraint in order to determine the usefulness of the constraint when applied to an optimization problem without far-field data noise. Models are fit to data in three whole spherical

(a) Former Force and Torque Cost Function   (b) New E-field Cost Function
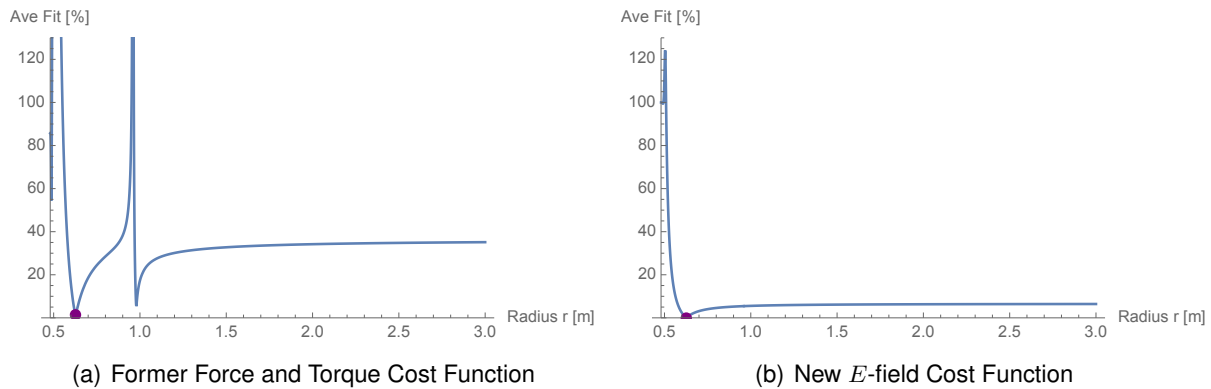
Figure 2.8: *Force and Torque and E-Field Cost Functions for Cylinder Model.*

shells with radii of 15, 20 and 25 m. Symmetry of the box-and-panel geometry about the $y-z$ plane is used to reduce the $4N$ degree-of-freedom optimization problem to a $3N$ degree-of-freedom problem. Imposing a self-capacitance constraint reduces the degrees-of-freedom to $3N - 1$. The model is charged to 30 kV. Maxwell 3D is once again used to calculate self-capacitance, and returns a value of 336.14 pF. Optimizer initial conditions are chosen loosely based on the box-and-panel geometry. A visualization the VMSM models of the box-and-panel geometry is included in Figure 2.9.

Tables 2.1-2.3 show the initial and final conditions for the one, two and three-sphere box-and-panel models, with and without the self-capacitance constraint.

Table 2.1: *Initial and Final States for One-Sphere VMSM Model Optimization, C- Constrained, NC- Non-Constrained*

	R_1 [m]	y_1 [m]	z_1 [m]
Initial	1.000	0.000	0.000
Final C	3.021	0.626	2.914
Final NC	2.951	0.608	2.785

Table 2.2: *Initial and Final States for Two-Sphere VMSM Model Optimization, C- Constrained, NC- Non-Constrained*

	R_1 [m]	R_2 [m]	y_1 [m]	z_1 [m]	y_2 [m]	z_2 [m]
Initial	1.000	1.000	0.000	0.000	1.400	6.000
Final C	2.202	1.458	0.135	0.210	1.596	8.183
Final NC	2.201	1.471	0.134	0.207	1.600	8.177

Table 2.3: *Initial and Final States for Three-Sphere VMSM Model Optimization, C- Constrained, NC- Non-Constrained*

	R_1 [m]	R_2 [m]	R_3 [m]	y_1 [m]	z_1 [m]	y_2 [m]	z_2 [m]	y_3 [m]	z_3 [m]
Initial	1.000	1.000	1.000	0.000	0.000	1.400	6.000	1.400	9.000
Final C	2.039	1.323	1.120	-0.008	-0.166	1.319	4.584	1.555	8.972
Final NC	2.041	1.322	1.119	-0.007	-0.163	1.321	4.612	1.556	8.974

(a) One-Sphere Model   (b) Two-Sphere Model   (c) Three-Sphere Model
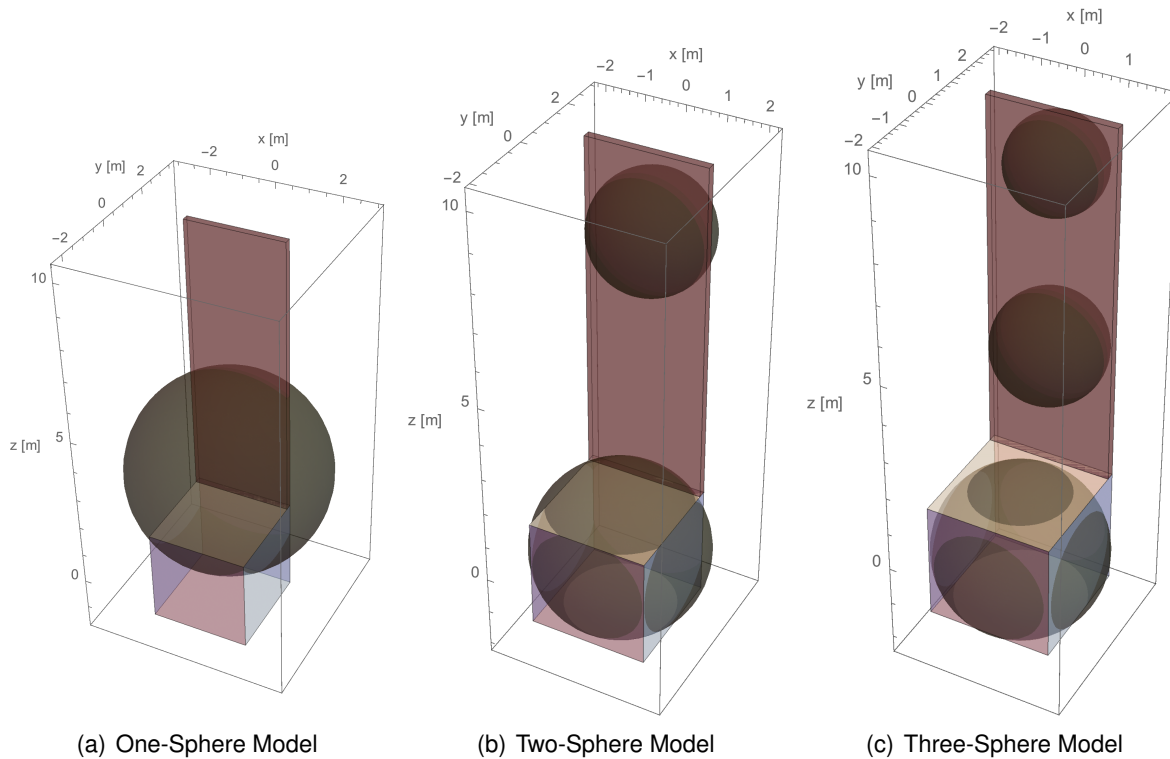
Figure 2.9: *Visualizations of VMSM Box-and-Panel Geometry Models Generated Using the E-Field Fitting Method*

Shell-averaged force and torque errors of the six VMSM models with respect to the SMSM generated data are shown in Figures 2.10(a) and 2.10(b), respectively. As can be seen, the self-capacitance constraint has utility even when far-field noise is not a concern. In particular, when generating a one-sphere model the self-capacitance constraint ensures that force errors far from the target geometry continue to decay as sample point radius is increased. The effect of the self-capacitance constraint is also dramatic for the two-sphere model. The force errors of the two and three-sphere models are nearly identical at 30 m from the target geometry when the constraint is imposed, whereas without it the two-sphere model model force errors remain significantly larger than the three-sphere model's. It is interesting to note that, as more spheres are added to the VMSM model, self-capacitance is matched automatically as displayed by the three-sphere force and torque errors. Both the constrained and non-constrained model errors overlap, and the optimal model parameters of each are nearly identical.

Another benefit of imposing the self-capacitance constraint is that it can significantly reduce computational effort. The number of function calls required to generate each of the six models is recorded. The results are shown in Figure 2.11. The results show that imposing the self-capacitance constraint consistently results in increased performance regardless of how many sphere are used to create the VMSM model. This performance increase is due to the reduced dimension of the search space when a self-capacitance constraint is enforced. Given the increased force and torque accuracy and decreased computation effort, the self-capacitance constraint should be enforced even when far-field noise is not a concern.

(a) Force Errors   (b) Torque Errors
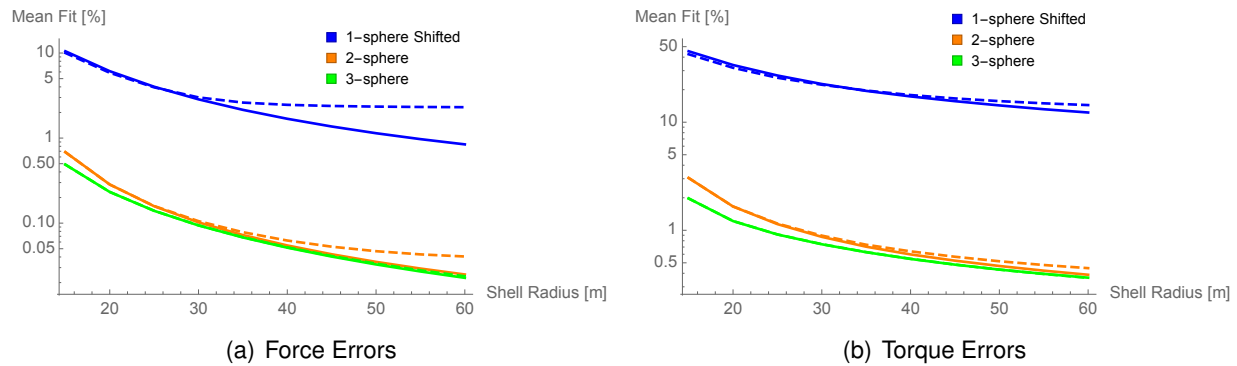
Figure 2.10: *One, Two and Three Sphere VMSM Model Force and Torque Errors with Respect to SMSM Force and Torque Predictions, (—) Constrained, (- -) Non-Constrained*
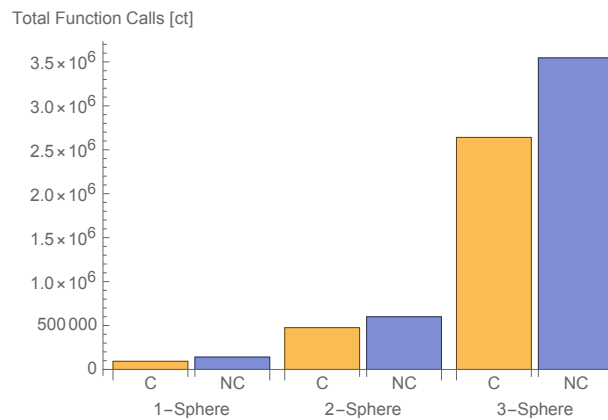
Figure 2.11: *Total Matlab Function Calls Required to Generate One, Two and Three-Sphere Box-and-Panel VMSM Models using E-Field Fitting*

2.1.1.5   Reduced-Shell Data Sets with Self-Capacitance Constraint

Since imposing a self-capacitance constraint forces force vectors in the far-field to automatically match, it is desired to investigate whether or not fewer numbers of shells with smaller radii can be used to effectively generate VMSM models. This question is interesting for two reasons: smaller data sets will reduce the amount of time required for optimization, and fitting to data closer to the target might increase near-field accuracy without significantly affecting accuracy at larger distances.

A three-sphere VMSM model is used to model the box-and-panel geometry. The VMSM model is fit to single shells at radii of 12, 14 and 15 m. The model voltage is set to 30 kV, and a self-capacitance constraint of 336.14 pF is imposed. The accuracy of these models are compared with each other and to the three-sphere constrained model generated using three whole shells. The resulting shell-averaged force, torque, and average error plots when compared with the SMSM model are shown in Figures 2.12(a)-2.12(c). These results show negligible differences in force and torque accuracy near the target, while the model fitted to the 12 m radius shell shows degraded accuracy far from the target. Accuracies of models fit to three whole shells and to 14 m and 15 m shell radii are nearly identical. The practical impact of the degraded accuracy for the model fitted to the 12 m shell is very small; however, for high accuracy at large distances from a target, a model should be fitted to at least one shell with a larger radius.

The performance impact of reducing the number of shells is analyzed by recording the number

(a) Force Errors

(b) Torque Errors
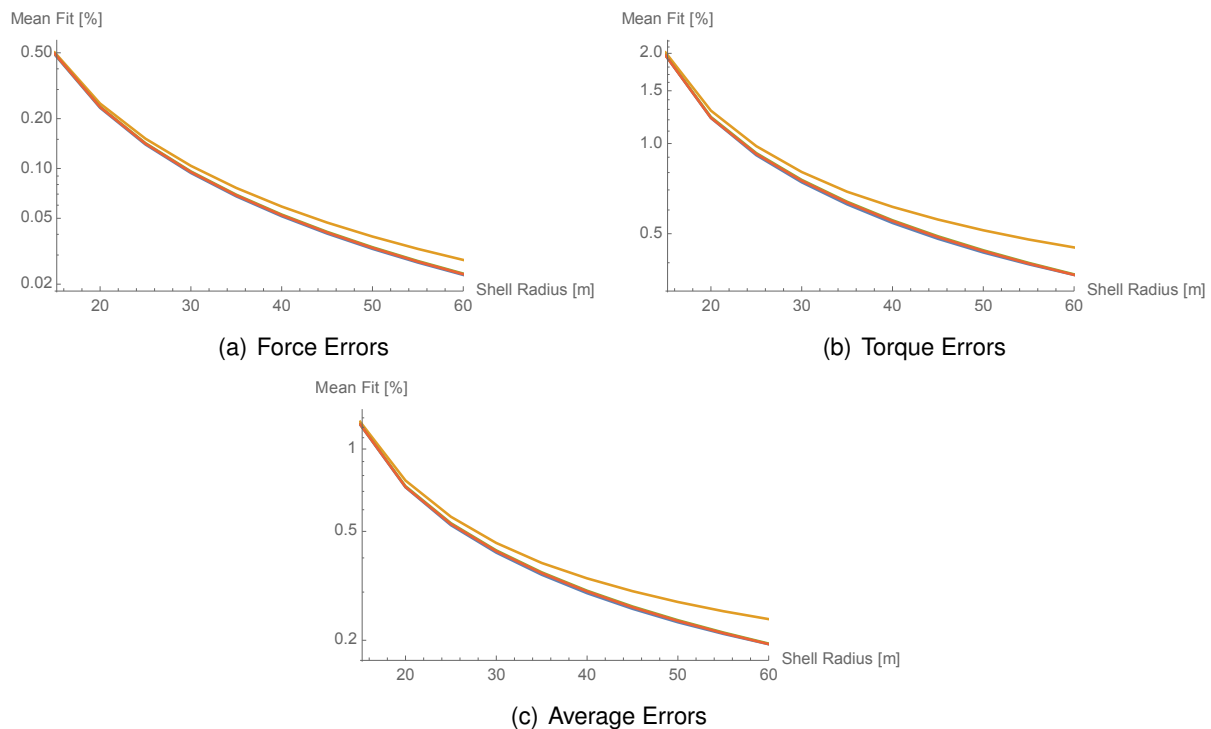
(c) Average Errors

Figure 2.12: *Model Force, Torque and Average (Force and Torque) Errors of Three-Sphere Box-and-Panel VMSM Models Generated Using: (—) 3 Whole Shells, (—) 15 m Shell, (—) 14 m Shell, (—) 12 m Shell*

of *fmincon* iterations and total time required to generate each model. The results are shown in Figures 2.13(a) and 2.13(b). These results show that there is not necessarily a positive correlation between decreased numbers of data points and increased performance. Fitting to data points very close to the target geometry increases the number of iterations required to generate a model. In addition, the time required to generate a model is not solely dependent upon the number of data points. While it takes more time to generate a model using three whole shells of data when compared to one whole shell at a radius of 15 m, it takes approximately the same amount of time to generate a model using one whole shell with a radius of 12 m even though the number of *fmincon* iterations is 12% less. The competing interests of maintaining a self-capacitance constraint while fitting to electric field data near the target – which is far more variable than the same data at larger radii – is likely the reason for this phenomenon. Due to the increased error and decreased performance associated with fitting to shells very close to the target, it is recommended to fit models using shells at intermediate ranges. Doing so aids convergence of the optimizer, and the total time required to generate a model is decreased either because the number of iterations to convergence is decreased or because the total time required for one iteration of the optimizer is decreased, or both.

2.1.1.6 Modeling using General 4 Degree-of-Freedom MSM Spheres

Previous work focuses on simple geometries that have high levels of symmetry, like the cylinder model. For geometries like these, the number of MSM optimization parameters can be reduced significantly by specifying, for example, that the cylinder MSM spheres must lie on the symmetry axis. As geometric complexity increases, so does the effort required to find symmetries to exploit

(a) *fmincon* Iterations

(b) Total Model Generation Times
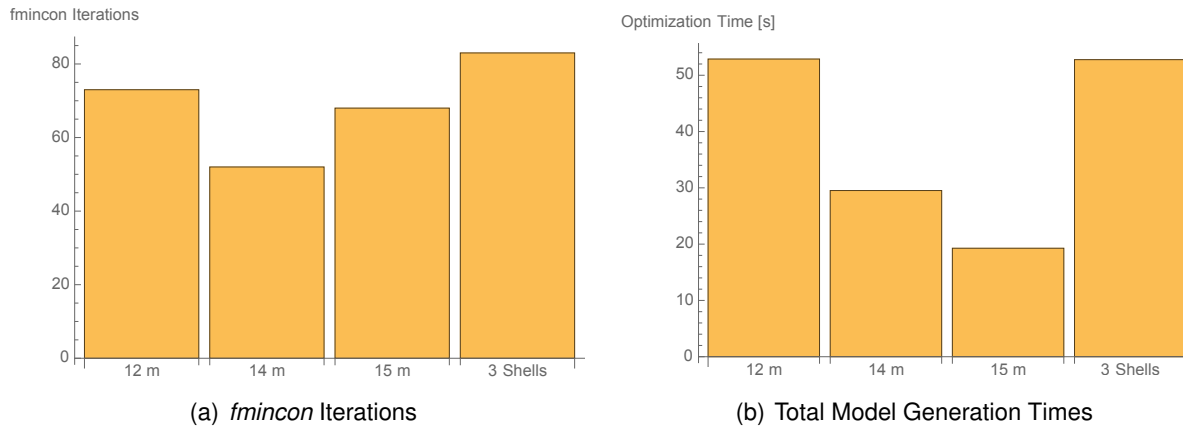
Figure 2.13: fmincon *Iterations and Total Model Generation Times Required to Generate Three Sphere VMSM Models Using E-Field Fitting and Shell Reduction for Various SMSM-Generated E-Field Data Sets*

Table 2.4: *Initial and Final States for Three-Sphere 4DOF VMSM Model Optimization*

	Initial	Final
R_1 [m]	1.000	2.051
R_2 [m]	1.000	1.299
R_3 [m]	1.000	1.106
x_1 [m]	0.000	-0.004
y_1 [m]	0.000	-0.004
z_1 [m]	0.000	-0.136
x_2 [m]	0.000	0.038
y_2 [m]	1.400	1.385
z_2 [m]	6.000	4.788
x_3 [m]	0.000	-0.028
y_3 [m]	1.400	1.534
z_3 [m]	9.000	8.993

and analytically parameterize them. Using general MSM 4 degree-of-freedom (4DOF) modeling allows each MSM sphere to have 3 location and one radius degree of freedom. This avoids the need to find symmetry and allows for optimization in a $4N$ dimension search space. Each parameter associated with a VMSM model sphere is found through optimization, and the up-front human-involvement cost of generating a model is reduced.

A three-sphere VMSM model of the box-and-panel geometry is generated using data in three whole shells with radii of 15, 20 and 25 m. A self-capacitance constraint is enforced using a value of 336.14 pF. The model voltage is set to 30 kV. The initial and final conditions for the 4DOF fitting problem are shown in Table 2.4.

The force and torque accuracy of the 4DOF model with respect to the box-and-panel SMSM model is compared to three-sphere 3DOF models using three whole shells and one half shell at 15 m in Figures 2.14(a) and 2.14(b). The model with the least accuracy is the 3DOF model fitted to one half shell of data. The 4DOF model's accuracy resembles the 3DOF model fitted to three whole shells. Since the optimizer knows nothing about the symmetry of the box-and-panel model, a whole shell of data must be used to generate an accurate model when 4DOF is used. Total *fmincon* iterations for each of the models shown in Figure 2.14 are shown in Table 2.5.

(a) Force Errors   (b) Torque Errors
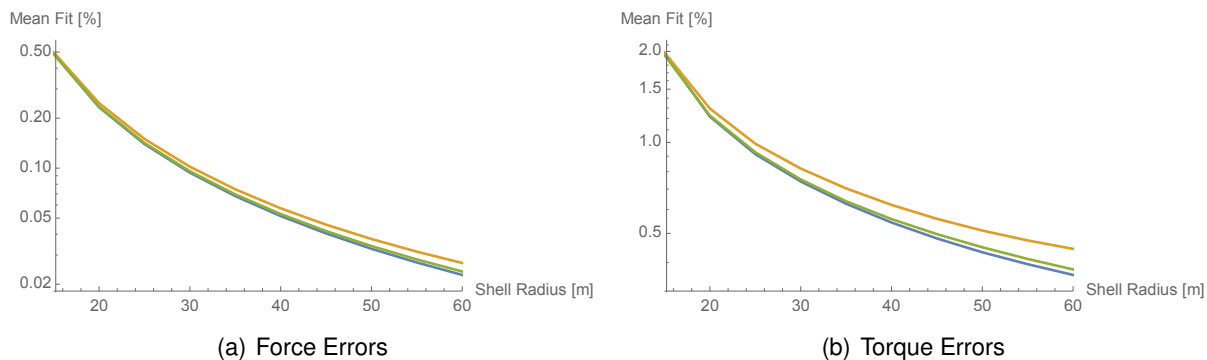
Figure 2.14: *4DOF Force and Torque Percent Relative Error Comparison to SMSM Force and Torque Predictions for: (——) Three-Sphere Model Three Whole Shells, (——) Three-Sphere Model One Half Shell, (——) Three-Sphere Model One Whole Shell (4DOF)*

Table 2.5: *Total Function Calls for 4DOF Model Comparison*

Model	Total *fmincon* Iterations
4DOF 3 Whole Shells	77
3DOF 3 Whole Shells	83
3DOF 1 Half Shell	132
3DOF 1 Whole Shell	68

Surprisingly, the 4DOF modeling method yields a converged result using only 58% of the iterations required for a 3DOF model using a half shell of data with the same radius. These results reiterate that the number of iterations required for convergence upon a useful model is far more dependent on using data at intermediate radii than on the number of data points used. However, when considering time required to generate a model, the 3DOF 1 half shell model is by far the most efficient to generate, requiring only about a third as much time as the three whole shell models. An interesting result is that the 4DOF model is generated in approximately the same amount of time as the 3DOF 3 whole shell model. These results show that 4DOF modeling using E-field fitting is promising from both an accuracy and performance perspective, and a 4DOF can be generated in approximately the same amount of time as a 3DOF model using the same number of data points at the same shell radii.

2.1.2 Appropriate Fidelity Models (AFMs)

2.1.2.1 Motivation for AFMs

The problem of two charged conductors interacting through electrostatics is similar to that of two bodies interacting gravitationally. The differential force in both cases is proportional to the product of either the masses or charges, and inversely proportional to the square of the distance between them. The gravitational problem can be readily solved using conic sections if both bodies are treated as point masses. For added fidelity, the larger body is treated as a general shape through the use of a spherical harmonic expansion. If both bodies are near the same size and very close, they must both be treated in a general manner solving the full gravitational two-body problem. This problem can be solved using a range of methods including expansions of mass distribution through MacCullagh's approximation,[10] inertia integrals[11] or numerically using a lumped-mass approach.[12] In the electrostatic problem, there is also an added complication: the total mass and its distribution

is fixed in a rigid body while the total charge and associated charge distribution change easily within a conductor. As the two conductors rotate and translate, the charge distribution changes and impacts the electrostatic forces and torques. For example, consider to negatively charged objects approaching each other. The electrons will repel each other and gather on the far sides of the objects, causing a differential charge distribution. In contrast, as two asteroids approach each other their mass distribution remain unchanged.

Many methods exist to solve the electrostatic problem numerically, and they all begin with prediction of the charge distribution. This can be done using full FEA software which is very accurate but much too slow for dynamics simulations, or more coarse methods like the Method of Moments.[13] Once the charge distribution is known, the total Coulomb force can be found by summing the force between every facet in one body and every facet in the other body. A new method for force and torque prediction is the Multi-Sphere Method (MSM),[3] which places spheres of tunable radii and position throughout the conductor. This process divides into Surface MSM (SMSM), which was optimized for large numbers of spheres constrained to be on the surface of the conductor by Stevenson et. al. in[2] and Volume MSM (VMSM), which uses a small number of spheres with unconstrained positions and was optimized by Chow et. al. in.[3,5] While these methods offer an excellent trade study between accuracy and speed, all are numerical and do not enable closed-form analysis. Analytical insight is instrumental in any dynamics and stability studies, such as for the de-spin and ET concept.

Analytical formula for the electrostatic two-body problem are found for the special case of two conducting spheres using the Method of Images.[7,8,14] If the bodies are not spherical, the multipole expansion method can be used to find the electric potential in the vicinity of a charge distribution by expanding the charge distribution in powers of $1/R$.[14] The potential energy of two charged molecules can also be found and differentiated with respect to position attitude to find force and torque.[15] These expansions use terms similar to the inertia integrals used by Hou.[11] The conference paper cited in Reference[16] introduces a similar method for finding the electrostatic force and torque between two charged spacecraft, but differs in that it does not find the potential but finds the force and torque directly. This method for predicting force and torque is called the Appropriate Fidelity Measures (AFM) method, named for the measures of the charge distribution that appear due to the appropriate fidelity truncation of the binomial series.

Reference[16] illustrates an early form of the AFM concept and investigates some special cases of an isolated body in a flat or radial field, but doesn't develop the full two body AFM theory. Flat field analysis was furthered for the special case of a High Area-to-Mass Ratio (HAMR) object's orbit being perturbed by Earth's magnetic field in Reference.[1] This report provides the first comprehensive theory of AFMs for general spacecraft applications, including the general case of two interacting charged bodies, and shows how the radial field is a special case of the general two body problem.[17] Providing a general formulation enables developing any particular AFM models that consider the local environmental electric and magnetic fields, as well as electric fields due to arbitrary neighboring charged spacecraft. This work differs from the multipole expansion cited in Reference[15] in that this work also presents a method for predicting the moments of the charge distribution from the voltage and attitude of each craft as well as their separation.

2.1.2.2 Problem Statement

This section establishes the notation and variables used in this paper, as well as the fundamental charging and force models employed and the key binomial expansion used. Consider two charged, conducting neighboring spacecraft as is shown in Figure 2.15 with a known charge distribution. This later assumption is relaxed later in the development to assume that only the potentials and

relative attitude and separation are known. They each experience a force and torque due to the other's charge. The force and torque on body 2 is found by integrating the differential force, which is a function of body 1's charge distribution, across body 2.

$$\mathrm{d}\boldsymbol{F}_2 = \frac{\mathrm{d}q_1 \mathrm{d}q_2 \boldsymbol{R}}{4\pi\epsilon_0 R^3} \tag{2.12}$$

where $\boldsymbol{R}$ points from $\mathrm{d}q_1$ to $\mathrm{d}q_2$. The separation vector is expressed from body vectors and a vector between the center of mass of each body $\boldsymbol{R} = \boldsymbol{R}_c + \boldsymbol{r}_2 - \boldsymbol{r}_1$. Using this substitution makes the differential force

$$\mathrm{d}\boldsymbol{F}_2 = \frac{\mathrm{d}q_1\,\mathrm{d}q_2\,\boldsymbol{R}_c + \boldsymbol{r}_2 - \boldsymbol{r}_1}{4\pi\epsilon_0\,||\boldsymbol{R}_c + \boldsymbol{r}_2 - \boldsymbol{r}_1||^3} \tag{2.13}$$
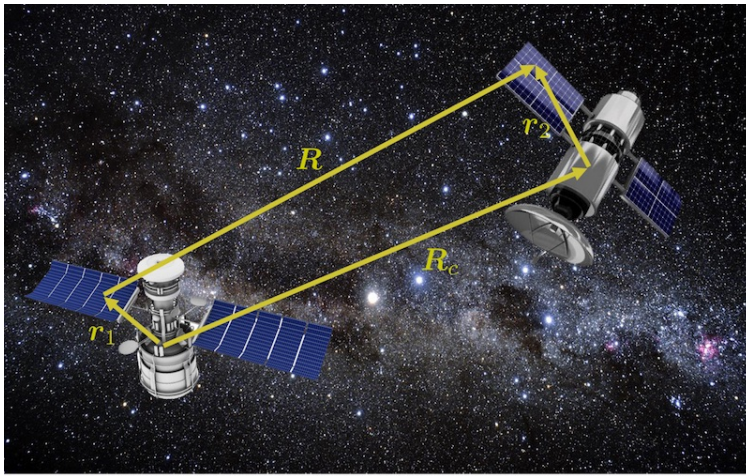
Figure 2.15: *Coordinate system for inter-craft derivation*

Where ϵ_0 is the permittivity of free space, $\epsilon_0 \approx 8.854187 * 10^{-12}$ F/m. The differential force is approximated by binomially expanding the denominator and truncating higher-order terms on the assumption that the body radii ($\boldsymbol{r}_1$ and $\boldsymbol{r}_2$) are small compared to their separation ($\boldsymbol{R}_c$).

$$\frac{1}{||\boldsymbol{R}_c + \boldsymbol{r}_2 - \boldsymbol{r}_1||^3} = (R_c^2 + r_1^2 + r_2^2 + 2(\boldsymbol{R}_c \cdot \boldsymbol{r}_2 - \boldsymbol{R}_c \cdot \boldsymbol{r}_1 - \boldsymbol{r}_2 \cdot \boldsymbol{r}_1))^{-3/2} \tag{2.14}$$

$$= \frac{1}{R_c^3}\left[1 + \left(\frac{r_2^2}{R_c^2} + \frac{r_1^2}{R_c^2} + \frac{2}{R_c^2}(\boldsymbol{R}_c \cdot \boldsymbol{r}_2 - \boldsymbol{R}_c \cdot \boldsymbol{r}_1 - \boldsymbol{r}_2 \cdot \boldsymbol{r}_1)\right)\right]^{-3/2} \tag{2.15}$$

Expand the denominator to second order using a binomial series $(1+x)^{-3/2} \approx 1 - \frac{3}{2}x + \frac{15}{8}x^2$ and reassemble to approximate the differential force as:

$$\mathrm{d}\boldsymbol{F}_2 = \frac{\mathrm{d}q_1\,\mathrm{d}q_2}{4\pi\epsilon_0 R_c^3}(\boldsymbol{R}_c + \boldsymbol{r}_2 - \boldsymbol{r}_1)\left(1 - \frac{3r_1^2}{2R_c^2} - \frac{3r_2^2}{2R_c^2} - \frac{3(\boldsymbol{R}_c \cdot \boldsymbol{r}_2 - \boldsymbol{R}_c \cdot \boldsymbol{r}_1 - \boldsymbol{r}_2 \cdot \boldsymbol{r}_1)}{R_c^2} + \right.$$
$$\left. \frac{15((\boldsymbol{R}_c \cdot \boldsymbol{r}_2)^2 + (\boldsymbol{R}_c \cdot \boldsymbol{r}_1)^2 - (\boldsymbol{R}_c \cdot \boldsymbol{r}_1)(\boldsymbol{R}_c \cdot \boldsymbol{r}_2))}{2R_c^4}\right) \tag{2.16}$$

This differential is integrated over the entire body to obtain the net electrostatic force on this object, or crossed with the body position vector and integrated over the body to obtain torque.

2.1.2.3 Appropriate Fidelity Measures

2.1.2.3.1 Fundamental AFM Expansion Terms Definition

The problem of two charged bodies interacting through electrostatics is similar to two massive bodies interacting through gravity. Just as moments of the mass distribution play a key role in solving the gravitational two-body problem,[11] moments of the charge distribution play a key role in predicting electrostatic force and torque. Three especially important moments of the charge distribution are identified and named here:

$$Q = \int_B \mathrm{d}q \qquad\qquad \boldsymbol{q} = \int_B \boldsymbol{r}\,\mathrm{d}q \qquad\qquad [Q] = \int_B -[\tilde{r}][\tilde{r}]\,\mathrm{d}q \qquad (2.17)$$

Q is a scalar and is the total charge, $\boldsymbol{q}$ is a 3×1 vector and is defined as the dipole moment, and $[Q]$ is a 3×3 tensor defined as the charge tensor. The vector $\boldsymbol{r}$ points from the center of mass to the differential charge $\mathrm{d}q$, and $[\tilde{r}]$ is the matrix form of the vector cross product: $\boldsymbol{a} \times \boldsymbol{b} = [\tilde{a}]\boldsymbol{b}$. If the gravity analogy is used, the total charge Q is similar to the total mass, the dipole moment $\boldsymbol{q}$ is similar to the total mass multiplied by the offset between the center of a coordinate system and the true center of mass, and the charge tensor $[Q]$ is similar to the inertia tensor. The dipole moment $\boldsymbol{q}$ provides a measure of where the center of charge is in relation to the center of mass. If $\boldsymbol{q}$ is zero, then the center of charge and mass locations are identical. To relate these AFM terms to the variables commonly used in multipole expansions, Q and $\boldsymbol{q}$ are the mono and dipole terms, and the charge tensor $[Q]$ defined here is related to the quadrupole $[Q_p]$ by $[Q_p] = -3[Q] + 2\mathrm{tr}([Q])$.[14]

2.1.2.3.2 Inter-Craft Electrostatic Reactions

This section derives the force and torque on body 2 due the charge on body 1 and 2. This is done using the 2nd order binomial expansion for the denominator of the differential force.

2.1.2.3.2.1 Force Derivation

The total force on body 2 is found by integrating the differential force over the entire body

$$\boldsymbol{F}_2 = \frac{1}{4\pi\epsilon_0 R_c^3} \int_{B_1}\int_{B_2} (\boldsymbol{R}_c + \boldsymbol{r}_2 - \boldsymbol{r}_1)\left(1 - \frac{3r_1^2}{2R_c^2} - \frac{3r_2^2}{2R_c^2} - \frac{3(\boldsymbol{R}_c\cdot\boldsymbol{r}_2 - \boldsymbol{R}_c\cdot\boldsymbol{r}_1 - \boldsymbol{r}_2\cdot\boldsymbol{r}_1)}{R_c^2} + \right.$$

$$\left. \frac{15((\boldsymbol{R}_c\cdot\boldsymbol{r}_2)^2 + (\boldsymbol{R}_c\cdot\boldsymbol{r}_1)^2 - (\boldsymbol{R}_c\cdot\boldsymbol{r}_1)(\boldsymbol{R}_c\cdot\boldsymbol{r}_2))}{2R_c^4}\right)\mathrm{d}q_2\mathrm{d}q_1 \quad (2.18)$$

This equation is broken into three parts: the terms resulting from the $\boldsymbol{R}_c, \boldsymbol{r}_1$, and $\boldsymbol{r}_2$ which are denotes as $\boldsymbol{F}_{2_0}, \boldsymbol{F}_{2_1}$ and $\boldsymbol{F}_{2_2}$, respectively. The first term $\boldsymbol{F}_{2_0}$ is expressed as

$$
\begin{aligned}
\boldsymbol{F}_{2_0} =& \frac{\boldsymbol{R}_c}{4\pi\epsilon_0 R_c^3} \int_{B_1}\int_{B_2} \left(1 - \frac{3r_1^2}{2R_c^2} - \frac{3r_2^2}{2R_c^2} - \frac{3(\boldsymbol{R}_c\cdot\boldsymbol{r}_2 - \boldsymbol{R}_c\cdot\boldsymbol{r}_1 - \boldsymbol{r}_2\cdot\boldsymbol{r}_1)}{R_c^2} + \right.\\
& \left. \frac{15((\boldsymbol{R}_c\cdot\boldsymbol{r}_2)^2 + (\boldsymbol{R}_c\cdot\boldsymbol{r}_1)^2 - (\boldsymbol{R}_c\cdot\boldsymbol{r}_1)(\boldsymbol{R}_c\cdot\boldsymbol{r}_2))}{2R_c^4}\right)\mathrm{d}q_2\mathrm{d}q_1\\
=&\frac{\boldsymbol{R}_c}{4\pi\epsilon_0 R_c^3}\left[Q_1 Q_2 - \left(\frac{3}{2R_c^2}\int_{B_1} r_1^2\,\mathrm{d}q_1 \int_{B_2}\mathrm{d}q_2\right) - \left(\frac{3}{2R_c^2}\int_{B_2}r_2^2\,\mathrm{d}q_2\int_{B_1}\mathrm{d}q_1\right)\right.\\
& - \left(\frac{3}{R_c^2}\boldsymbol{R}_c\cdot\int_{B_1}\mathrm{d}q_1\int_{B_2}\boldsymbol{r}_2\mathrm{d}q_2\right) + \left(\frac{3}{R_c^2}\boldsymbol{R}_c\cdot\int_{B_2}\mathrm{d}q_2\int_{B_1}\boldsymbol{r}_1\mathrm{d}q_1\right)\\
& + \left(\frac{3}{R_c^2}\int_{B_1}\boldsymbol{r}_1\mathrm{d}q_2\int_{B_2}\boldsymbol{r}_2\mathrm{d}q_2\right) + \left(\frac{15}{2R_c^4}\int_{B_1}\mathrm{d}q_1\int_{B_2}(\boldsymbol{R}_c\cdot\boldsymbol{r}_2)^2\mathrm{d}q_2\right)\\
& \left. + \left(\frac{15}{2R_c^4}\int_{B_2}\mathrm{d}q_2\int_{B_1}(\boldsymbol{R}_c\cdot\boldsymbol{r}_1)^2\mathrm{d}q_1\right) - \left(\frac{15}{2R_c^4}\int_{B_2}(\boldsymbol{R}_c\cdot\boldsymbol{r}_2)\mathrm{d}q_2\int_{B_1}(\boldsymbol{R}_c\cdot\boldsymbol{r}_1)\mathrm{d}q_1\right)\right]
\end{aligned}
\tag{2.19}
$$

Here the moments of the charge distribution given in Eq. 2.17 are used to simplify the equations. Using the identity $\int r^2\mathrm{d}q = \mathrm{tr}([Q])/2$ to simplify the above equation yields:

$$
\begin{aligned}
\boldsymbol{F}_{2_0} =& \frac{\boldsymbol{R}_c}{4\pi\epsilon_0 R_c^3}\left[Q_1 Q_2 - \frac{3Q_2}{4R_c^2}\mathrm{tr}([Q_1]) - \frac{3Q_1}{4R_c^2}\mathrm{tr}([Q_2]) - \frac{3Q_1}{R_c^2}\boldsymbol{R}_c\cdot\boldsymbol{q}_2\right.\\
& + \frac{3Q_2}{R_c^2}\boldsymbol{R}_c\cdot\boldsymbol{q}_1 + \frac{3Q_2}{R_c^2}\boldsymbol{q}_2\cdot\boldsymbol{q}_1 + \frac{15Q_1}{2R_c^4}\int_{B_2}(\boldsymbol{R}_c\cdot\boldsymbol{r}_2)^2\mathrm{d}q_2\\
& \left. + \frac{15Q_2}{2R_c^4}\int_{B_1}(\boldsymbol{R}_c\cdot\boldsymbol{r}_1)^2\mathrm{d}q_1 - \frac{15}{2R_c^4}(\boldsymbol{R}_c\cdot\boldsymbol{q}_2)(\boldsymbol{R}_c\cdot\boldsymbol{q}_1)\right]
\end{aligned}
\tag{2.20}
$$

To solve the two remaining integrals, apply the vector identity $(\boldsymbol{a}\cdot\boldsymbol{b})\boldsymbol{b} = ([\tilde{\boldsymbol{b}}][\tilde{\boldsymbol{b}}] + b^2[I])\boldsymbol{a}$ to the terms of the form $(\boldsymbol{R}_c\cdot\boldsymbol{r})^2$ and integrate to yield

$$
\boldsymbol{R}_c\cdot(\boldsymbol{R}_c\cdot\boldsymbol{r})\boldsymbol{r} = \boldsymbol{R}_c\cdot([\tilde{\boldsymbol{r}}][\tilde{\boldsymbol{r}}] + r^2[I])\boldsymbol{R}_c = \boldsymbol{R}_c^T[\tilde{\boldsymbol{r}}][\tilde{\boldsymbol{r}}]\boldsymbol{R}_c + R_c^2 r^2
\tag{2.21}
$$

$$
\rightarrow -\boldsymbol{R}_c^T[Q]\boldsymbol{R}_c + R_c^2\mathrm{tr}([Q])/2
\tag{2.22}
$$

and re-write $\boldsymbol{F}_{2_0}$ finally as:

$$
\begin{aligned}
\boldsymbol{F}_{2_0} =& \frac{\boldsymbol{R}_c}{4\pi\epsilon_0 R_c^3}\left[Q_1 Q_2 + \frac{3Q_2}{R_c^2}\mathrm{tr}([Q_1]) + \frac{3Q_1}{R_c^2}\mathrm{tr}([Q_2]) - \frac{3Q_1}{R_c^2}\boldsymbol{R}_c\cdot\boldsymbol{q}_2 + \frac{3Q_2}{R_c^2}\boldsymbol{R}_c\cdot\boldsymbol{q}_1\right.\\
& \left. + \frac{3Q_2}{R_c^2}\boldsymbol{q}_2\cdot\boldsymbol{q}_1 - \frac{15Q_1}{2R_c^4}\boldsymbol{R}_c^T[Q_2]\boldsymbol{R}_c - \frac{15Q_2}{2R_c^4}\boldsymbol{R}_c^T[Q_1]\boldsymbol{R}_c - \frac{15}{R_c^4}(\boldsymbol{R}_c\cdot\boldsymbol{q}_2)(\boldsymbol{R}_c\cdot\boldsymbol{q}_1)\right]
\end{aligned}
\tag{2.23}
$$

The second part of the force $\boldsymbol{F}_{2_1}$ is much simpler because many of the terms become third order and are neglected in this second order expansion.

$$
\boldsymbol{F}_{2_1} = \frac{1}{4\pi\epsilon_0 R_c^3}\int_{B_1}\int_{B_2}\boldsymbol{r}_2\left(1 - \frac{3(\boldsymbol{R}_c\cdot\boldsymbol{r}_2 - \boldsymbol{R}_c\cdot\boldsymbol{r}_1)}{R_c^2}\right)\mathrm{d}q_2\mathrm{d}q_1
\tag{2.24}
$$

$$
= \frac{1}{4\pi\epsilon_0 R_c^3}\left[Q_1\boldsymbol{q}_2 + \frac{3Q_1}{R_c^2}[Q_2]\boldsymbol{R}_c - \frac{3Q_1}{2R_c^2}\mathrm{tr}([Q_2])\boldsymbol{R}_c + \frac{3(\boldsymbol{R}_c\cdot\boldsymbol{q}_1)}{R_c^2}\boldsymbol{q}_2\right]
\tag{2.25}
$$

The third part of the force $\boldsymbol{F}_{2_2}$ is similar in form to $\boldsymbol{F}_{2_1}$ with the $\boldsymbol{r}_2$ being replaced with a $-\boldsymbol{r}_1$.

$$\boldsymbol{F}_{2_2} = \frac{1}{4\pi\epsilon_0 R_c^3} \int_{B_1} \int_{B_2} -\boldsymbol{r}_1 \left(1 - \frac{3(\boldsymbol{R}_c \cdot \boldsymbol{r}_2 - \boldsymbol{R}_c \cdot \boldsymbol{r}_1)}{R_c^2}\right) \mathrm{d}q_2 \mathrm{d}q_1 \tag{2.26}$$

$$= \frac{1}{4\pi\epsilon_0 R_c^3} \left[-Q_2 \boldsymbol{q}_1 + \frac{3Q_2}{R_c^2}[Q_1]\boldsymbol{R}_c - \frac{3Q_2}{2R_c^2}\mathrm{tr}([Q_1])\boldsymbol{R}_c + \frac{3(\boldsymbol{R}_c \cdot \boldsymbol{q}_2)}{R_c^2}\boldsymbol{q}_1 \right] \tag{2.27}$$

The total force is then expressed as

$$\boldsymbol{F}_2 = \frac{1}{4\pi\epsilon_0 R_c^3} \left[\left(Q_1 Q_2 + \frac{3Q_2}{2R_c^2}\mathrm{tr}([Q_1]) + \frac{3Q_1}{2R_c^2}\mathrm{tr}([Q_2]) - \frac{3Q_1}{R_c^2}\boldsymbol{R}_c \cdot \boldsymbol{q}_2 + \frac{3Q_2}{R_c^2}\boldsymbol{R}_c \cdot \boldsymbol{q}_1 + \frac{3Q_2}{R_c^2}\boldsymbol{q}_2 \cdot \boldsymbol{q}_1 \right. \right.$$
$$\left. - \frac{15Q_1}{2R_c^4}\boldsymbol{R}_c^T[Q_2]\boldsymbol{R}_c - \frac{15Q_2}{2R_c^4}\boldsymbol{R}_c^T[Q_1]\boldsymbol{R}_c - \frac{15}{R_c^4}(\boldsymbol{R}_c \cdot \boldsymbol{q}_2)(\boldsymbol{R}_c \cdot \boldsymbol{q}_1) \right)\boldsymbol{R}_c$$
$$\left. + Q_1 \boldsymbol{q}_2 + \frac{3Q_1}{R_c^2}[Q_2]\boldsymbol{R}_c + \frac{3(\boldsymbol{R}_c \cdot \boldsymbol{q}_1)}{R_c^2}\boldsymbol{q}_2 - Q_2 \boldsymbol{q}_1 + \frac{3Q_2}{R_c^2}[Q_1]\boldsymbol{R}_c + \frac{3(\boldsymbol{R}_c \cdot \boldsymbol{q}_2)}{R_c^2}\boldsymbol{q}_1 \right] \tag{2.28}$$

This equation is visualized in Table 2.6, where the common factor of $4\pi\epsilon_0 R_c^3$ is omitted, allowing easy ordering of terms based on which measures $(Q, \boldsymbol{q}, [Q])$ they incorporate. They are also ordered by the dimensionless ratio r/R_c where r is a characteristic dimension of either spacecraft. As the spacecraft move farther and farther away, the higher order terms in this variable matter less and less. The zeroth order term is in the upper left, the two boxes with two terms each are the first order terms, and the three boxes containing twelve terms along the diagonal are the second order terms. This table allows easy selection of the force terms needed for appropriate fidelity.

Table 2.6: *Force ordering matrix*

	Q_1	$\boldsymbol{q}_1$	$[Q_1]$
Q_2	$Q_1 Q_2 \boldsymbol{R}_c$	$\frac{3Q_2}{R_c^2}(\boldsymbol{R}_c \cdot \boldsymbol{q}_1)\boldsymbol{R}_c - Q_2\boldsymbol{q}_1$	$\frac{3Q_2}{2R_c^2}\mathrm{tr}([Q_1])\boldsymbol{R}_c$ $- \frac{15Q_2}{2R_c^4}(\boldsymbol{R}_c^T[Q_1]\boldsymbol{R}_c)\boldsymbol{R}_c$ $+ \frac{3Q_2}{R_c^2}[Q_1]\boldsymbol{R}_c$
$\boldsymbol{q}_2$	$Q_1\boldsymbol{q}_2 - \frac{3Q_1}{R_c^2}(\boldsymbol{R}_c \cdot \boldsymbol{q}_2)\boldsymbol{R}_c$	$\frac{3}{R_c^2}(\boldsymbol{q}_2 \cdot \boldsymbol{q}_1)\boldsymbol{R}_c$ $- \frac{15}{R_c^4}(\boldsymbol{R}_c \cdot \boldsymbol{q}_2)(\boldsymbol{R}_c \cdot \boldsymbol{q}_1)\boldsymbol{R}_c$ $+ \frac{3(\boldsymbol{R}_c \cdot \boldsymbol{q}_1)}{R_c^2}\boldsymbol{q}_2 + \frac{3(\boldsymbol{R}_c \cdot \boldsymbol{q}_2)}{R_c^2}\boldsymbol{q}_1$	
$[Q_2]$	$\frac{3Q_1}{2R_c^2}\mathrm{tr}([Q_2])\boldsymbol{R}_c$ $- \frac{15Q_1}{2R_c^4}(\boldsymbol{R}_c^T[Q_2]\boldsymbol{R}_c)\boldsymbol{R}_c$ $+ \frac{3Q_1}{R_c^2}[Q_2]\boldsymbol{R}_c$		

As might be expected, the force expression is symmetric, if one changes the sign on all $\boldsymbol{R}_c$ terms and switches the subscripts the force on body 1 is found to be equal in magnitude but opposite in direction to the force on body 2. This satisfies Newton's 3rd law.

2.1.2.3.2.2 Torque Derivation

The torque on body 2 is given by $\boldsymbol{T}_2 = \int_{B_1} \int_{B_2} \boldsymbol{r}_2 \times \mathrm{d}\boldsymbol{F}$, where the same binomial expansion as before is used to approximate $\mathrm{d}\boldsymbol{F}$ to second order.

$$\boldsymbol{T}_2 \quad = \quad \frac{1}{4\pi\epsilon_0 R_c^3} \int_{B_1} \int_{B_2} \boldsymbol{r}_2 \times (\boldsymbol{R}_c + \boldsymbol{r}_2 - \boldsymbol{r}_1)\left(1 - \frac{3(\boldsymbol{R}_c \cdot \boldsymbol{r}_2 - \boldsymbol{R}_c \cdot \boldsymbol{r}_1)}{R_c^2}\right)\mathrm{d}q_2\mathrm{d}q_1 \quad (2.29)$$

Because of the extra $\boldsymbol{r}_2$, many of the terms in the differential force expansion become third order and are neglected. The differential torque has three parts corresponding to the $\boldsymbol{r}_2 \times \boldsymbol{R}_c, \boldsymbol{r}_2 \times \boldsymbol{r}_2$ and $\boldsymbol{r}_2 \times \boldsymbol{r}_1$ components. The middle term is zero and the first and third are labeled by $\boldsymbol{T}_{2_0}$ and $\boldsymbol{T}_{2_1}$, respectivley. $\boldsymbol{T}_{2_0}$ is evaluated first:

$$\boldsymbol{T}_{2_0} = \frac{1}{4\pi\epsilon_0 R_c^3} \int_{B_1} \int_{B_2} \boldsymbol{r}_2 \times \boldsymbol{R}_c\left(1 - \frac{3(\boldsymbol{R}_c \cdot \boldsymbol{r}_2 - \boldsymbol{R}_c \cdot \boldsymbol{r}_1)}{R_c^2}\right)\mathrm{d}q_2\mathrm{d}q_1 \qquad (2.30)$$

$$= -\frac{1}{4\pi\epsilon_0 R_c^3}\boldsymbol{R}_c \times \int_{B_1} \int_{B_2} \boldsymbol{r}_2\left(1 - \frac{3(\boldsymbol{R}_c \cdot \boldsymbol{r}_2 - \boldsymbol{R}_c \cdot \boldsymbol{r}_1)}{R_c^2}\right)\mathrm{d}q_2\mathrm{d}q_1 \qquad (2.31)$$

Where higher order terms in the binomial expansion are neglected. The integral is identical to the force integral in Eq.(2.24) evaluated earlier, and is written down from inspection as:

$$\boldsymbol{T}_{2_0} = -\boldsymbol{R}_c \times \left[\frac{Q_1 \boldsymbol{q}_2}{R_c^3} + \frac{3(\boldsymbol{R}_c \cdot \boldsymbol{q}_1)\boldsymbol{q}_2}{R_c^5} + \frac{3Q_1[Q_2]\boldsymbol{R}_c}{R_c^5}\right] \qquad (2.32)$$

The other part of the torque comes from the $\boldsymbol{r}_1$ and is evaluated below:

$$\boldsymbol{T}_{2_1} = -\frac{1}{4\pi\epsilon_0 R_c^3} \int_{B_1} \int_{B_2} (\boldsymbol{r}_2 \times \boldsymbol{r}_1)\mathrm{d}q_2\mathrm{d}q_1 \qquad (2.33)$$

The binomial expansion here is truncated to just the first term because the $\boldsymbol{r}_2 \times \boldsymbol{r}_1$ term is already second order. This gives

$$\boldsymbol{T}_{2_1} = -\frac{1}{4\pi\epsilon_0 R_c^3}\boldsymbol{q}_2 \times \boldsymbol{q}_1 \qquad (2.34)$$

The total torque is found by summing $\boldsymbol{T}_{2_0}$ and $\boldsymbol{T}_{2_1}$ to yield

$$\boldsymbol{T}_2 = \frac{1}{4\pi\epsilon_0 R_c^3}\left[Q_1 \boldsymbol{q}_2 \times \boldsymbol{R}_c + \frac{3(\boldsymbol{R}_c \cdot \boldsymbol{q}_1)\boldsymbol{q}_2 \times \boldsymbol{R}_c}{R_c^2} - \frac{3Q_1\boldsymbol{R}_c \times [Q_2]\boldsymbol{R}_c}{R_c^2} + (\boldsymbol{q}_1 \times \boldsymbol{q}_2)\right] \qquad (2.35)$$

This equation is visualized in Table 2.7 which follows Table 2.6 in omitting the factor of $4\pi\epsilon_0 R_c^3$ and grouping terms by their order in the dimensionless ratio r/R_c. Terms closer to the upper left corner are lower order.

Table 2.7: *Torque ordering matrix*

	Q_1	q_1	$[Q_1]$
Q_2			
q_2	$Q_1\boldsymbol{q}_2 \times \boldsymbol{R}_c$	$\frac{3}{R_c^2}(\boldsymbol{R}_c \cdot \boldsymbol{q}_1)\boldsymbol{q}_2 \times \boldsymbol{R}_c + (\boldsymbol{q}_1 \times \boldsymbol{q}_2)$	
$[Q_2]$	$-\frac{3}{R_c^2}Q_1\boldsymbol{R}_c \times [Q_2]\boldsymbol{R}_c$		

As expected, there are no zeroth order terms, in fact there are no terms at all corresponding to the scalar charge Q_2. Unlike the force expansion, the torque is not symmetric, i.e. $\boldsymbol{T}_1 \neq -\boldsymbol{T}_2$. This is because the torque on body 1 and body 2 are not measured about the same point, but rather the center of mass of each body. If all torques are measured about the same point, such as the barycenter of the system, the torques are equal and opposite and cancel out and are not able to change the angular momentum of the system.

2.1.2.3.3   Radial Electrostatic Field Simplification

In Reference 16, the force and torque on a charged body are found by assuming a differential force of

$$\mathrm{d}\boldsymbol{F}_2 = \frac{Q_1 \mathrm{d}q_2}{4\pi\epsilon_0 R^3}\boldsymbol{R} \tag{2.36}$$

and integrating over body 2. Rather than repeating this integration, the first column of the force and torque ordering tables can be added to produce force and torque because that column only considers the scalar charge of body 1. This yields

$$\begin{aligned}
\boldsymbol{F}_2 = \frac{Q_1}{4\pi\epsilon_0 R_c^3}\Bigg[&Q_2\boldsymbol{R}_c + \boldsymbol{q}_2 - \frac{3(\boldsymbol{q}\cdot\boldsymbol{R}_c)}{R_c^2}\boldsymbol{R}_c + \frac{3[Q_2]\boldsymbol{R}_c}{R_c^2} + \frac{3\boldsymbol{R}_c}{2R_c^2}\mathrm{tr}([Q_2]) \\
&- \frac{15}{2R_c^4}(\boldsymbol{R}_c^T[Q_2]\boldsymbol{R}_c)\boldsymbol{R}_c\Bigg]
\end{aligned} \tag{2.37}$$

$$\boldsymbol{L}_2 = \frac{Q_1}{4\pi\epsilon_0 R_c^3}\left[\boldsymbol{q}_2 + \frac{3}{R_c^2}[Q_2]\boldsymbol{R}_c\right] \times \boldsymbol{R}_c \tag{2.38}$$

which agrees with the derivation done with the point charge differential force. This shows how force and torque in a radial field is a special case of the general two body problem. This is similar to how in most treatments a satellite is treated as a point mass while the earth is treated as a general body using spherical harmonics.

2.1.2.3.4   Flat Electrostatic Field Simplification

It is also of interest to calculate the force and torque on charged conducting bodies due to ambient flat electric and magnetic fields.[1] The differential force on a differential charge moving at $\boldsymbol{v}$ subject to $\boldsymbol{E}$ and $\boldsymbol{B}$ fields is given in Reference 18 as:

$$\mathrm{d}\boldsymbol{F} = \mathrm{d}q(\boldsymbol{E} + \boldsymbol{v}\times\boldsymbol{B}) \tag{2.39}$$

This differential force only varies significantly across a body if it is rotating very quickly near the geostationary point. The velocity is the orbital velocity $\boldsymbol{v}_o$ plus the transport velocity: $\boldsymbol{\omega}_{\mathcal{B}/\mathcal{E}}\times\boldsymbol{r}$,[19] where $\boldsymbol{\omega}_{\mathcal{B}/\mathcal{E}}$ is the angular velocity between the satellite body frame $\mathcal{B}$ and the magnetic field frame $\mathcal{E}$. For a spacecraft with $r = 1$ m, $\omega_{\mathcal{B}/\mathcal{E}} = 1$ deg/sec, and an ECEF orbital velocity of 1 km/sec, the ratio of the transport velocity to the orbital velocity will be less than 10^{-5}. In many scenarios the transport term can be dropped. The force is then:

$$\boldsymbol{F} = \int_B (\boldsymbol{E} + \boldsymbol{v}_o\times\boldsymbol{B})\mathrm{d}q = Q(\boldsymbol{E} + \boldsymbol{v}_o\times\boldsymbol{B}) \tag{2.40}$$

and the torque is

$$\boldsymbol{L} = \int_B \boldsymbol{r}\times(\boldsymbol{E} + \boldsymbol{v}_o\times\boldsymbol{B})\mathrm{d}q = (\boldsymbol{E} + \boldsymbol{v}_o\times\boldsymbol{B})\times\boldsymbol{q} \tag{2.41}$$

This is the exact answer for the torque on a pure dipole in a flat field.[18,20]

2.1.2.3.5   Susceptibilities of the Measures

The expansions for force and torque in the electrostatic two-body problem, radial field, and flat field are useful formula. However, they rely on knowledge of the charge distribution on both bodies in order to perform the integrations and find the measures. Unlike the gravitational two-body problem, these measures change as charge moves throughout the bodies. Recalculating the entire charge distribution for both bodies would be a very intensive process. Here, a method for predicting the measures from parameters that are much more feasible to measure in situ such as the voltage, attitude, and position of each craft is presented.

To do this, a matrix dependent on the relative position and attitude is used to translate the voltage of each craft into a representation of the charge distribution. From this distribution, the measures are formed as functions of the voltage of each craft. There are many ways to make this matrix, including the Method of Moments or Boundary Element Method. A recent addition is the Multi-Sphere Method, which uses hand-tuned parameters for the size and locations of spheres which are constrained to be equipotential.[3,3]

MSM emerged as a way to predict the force and torque with high-enough fidelity to be useful, while also evaluating fast enough to be practical. MSM approximates the satellite as a collection of spheres with variable position and radii. The voltage of any sphere is a function of both its own charge and the charge on neighboring spheres. If these spheres are far enough away to be approximated as point charges, the voltage on the ith sphere is given by:[3,3,18]

$$V_i = \frac{1}{4\pi\epsilon_0}\frac{q_i}{R_i} + \sum_{j=1,j\neq i}^{N} \frac{1}{4\pi\epsilon_0}\frac{q_j}{r_{i,j}} \tag{2.42}$$

Where q_i and R_i are the charge and radius of the ith sphere, respectively, and $r_{i,j}$ is the distance between spheres i and j. If the voltages of each sphere are given by $\boldsymbol{V} = [V_1, V_2, ...V_N]^T$ and the charges are given by $\boldsymbol{Q} = [q_1, q_2, ...q_N]^T$, the relationship between the two is $\boldsymbol{V} = [S]\boldsymbol{Q}$ or $\boldsymbol{Q} = [C]\boldsymbol{V}$, where $[C]$ is the capacitance matrix and $[S]$ is the elastance matrix defined below:[4]

$$[S] = \frac{1}{4\pi\epsilon_0}\begin{bmatrix} 1/R_1 & 1/r_{1,2} & \cdots & 1/r_{1,N} \\ 1/r_{2,1} & 1/R_2 & \cdots & r_{2,N} \\ \vdots & \vdots & \ddots & \vdots \\ 1/r_{N,1} & 1/r_{N,2} & \cdots & 1/R_N \end{bmatrix} \tag{2.43}$$

Since the voltage is assumed known, the charge distribution is found by numerically solving the linear system. If two conductors with n_1 and n_2 spheres each are considered, the elastance matrix can be put into block form:

$$\begin{bmatrix} \boldsymbol{V}_1 \\ \boldsymbol{V}_2 \end{bmatrix} = \frac{1}{4\pi\epsilon_0}\begin{bmatrix} S_1 & S_M \\ S_M^T & S_2 \end{bmatrix}\begin{bmatrix} \boldsymbol{Q}_1 \\ \boldsymbol{Q}_2 \end{bmatrix} \tag{2.44}$$

Where the voltage and charge of each craft are separated. Note that the self elastance terms S_1 and S_2 are much larger than the mutual elastance terms S_M because the inter-sphere separations are much smaller inside one body rather than between the two bodies. Additionally, the self elastance matrices contain the diagonal $1/R$ terms which are larger than the off-diagonal $1/r$ terms. As an example, consider a template box and panel spacecraft with an 8 meter boom made from 248 spheres and a 3×1 meter cylinder made from 138 spheres. The log of the elastance matrix for these two objects with a separation of 40 meters is shown in Figure 2.16.
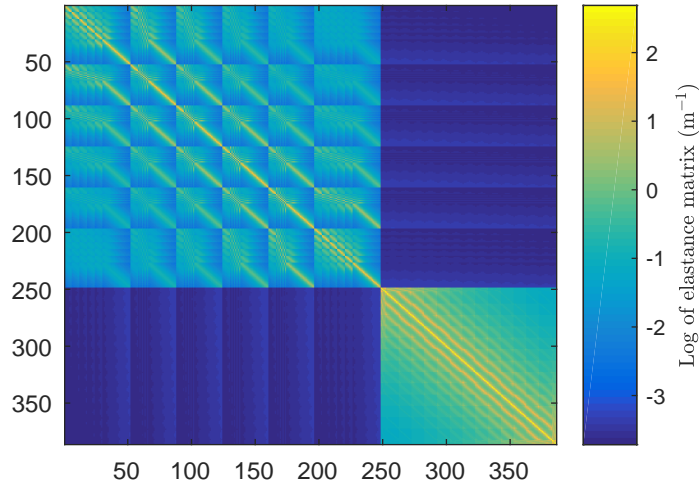
Figure 2.16: *Log of elastance matrix*

There are clearly four blocks, and the diagonals are $10^2 - 10^5$ times larger than the non-diagonal blocks. The blocky structure in the upper diagonal block comes from the method of assembly for the the box and panel spacecraft which is made from six rectangles. In general, the diagonal blocks will not change with relative position or attitude. The blocky structure, symmetry, and the time-fixed properties of the diagonal blocks are exploited when inverting using the Schur complement.

$$\begin{bmatrix} A & B \\ B^T & D \end{bmatrix}^{-1} = \begin{bmatrix} (A - BD^{-1}B^T)^{-1} & -A^{-1}B(D - B^T A^{-1} B)^{-1} \\ -D^{-1}B^T(A - BD^{-1}C)^{-1} & (D - B^T A^{-1} B)^{-1} \end{bmatrix} \tag{2.45}$$

Recognizing that A and D represent the self capacitance matrices, which contain much larger terms than the mutual matrix B, terms second order in B are dropped:

$$\begin{bmatrix} A & B \\ B^T & D \end{bmatrix}^{-1} \approx \begin{bmatrix} A^{-1} & -A^{-1}BD^{-1} \\ -D^{-1}B^T A^{-1} & D^{-1} \end{bmatrix} = \begin{bmatrix} C_1 & -C_1 S_M C_2 \\ -C_2 S_M^T C_1 & C_2 \end{bmatrix} \tag{2.46}$$

Where $[C_i] = [S_i]^{-1}$ for all blocks. The two matrices C_1 and C_2 are not functions of the relative separation and orientation, which means they will be constant in time. The terms in S_M are of the form $1/\|\boldsymbol{R}_c + \boldsymbol{r}_{2_i} - \boldsymbol{r}_{1_j}\|$. Since the center to center separation R_c is much greater than the dimensions of either craft r_1 or r_2, this is approximated as

$$[S_M]_{i,j} = \frac{1}{\|\boldsymbol{R}_c + \boldsymbol{r}_{2_i} - \boldsymbol{r}_{1_j}\|} \sim \frac{1}{R_c} \tag{2.47}$$

Approximating all elements in the mutual capacitance matrix as $1/R_c$ allows the relative attitude to be ignored while still capturing some first-order mutual capacitance and susceptibility. The elastance matrix is now approximately inverted as

$$\begin{bmatrix} \boldsymbol{Q}_1 \\ \boldsymbol{Q}_2 \end{bmatrix} = \frac{1}{4\pi\epsilon_0} \begin{bmatrix} C_1 & -C_1 \mathbb{1}(n_1, n_2) C_2 / R_c \\ -C_2 \mathbb{1}(n_2, n_1) C_1 / R_c & C_2 \end{bmatrix} \begin{bmatrix} \boldsymbol{V}_1 \\ \boldsymbol{V}_2 \end{bmatrix} \tag{2.48}$$

Where $\mathbb{1}(n, m)$ is a matrix consisting of ones of size (n, m). If the two bodies are both conductors,

each MSM sphere is at the same voltage this matrix equation is transformed to a vector equation

$$\boldsymbol{Q}_1 = [C_1]\mathbb{1}(n_1, 1)V_1 - \frac{[C_1]\mathbb{1}(n_1, n_2)[C_2]}{R_c}\mathbb{1}(n_2, 1)V_2 \tag{2.49}$$

$$\boldsymbol{Q}_2 = [C_2]\mathbb{1}(n_2, 1)V_2 - \frac{[C_2]\mathbb{1}(n_2, n_1)[C_1]}{R_c}\mathbb{1}(n_1, 1)V_1 \tag{2.50}$$

Now the charge on each MSM sphere is approximated as a function of a collection of matrices that do not change with state, and the scalar voltage of each craft. The susceptibility of the total charges, dipoles, and charge tensors to the voltage of each craft are found next.

2.1.2.3.5.1   Total Charges

The total charge on each spacecraft is found by summing the charge on each sphere

$$Q = \sum_{i=1}^{n_1} q_i = \mathbb{1}(1, n)\boldsymbol{Q} \tag{2.51}$$

Thus, the scalar charge of body 1 is given by

$$Q_1 = C_S V_1 + C_M V_2 \tag{2.52}$$

Where the self and mutual capacitances are given by

$$C_S = \mathbb{1}(1, n_1)[C_1]\mathbb{1}(n_1, 1) = \sum_{i=1}^{n_1}\sum_{j=1}^{n_1}[C_1]_{i,j} \tag{2.53}$$

$$C_M = \frac{-\mathbb{1}(1, n_2)[C_1]\mathbb{1}(n_1, n_2)[C_2]\mathbb{1}(n_2, 1)}{R_c} = -\frac{\sum_{i=1}^{n_1}\sum_{j=1}^{n_2}[C_1]\mathbb{1}(n_1, n_2)[C_2]}{R_c} \tag{2.54}$$

The scalar self capacitance can be computed with high fidelity using a MSM model with hundreds or thousands of spheres and re-used in each time step for computation. The numerator of the mutual capacitance can be similarly computed at high fidelity and then divided by the norm of the separation vector at each time step.

2.1.2.3.5.2   Dipole Moments

The dipole $\boldsymbol{q}$ is defined in a continuous charge distribution and MSM model as

$$\boldsymbol{q} = \int_B \boldsymbol{r}\mathrm{d}q = \sum_{i=1}^{N}\boldsymbol{r}_i q_i = [R]\boldsymbol{q} \tag{2.55}$$

where $[R]$ is a $3 \times N$ matrix containing the x, y, and z coordinates of each MSM sphere:

$$[R] = \begin{bmatrix} x_1 & \dots & x_N \\ y_1 & \dots & y_N \\ z_1 & \dots & z_N \end{bmatrix} \tag{2.56}$$

The dipole is given by

$$\boldsymbol{q} = \boldsymbol{\chi}_S V_1 + \boldsymbol{\chi}_M V_2 \tag{2.57}$$

Where the self and mutual susceptibilities of the dipole for body 1 are

$$\chi_S = [R_1][C_1]\mathbb{1}(n_1, 1) \tag{2.58}$$

$$\chi_M = \frac{-[R_1][C_1]\mathbb{1}(n_1, n_2)[C_2]\mathbb{1}(n_2, 1)}{R_c} \tag{2.59}$$

Once again, these 3×1 vectors can be computed with high fidelity from SMSM models of each body. Each element in the mutual term must be divided by the separation distance, which may change with time.

2.1.2.3.5.3   Charge Tensor

The charge tensor is defined from a continuous charge distribution or MSM model as

$$[Q] = \int_B -[\tilde{r}][\tilde{r}]\mathrm{d}q = \sum_i^N -[\tilde{r}_i][\tilde{r}_i]q_i \tag{2.60}$$

Define $[R_s]$ as a $3 \times 3N$ matrix containing the cross product matrix of each MSM sphere position and A is a $3N \times N$ matrix used to interweave three copies of the charge vector made from smaller matrices a.

$$[R_s] = \begin{bmatrix} [\tilde{r}_1] \\ \vdots \\ [\tilde{r}_N] \end{bmatrix} \qquad [a] = \begin{bmatrix} 1 \\ 1 \\ 1 \end{bmatrix} \qquad [A] = \begin{bmatrix} a & 0 & \dots & 0 \\ 0 & a & \dots & 0 \\ \vdots & \vdots & \ddots & \vdots \\ 0 & 0 & \dots & a \end{bmatrix} \tag{2.61}$$

The charge tensor is now found as a function of both voltages, and two 3×3 matrices,

$$[Q_1] = [\psi_S]V_1 + [\psi_M]V_2 \tag{2.62}$$

where the self and mutual susceptibilities of the charge tensor for body 1 are given by

$$[\psi_S] = [R_{s_1}]^T \mathsf{diag}([A][C_1]\mathbb{1}(n_1, 1))[R_{s_1}] \tag{2.63}$$

$$[\psi_M] = -[R_{s_1}]^T \frac{\mathsf{diag}([A][C_1]\mathbb{1}(n_1, n_2)[C_2]\mathbb{1}(n_2, 1))}{R_c}[R_{s_1}] \tag{2.64}$$

These matrices can be found using high fidelity MSM models before propagation and the mutual term can be adjusted by dividing by the separation distance. The derivations are done for body 1, but the susceptibilities for body 2 can easily be found by changing all subscript 2s to 1s and vice versa.

2.1.2.3.6   Flat Field Susceptibilities

A flat environmental field will change the charge distribution, but not the scalar charge. The only measures that contribute in a flat field are the dipole and the total charge. The scalar charge is still given by

$$Q = CV \tag{2.65}$$

To find the dipole, write the voltage of each sphere as a function both of the charges and its position relative to the total field $A = E + v \times B$ where v is the velocity with respect to the magnetic field.

$$V = [C]^{-1}Q - [R]^T A \tag{2.66}$$

The charges are found by

$$Q = [C](V - [R]^T A) \tag{2.67}$$

The dipole is then

$$q = \chi_S V_T + [\chi_A] A \tag{2.68}$$

where the self and ambient susceptibilities are given by

$$\chi_S = [R][C]\mathbb{1}(n,1) \tag{2.69}$$
$$[\chi_A] = [R][C][R]^T \tag{2.70}$$

for a model with n spheres. The ambient susceptibility is similar to the electric susceptibility used to calculate the polarization of dielectrics in an electric field.[18]

2.1.2.3.7   Numerical Validation

In a flat field, AFMs and MSM give the same answers down to machine precision assuming the same MSM model is used to calculate the susceptibilities of the measures because there is no truncation of a binomial series. For the two-body problem, the accuracy of predictive AFMs is checked against the truth model of SMSM, which places a large number of equal radius spheres uniformly across the surface of the body. The radius of all spheres is varied to achieve the known self capacitance. Although this method is slower to evaluate (due to the much larger number of spheres), it removes the need for hand tuning and has good accuracy relative to commercial FEA software.[2] An example SMSM model for two template "box and panel" spacecraft in close proximity is shown in Fig. 2.17. Note that charge, which is shown as color, tends to bunch up at the corners of conductors and is affected by the nearby spacecraft.
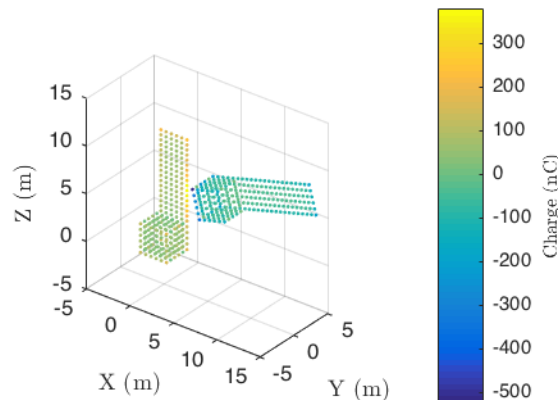
Figure 2.17: *Example SMSM configuration for two satellites*

For validation, one "box and panel" spacecraft has fixed location and attitude at the origin of the coordinate system. The second spacecraft occupies many different positions and attitudes on a shell of a given radius. SMSM is used to find the force and torque on the fixed craft. The force and torque is also predicted using AFMs with the susceptibilities $C_S, C_M, \chi_S, \chi_M, [\psi_S]$, and $[\psi_M]$ for each craft found before computation from the same 256-sphere SMSM model. The average percent error is computed for each spherical shell. The percentage error is computed as:

$$PE = 100 * \frac{||\boldsymbol{a}_{\mathsf{AFM}} - \boldsymbol{a}_{\mathsf{T}}||}{||\boldsymbol{a}_{\mathsf{T}}||} \tag{2.71}$$

Where a is either the force or torque, and the subscript "T" indicates the truth model.

The second craft is placed at points on a spherical shell precomputed using a golden spiral algorithm[9] which arranges 20 points equidistantly on the surface of a sphere. The shells are varied in radius logarithmically from 15 to 200 meters in 10 steps. The attitude of the second object at each of these points is changed using three random Euler angles while the first object is held fixed in attitude at the origin. The mean percentage error per shell is shown in Figure 2.18

(a) Force percent error   (b) Torque percent error
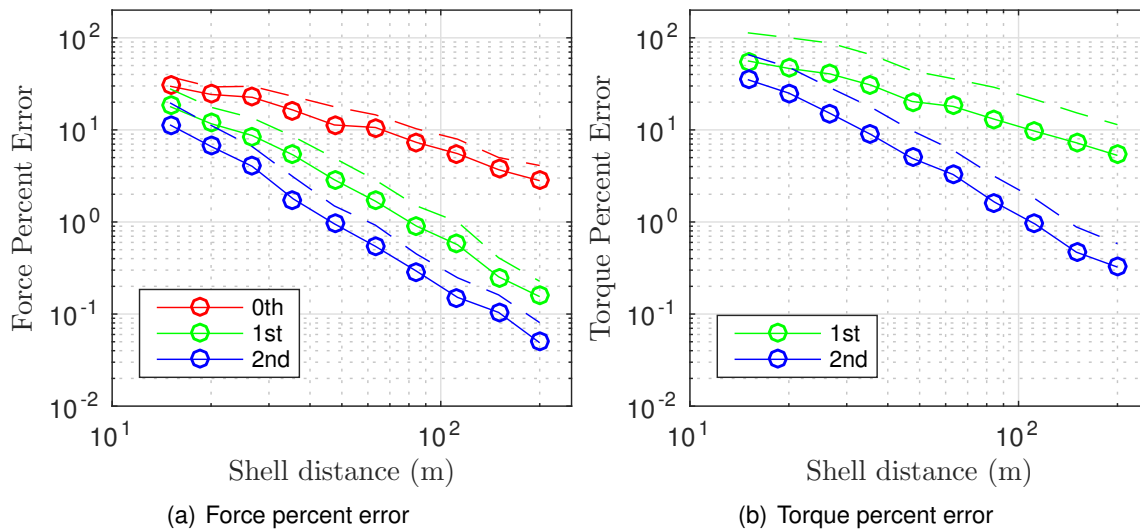
Figure 2.18: *Percentage errors for force and torque using predictive AFMs*

The mean percentage error for the zeroth, first, and second order expressions for force are shown as red, green, and blue lines in the force plot. Since there is no zeroth order term for torque prediction, only the first and second order expressions are shown in the torque plot. A dashed line is shown 1 standard deviation above each of these to give a sense of the variation a user should expect.

The errors are initially very high, a few hundreds of percent, but they drop quickly as the spacecraft move farther apart. Since the AFM derivation hinges on the assumption that the spacecraft sizes are much smaller than the distance between them, this matches intuition. The second order term for force drops below 5% error at 25 meters and the second order term for torque drops below 5% at 48 meters.

2.1.2.4   Analysis and Applications

There are many numerical methods for electrostatic force and torque prediction for conductors. However, they do not give good analytical forms for force and torque. This section summarizes previous work that curve fit the angular and voltage dependencies of electrostatic torque, and then uses AFMs to analytically predict the same result. Next AFMs are used to predict the torque in the case where the center of mass is not aligned with the exact center of the target object.

Bennett et. al. used MSM to calculate the torque on a 3×1 meter target cylinder due to a spherical tug craft for different voltages and angles.[21] This set up is shown in Fig. 2.19. The cylinder has the same voltage magnitude as the sphere, and is always positive while the tug
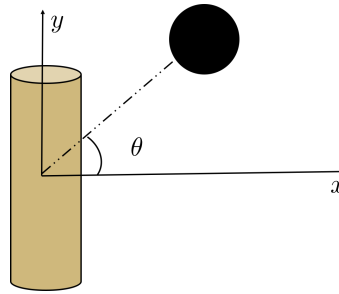
Figure 2.19: *Coordinate system for example analysis*

sphere can change the polarity of its voltage: $V_2 = |\phi|, V_1 = \phi$. The torque is only about the z axis due to the symmetry, and is shown as a function of both the angle θ and the voltage ϕ. This plot is shown for near field (2.5 meter separation) and far field (15 meter separation) cases in Fig. 2.20. The voltage dependance follows a quadratic relationship, and the angular dependance is well approximated by $\sin(2\theta)$. The torque is then curve fit to be:[21]

$$L = \gamma f(\phi)g(\theta) = \gamma \phi |\phi| \sin(2\theta) \tag{2.72}$$

In the near field, γ divides into a larger value for attraction γ_a and a smaller value for repulsion γ_r. At further separations the difference between attraction and repulsion is less evident.

(a) Separation $d = 15$ m   (b) Separation $d = 2.5$ m
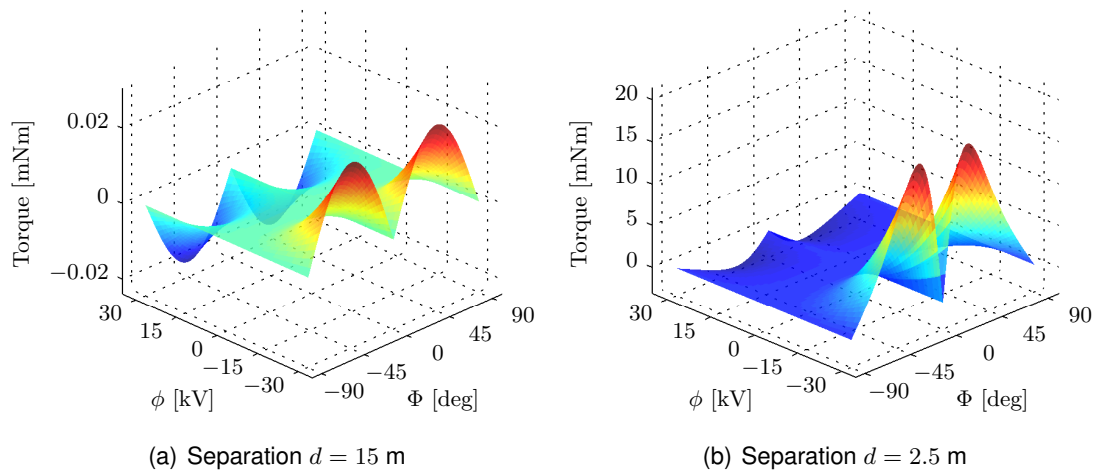
Figure 2.20: *MSM torque surfaces at a separation distances of $d = 2.5$ m and $d = 15$ m for $V_1 = \phi$ and $V_2 = |\phi|$.[21]*

The angular, voltage, and attraction/repulsion trends that have been empirically found using MSM are now derived using AFMs. Referencing Eq. 2.38, the torque on a general body due to a nearby point charge is given by

$$\boldsymbol{L}_2 = \frac{Q_1}{4\pi\epsilon_0 R_c^3}\left[\boldsymbol{q}_2 + \frac{3}{R_c^2}[Q_2]\boldsymbol{R}_c\right] \times \boldsymbol{R}_c \tag{2.73}$$

re-writing this in terms of susceptibilities gives:

$$\boldsymbol{L}_2 = \frac{C_{S1}V_1 + C_M V_2}{4\pi\epsilon_0 R_c^3}\left[(\boldsymbol{\chi}_S + \frac{3}{R_c^2}[\psi_S]\boldsymbol{R}_c)V_2 + (\boldsymbol{\chi}_M + \frac{3}{R_c^2}[\psi_M]\boldsymbol{R}_c)V_1\right] \times \boldsymbol{R}_c \tag{2.74}$$

This equation is grouped into four separate terms

$$\boldsymbol{L}_2 = \frac{1}{4\pi\epsilon_0 R_c^3}\left[C_M(\boldsymbol{\chi}_S + \frac{3}{R_c^2}[\psi_S]\boldsymbol{R}_c)V_2^2 + C_{S1}(\boldsymbol{\chi}_M + \frac{3}{R_c^2}[\psi_M]\boldsymbol{R}_c)V_1^2\right.$$
$$\left. + (C_{S1}(\boldsymbol{\chi}_S + \frac{3}{R_c^2}[\psi_S]\boldsymbol{R}_c) + C_M(\boldsymbol{\chi}_M + \frac{3}{R_c^2}[\psi_M]\boldsymbol{R}_c))V_1V_2\right] \times \boldsymbol{R}_c$$
$$= \boldsymbol{A}V_1^2 + \boldsymbol{B}V_2^2 + (\boldsymbol{C} + \boldsymbol{D})V_1V_2 \tag{2.75}$$

In this this 1-D case the torque is purely about the z axis and is written using scalars as

$$L = AV_1^2 + BV_2^2 + (C + D)V_1V_2 \tag{2.76}$$

The terms A and B have one mutual term and are thus 1$^{\text{st}}$ order in $(1/R_c)$, C is 0$^{\text{th}}$ order, and D is 2$^{\text{nd}}$ order. This means that in the far field terms linked to C will persist longer than those linked to A and B, which will persist longer than those linked to D. Because the mutual susceptibilities $(C_M, \boldsymbol{\chi}_M, [\psi_M])$ are negative but the self susceptibilities are positive, A, B and D are negative, but C is positive and larger than D.

Thus the following development switches to the positive variables $F = |A + B|$ and $G = C + D$, and makes use of the definitions $V_1 = \phi, V_2 = |\phi|$ to match prior work.[21] The torque for attractive (L_a) and repulsive (L_r) cases is given by:

$$L_r = (-F + G)\phi^2 = (-F + G)\phi|\phi| \tag{2.77}$$
$$L_a = (-F - G)\phi^2 = (F + G)\phi|\phi| \tag{2.78}$$

In the attractive cases the magnitude of the torque is larger because F and G add rather than subtract. This can be seen empirically in Fig. 2.20(a). Additionally, since G has the highest order term, it will matter most in the far field. Since F matters less in the far field, the difference between the attractive and repulsive torque decreases in the far field, which can also be seen by comparing Fig. 2.20(a) and 2.20(b).

In prior work Reference[21] numerically fit the far field parameter γ to a value of $2.234 * 10^{-14}$ for a 3 meter by 1 meter cylinder 15 meters away from a 1 meter diameter sphere. To compute the corresponding value from AFMs, assume that the center of mass is perfectly aligned with the center of charge so that $\boldsymbol{\chi}_S = 0$ and the body axes are aligned so that $[\psi_S]$ is given by diag(ψ_B, ψ_s, ψ_B), where $\psi_B > \psi_s$. This represents the case of a perfectly axis-symmetric cylinder as shown in Figure 2.19. Ignoring the mutual part of G which decays quickly gives the torque as

$$L = \frac{-3C_{S1}}{4\pi\epsilon_0 R_c^5}\tilde{\boldsymbol{R}}_c[\psi_S]\boldsymbol{R}_c V_1 V_2$$
$$= \frac{3C_{S1}}{8\pi\epsilon_0 R_c^3}(\psi_B - \psi_s)\sin(2\theta)V_1V_2\hat{\boldsymbol{z}} \tag{2.79}$$

where G is defined as

$$G = \frac{3C_{S1}}{8\pi\epsilon_0 R_c^3}(\psi_B - \psi_s) \tag{2.80}$$

SMSM is used to find the values of ψ_S and ψ_B which gives $G \approx 2.531 * 10^{-14}$, only a 13% difference with the numerically fit value used in Reference [21]. These two results agree well considering that only a second order AFM model is used and the mutual part of G is ignored, and Reference [21] fits γ to the full MSM solution.

Now consider the same cylinder, but allow the center of mass to move within the craft by a few centimeters along the y axis ($\boldsymbol{\chi}_S = [0, \chi_S, 0]^T$). The torque is still only about the z axis and is given by

$$\begin{aligned}
\boldsymbol{L}_2 &= \frac{-C_{S1}}{4\pi\epsilon_0 R_c^3} \tilde{\boldsymbol{R}}_c \Big(\boldsymbol{\chi}_S + \frac{3}{R_c^2}[\psi_S]\boldsymbol{R}_c \Big) V_1 V_2 \\
&= \frac{-C_{S1}}{8\pi\epsilon_0 R_c^2} \Big[\chi_S \cos(\theta) + \frac{3(\psi_B - \psi_s)}{2R_c}\sin(2\theta) \Big] V_1 V_2 \hat{\boldsymbol{z}}
\end{aligned} \tag{2.81}$$

Setting $\chi_S = 0$ recovers Eq. (2.79), but even a small CM offset can make the $\cos(\theta)$ term dominate, especially at large separations. As the CM moves away from the geometric center, χ_S grows linearly, and some elements of ψ_S grow quadratically. The torque as a function of θ is shown for a variety of CM offsets in the example of the same cylinder 15 meters away from a 1 μC point charge in Figure 2.21. The different curves are for different values of χ_S – the center of mass offset is shown in the legend.
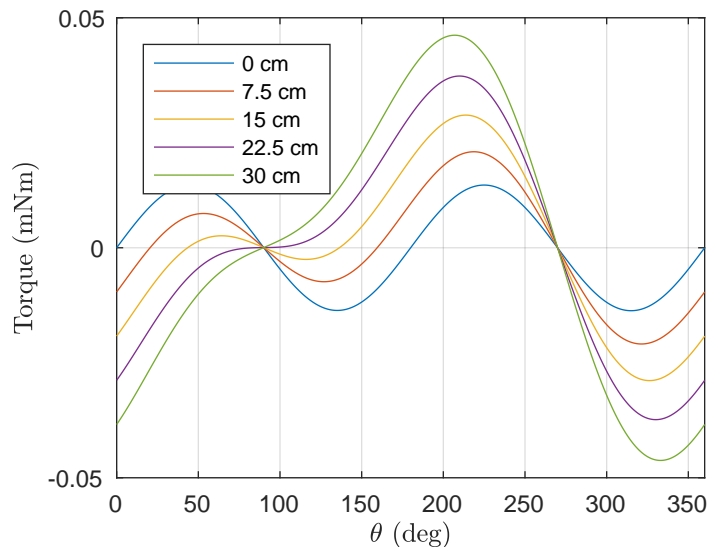
Figure 2.21: *Torque on cylinder for a variety of center of mass offsets*

The torque slowly changes from a perfect $\sin(2\theta)$ to an augmented $-\cos(\theta)$ curve as the CM offset varies. The magnitude of the torque also increases by a factor of 3.38. This factor is even greater at further separations since the $\cos(\theta)$ term has lower order in $1/R_c$. Knowledge of center of mass to center of charge differences are essential for the stability of control laws used for de-spinning of passive space debris. If the center of charge location is not properly accounted for, the sign of the predicted torque can be wrong, leading to instabilities in the closed-loop control discussed in Reference.[21]

2.1.3   Charged Orbital Perturbation Analysis using Appropriate Fidelity Models

2.1.3.1   Motivation

The dominant effects of space weather on satellite orbits are density variations which affect satellite drag in Low Earth Orbit (LEO) at altitudes between 300 and 1500 km, and spacecraft charging

at Geosynchronous Earth Orbits (GEO). Spacecraft charging can lead to arcing, which can damage solar panels and damage spacecraft electronics. The SCATHA mission showed that charging naturally to 10's of kilo-volts in Earth's shadow is possible.[22,23] If the spacecraft is not continuously conducing, different parts of the spacecraft can charge to different levels and arc, which can damage spacecraft electronics.[24] However, recent work by[1,25–27] suggests that spacecraft charging can affect the orbits of lightweight debris objects as well. This has major implications for those wishing to track debris objects in GEO to prevent collisions. This is especially important as lightweight debris from the "graveyard" GEO orbit can easily drift back into the operational GEO orbit and threaten valuable space assets. Additionally, understanding this possible new link between space weather and GEO orbital perturbations has the possibility to benefit both fields.

Spacecraft are subject to a number of small forces that perturb their orbits from the closed-form conic section solution to the two body problem. At low altitudes, Earth's spherical gravity and drag strongly perturb certain orbits. Further out in GEO, all objects are perturbed by lunar and solar gravity, and some High Area-to-Mass (HAMR) objects are strongly perturbed by Solar Radiation Pressure (SRP).[28] However, not all orbits are explained using just the above perturbations,[29] reports some near-GEO debris objects which appear to accelerate *towards* the sun during the propagation interval, which is impossible with only SRP disturbances. The primary source of this discrepancy is postulated to be that these objects are interacting with Earth's magnetic field.
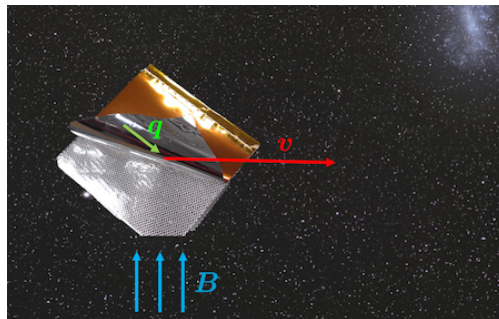
Figure 2.22: *Electromagnetic perturbations acting on charged MLI*

Some of these unknown objects are thought to be torn-off pieces of Multi-Layer Insulation (MLI) as discussed by.[30] Samples returned from the Hubble Space Telescope showed cracks in areas of constrained loading, and[31] discuss a tendency of MLI to curl up when peeling off.[22] discuss how GEO spacecraft could charge to very high potentials during geomagnetic storms. This charging causes a translational Lorentz force, and may cause a significant electrostatic torque depending on the relative distance between the center of charge and center of mass. Additionally, if the object is rotating relative to an external magnetic field it will experience an eddy current torque.

Reference 25 is the first publication with results modeling the electrostatic charging effects on HAMR objects. This initial work adds the Lorentz force and eddy torque to the more standard list of perturbations for a HAMR plate. Including these two new effects changes the orbit by nearly a tenth of a degree in inclination and 0.002 in eccentricity after only 12 hours.[26] model a sphere for which torques are not included and found much less dramatic results.[27] consider a rigid plate similar to,[25] but included electrostatic torques and found that the main method that charging affects orbits is through the torques rotating the object so that the SRP pushes on it differently.

This work builds off the dynamical insights gained from References 26 and 27 by adding a more realistic charging model. In particular, the orbit averaged GEO space weather variations are taken into account as well as the convection E field. Finally, a statistical analysis over initial attitude is performed to study the relative sensitivity of the electrostatic and eddy current disturbance relative

to other orbital perturbations. In Reference 27 a worst case charging environment of 30 kV is assumed for the entire orbit. In this work, measured flux distributions at every local time are used to compute the equilibrium charging level at that point in the orbit. Additionally, this work considers a more complex debris object than a square plate or sphere: a thicker piece of MLI consisting of two separate pieces of aluminized mylar electrically separated by a piece of non-conducting tule. MLI normally has more than 40 layers of metalized sheets and mesh as shown in Fig. 2.23 but in this work only the three layer system is considered. This 2 conductor system has the interesting property that one conductor is in the sunlight at all times and one is shaded. The presence of sunlight is very important for spacecraft charging with most objects charging a few volts positive in the sunlight and very negative in shade.

Figure 2.23: *Multi Layer Insulation with non-conducting mesh shown*

The statistical analysis looks at the relative impacts between including electromagnetic perturbations and uncertainty in the initial attitude. In contrast, Reference 27 varies the initial attitude, but no analysis over how the size of the initial attitude change relates to the propagation model used is made. This work is done by first reviewing the space environment at GEO in both calm ($K_P = 2-$) and stormy ($K_P = 8$) conditions, then evaluating the spacecraft charging considering the statistical flux distributions to compute the currents. Next, methods for computing the new electromagnetic perturbations are reviewed with special emphasis on the debris object in question. The debris object is then propagated in a full attitude-dependent, 6 degree-of-freedom simulator to investigate the change in dynamics from including or neglecting electromagnetic perturbations. The goal of this paper is a detailed discussion of how space weather conditions can impact the lightweight GEO debris astrodynamics.

2.1.3.2   The Space Environment

The Geosynchronous orbit regime lies near the boundary between the inner and outer magnetosphere at a radius of $\sim$6.6 Earth radii or 42,164 km. The motion of the plasma in the inner magnetosphere is governed mainly by curvature and gradient drift, while the outer magnetosphere transitions to the global magnetospheric convection cycle. For the purposes of spacecraft charging, the electron and ion populations are usually described as bi-Maxwelllian distributions.[32] Some common space weather model parameters are shown Tab. 2.8. Here n_e is the electron density, n_i is the ion density, and kT_e and kT_i are the electron and ion temperatures. The worst case model is a single Maxwellian while the ATS-6 fit and the Day in the Life (DITL) models are double Maxwellian.[32] The drawback of these models is that they provide fixed nominal values, where the actual GEO space weather conditions will vary across the orbit even at a fixed K_P index. Additionally, measured flux distributions are very non-Maxwellian.

    Reference 33 presents an empirical model that uses 82 satellite-years of observed electron

Table 2.8: *Parameters for commonly used Maxwellian fits for GEO plasma[32]*

Model	n_e (cm^{-3})	kT_e (keV)	n_i (cm^{-3})	kT_i (keV)
Worst Case	1.1	12	0.24	29
ATS-6	1.2, 1.2	16, 1	0.24, 8.82e-3	29.5, 0.111
DITL	0.3, 0.2	4,7	0.3, 0.2	4, 7

and ion flux data. Both populations are measured by Magnetospheric Plasma Analyzers (MPAs) on board multiple Los Alamos National Labs (LANL) satellites. The MPAs are capable of measuring the flux between 1 eV and 40 keV in three spatial dimensions every 86 seconds. All of this data over the 82 satellite-years of data is tagged with local time (LT), K_P index, and solar wind electric field (vB_z). Denton's model allows users to specify three inputs (Energy, LT, and K_P or vB_z) and outputs the mean, median, and percentile flux values. K_P is a measure of the severity of geomagnetic storms and varies from 1 to 9 with three steps within each number, so 3+ is worse than 3, which is worse than 3-. This work considers the a DITL case where $K_P = 2-$ and a severe storm with $K_P = 8$. The statistical mean electron fluxes for GEO are shown in Fig. 2.24, with the
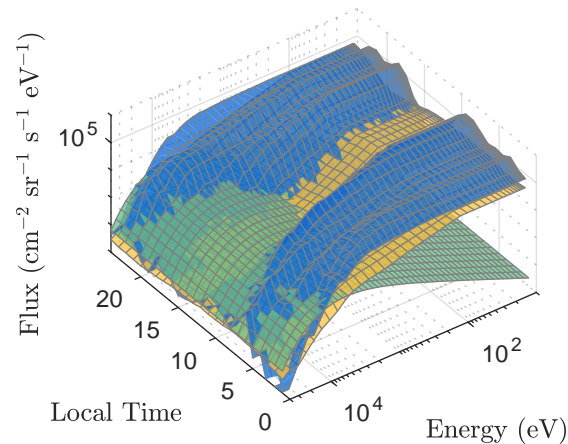
Figure 2.24: *Electron Fluxes at GEO for $K_P = 2-$ (yellow), K_P = 8 (blue) as well as a Maxwellian fit (green)*

yellow sheet indicating $K_P = 2-$, the blue sheet for K_P = 8, and the green sheet the Maxwellian fit for a DITL condition as shown in Tab. 2.8. The measured flux at low energies will be a combination of the natural space environment and the secondary and photoelectrons generated by the spacecraft itself. To avoid double-counting these electrons, the flux at all energies below 100 eV is reassigned to the flux at 100 eV which is why the surfaces are flat respect to energy below 100 eV in Fig. 2.24.

The storm conditions differ in many ways from the quiet condition - the flux is higher nearly everywhere, except for local times near 12, which corresponds to the sun line. The shape of the flux in energy space is also different with more flux at higher energies during a storm. Both of these measurements differ significantly from the Maxwellian fit. In the low energy region, the Maxwellian grossly underestimates the flux by 5 orders of magnitude. In the high energy region the Maxwellian overestimates the flux, but not by nearly as large of a factor. The statistical mean ion fluxes for GEO are shown in Fig. 2.25, with the yellow sheet indicating $K_P = 2-$, the blue sheet
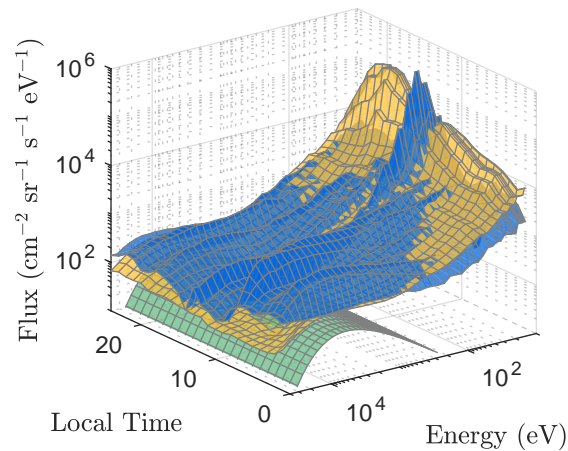
Figure 2.25: *Ion Fluxes at GEO for K_P = 2- (yellow), K_P = 8 (blue) as well as a Maxwellian fit (green)*

for K_P = 8, and the green sheet the same Maxwellian DITL fit but for ions. Once again, the storm time flux is greater than the quiet time flux, but unlike the electrons, this trend is more dramatic at high energy. At low energy the storm flux is actually lower. In Local Time, the trend seen in the electrons is reversed - there are more ions clustered near 12:00 during a storm. The Maxwellian fit is radically different from the measured data, but does get the order of magnitude approximately correct in the 10 keV region.

2.1.3.3 Spacecraft Charging

A space object is subject to many currents from the space plasma and the sun. The currents considered here are the thermal electron and ion currents (I_e, I_i) from the plasma, secondary electron emission (SEE) from both electrons and ions (I_{SEE_e}, I_{SEE_i}), electron backscattering (I_b), and the photoelectric current (I_{ph}) if the object is sunlit. The sign convention is for the currents to the spacecraft - so all currents except for the electron thermal current are positive. The object is in equilibrium when the net current to it is zero:

$$I_{\mathsf{e}}(\phi) + I_{\mathsf{i}}(\phi) + I_{\mathsf{SEE}_e}(\phi) + I_{\mathsf{SEE}_i}(\phi) + I_b(\phi) + I_{\mathsf{ph}}(\phi) = 0 \tag{2.82}$$

All these currents are functions of the object's voltage ϕ as well as many other parameters. Since the charging times for the objects considered here are so short, the object is always considered to be in equilibrium with its environment. Therefore, for each set of environmental conditions, the appropriate voltage can be prescribed by finding the voltage that drives the net current to zero. Each of the currents are discussed in detail in the following subsections.

2.1.3.3.1 Electron and Ion Currents

Electrons and ions impact the spacecraft, electrons causing a negative current and ions stealing an electron and causing a positive current. The magnitude of these currents is dependent on the amount of ions and electrons in the environment as well as the voltage of the spacecraft. For a flux distribution over energy $F(E)$, the current is

$$I(\phi) = q_0 A 4\pi \int_L^\infty \left(\frac{E}{E \pm \phi} \right) F(E \pm \phi) dE \tag{2.83}$$

Where q_0 is the particle charge, A is the area exposed to the plasma, and ϕ once again is the spacecraft potential. The lower bound of the integral L is 0 for the repelled particle, and $|\phi|$ for the attracted particle. Ions take the upper sign and electrons take the lower. If a Maxwellian distribution is used, the integral can be solved analytically and the current is given by:

$$I(\phi) = \begin{cases} I_0(1 + \frac{q_0\phi}{kT}) & \text{Attracted} \\ I_0 e^{q_0\phi/kT} & \text{Repulsed} \end{cases} \tag{2.84}$$

where kT is the thermal energy of the plasma, q_0 is the fundamental charge, and I_0 is the current when the spacecraft is at 0 V, found from the parameters in the Maxwellian distribution. The dominant trends are linear attraction with a characteristic voltage equal to the temperature of the Maxwellian, and exponentially decreasing repulsed current.

In this analysis, measured flux distributions are used and these integrals are done numerically using an adaptive quadrature integration program that uses linear interpolation on the flux data. The flux data is logarithmically spaced in 40 increments for $K_P = 2$ and 50 increments for $K_P = 8$ as shown in Figs. 2.24 and 2.25. The lower bound for the attracted particle is $|\phi| + 0.1$ V to avoid a singularity, and since data for $F(E)$ only exists up to 40 keV for the distributions used, the upper bound is taken as $40,000$ V $+ \phi$.

2.1.3.3.2   Secondary Electron Emission and Backscattering Current

2.1.3.3.2.1   General Secondary Electron Emission

When an electron or ion impacts a material, it deposits much of its energy in the first few nanometers of the material. Some of this energy goes into freeing electrons near the surface which can be ejected. This phenomena is referred to as Secondary Electron Emission (SEE) and can significantly reduce the net electron thermal current and amplify the ion thermal current. Additionally, there is a chance that an electron will bounce off the material rather than sticking. This phenomena is called "backscatter". The probability that an electron will backscatter is given by η, the expected number of secondary electrons generated is typically given by δ, and the total yield as Y. Since the total yield is a function of energy, it must be integrated over the distribution to find the current:

$$I(\phi) = q_0 A 4\pi \int_L^\infty Y(E)\left(\frac{E}{E \pm \phi}\right)F(E \pm \phi)dE \tag{2.85}$$

Typically, rather than calculating the actual current the mean yield $< Y >$ is used which is the effective yield for a particular distribution.

$$< Y > = \frac{I_Y}{I} = \frac{\int_L^\infty Y(E)\left(\frac{E}{E\pm\phi}\right)F(E \pm \phi)dE}{\int_L^\infty \left(\frac{E}{E\pm\phi}\right)F(E \pm \phi)dE} \tag{2.86}$$

Since $< Y >$ is constant for the repulsed particle if the distribution is Maxwellian, and very little variation for the attracted particle, $< Y >$ is often treated as a constant. In this analysis It is treated as a function of the changing distribution (via LT) and the spacecraft voltage ϕ which shifts the distribution. Once again, this integral is done numerically using an adaptive quadrature integration program. The integration limits are the same as in the preceding subsection. The SEE function δ for both ion and electron impact as well as the backscattering function η are discussed next.

2.1.3.3.2.2   Electron-Induced SEE

The electron-induced SEE yield is typically low at low landing energies, then it rises to a large value, often larger than 1, for intermediate energies around a few hundred eV, then falls back to a small yield for keV energies. If the maximum yield is larger than 1, there will be an incident energy region where incident electrons can cause a net positive current. In this work, the "universal curve" of Lin and Joy[34] is used:

$$\delta(E) = \delta_M 1.28 \left(\frac{E}{E_M}\right)^{-0.67} \left(1 - \exp(-1.614(E/E_M)^{1.67})\right) \tag{2.87}$$

Where δ_M is the max yield, and E_M is the energy at which it occurs. For aluminum, the parameters $\delta_M = 0.97$ and $E_M = 400$ eV are used.

2.1.3.3.2.3   Electron backscattering

Backscattering occurs when an electron is reflected from the spacecraft rather than absorbed. This analysis uses the model provided by the Nascap Scientific Documentation for energy-dependent backscattering:[32]

$$\eta(E) = \left(\frac{H(1-E)H(E-0.05)\log(\frac{E}{0.05})}{\log(20)} + H(E-1)\right) \times (\frac{e^{-E/5}}{10} + 1 - (2/e)^{0.037Z}) \tag{2.88}$$

Where E is the landing energy in keV, $H(x)$ is the Heaviside step function, and Z is the atomic number of the material (aluminum in this analysis). The formulas above can be added to produce the total yield $Y(E) = \eta(E) + \delta(E)$ for normally incident monoenergitic electrons.

2.1.3.3.2.4   Ion-Induced SEE

Ions may also cause SEE, and for many materials the number of secondaries caused by ions is much larger than that caused by electrons. However, since the ion current is usually much smaller than the electron current, ion-induced SEE is neglected in many cases. In this analysis the two parameter Nascap model[32] is used:

$$\delta(E) = \frac{\beta E^{1/2}}{1 + E/E_M} \tag{2.89}$$

Where E is the energy in keV, and for aluminum $\beta = 1.36$ and $E_M = 40$ are fitting parameters.

2.1.3.3.2.5   Mean Yields

The above formulas for SEE and backscattering are inserted into Eq. (2.86) to calculate $< Y >$ for electrons and ions as a function of both space weather and local time for both space weather conditions. This is shown in Figs. 2.26 and 2.27.

Fig. 2.26 shows the electron yields for stormy and calm space weather conditions. The effective yield is zero for a positive craft since although secondaries are generated, they are re-collected by the craft. The yield is always less than 1, but it gets very close for low voltages where there are still a lot of low energy particles. The dependence on local time is much more dramatic during the storm, which matches the higher dependence for the flux. At local noon, the storm yields
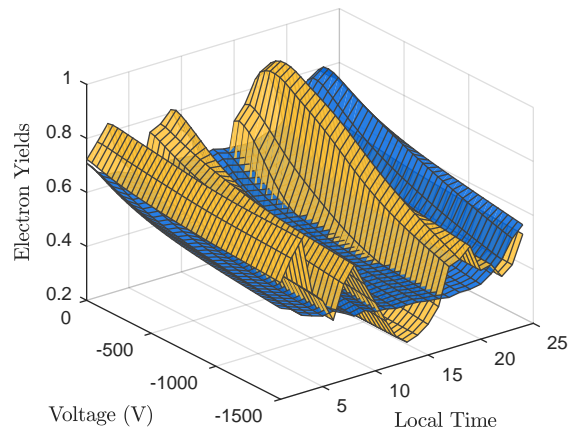
Figure 2.26: *Electron-Induced yields for K_P = 8 (orange), K_P = 2 (blue) as a function of Local Time and voltage*

are lowest, which matches the depleted low energy section of the flux. Although the local time dependence for the flux is low in the morning and afternoon/night sectors in the flux, the yields have high dependence there.

Fig. 2.27 shows the ion yields, which are much higher than the electron yields, although since the incident ion flues are much lower this current is smaller than the electron-induced yields. There is a huge dip around local noon for the storm case, just as with the electron yields. Since the peak for ion-induced SEE is at much higher energies in the keV range, this matches the increase in low energy ions and decrease in high energy ions observed around local noon.
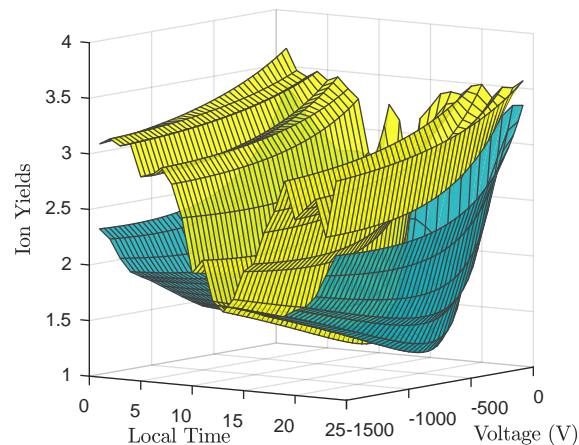

Figure 2.27: *Ion-Induced yields for K_P = 2 (teal), K_P = 8 (yellow) as a function of Local Time and voltage*

2.1.3.3.3   Photoelectric Current

Energy from the sun can energize electrons in the first few nanometers of the spacecraft so that they leave the surface. The fraction that have enough energy to escape the potential well of

the spacecraft cause a net positive current given by:[35]

$$I_p = \begin{cases} j_{\mathsf{ph}} A \cos(\theta) e^{-q\phi/k_{\mathsf{B}}T_{\mathsf{ph}}} & \phi > 0 \\ j_{\mathsf{ph}} A \cos(\theta) & \phi \leq 0 \end{cases} \tag{2.90}$$

Where j_{ph} is the photoelectron flux, A is the area, θ is the angle of incidence, and $k_{\mathsf{B}}T_{\mathsf{ph}}$ is the thermal energy of the ejected photoelectrons. For aluminum, $k_{\mathsf{B}}T_{\mathsf{ph}} = 2$ eV and $j_{\mathsf{ph}} = 40$ μA/m^2. For a negative spacecraft this current is constant, and for a positively charged spacecraft it quickly vanishes.

2.1.3.3.4 Equilibrium Voltage

Equation (2.82) can be solved at each local time and each sun facing angle θ to provide a look-up table to interpolate and determine the voltage of both plates at any point in the orbit. Assuming the voltage to always be at the equilibrium value is justified since the relevant capacitance $C = C_S + C_M = 24.9$ pF is small enough that the charging time is short compared to the orbital times. The parameters C_S and C_M will be discussed in greater detail in the following section.
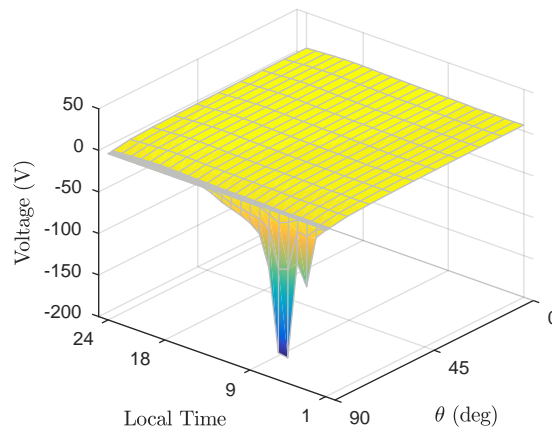
Figure 2.28: *Equilibrium voltage for $K_P = 2-$ as a function of sun incidence angle and local time*

Figure 2.28 shows the equilibrium voltage for aluminum as a function of local time and sun incidence angle. An angle of 90 or greater indicates that the object is shaded, and has no photo-electric current. Most of the charging happens in the absence of sunlight, and in the early morning sector when LT is between 0 and 6. This matches intuition as high energy electrons cluster in that region due to their drifts. The most negative voltage occurs when the spacecraft is entirely shaded and at a local time of 5, and is -169 V. For $\theta < 88°$, the voltage varies between 5 and 10 V positive as expected for a sunlit object in calm space weather.

Figure 2.29 shows the equilibrium voltage in the same format as Fig. 2.28 but for the stormy condition of $K_P = 8$. Again, most of the charging occurs for shaded or almost shaded angles, although the minimum angle moves down by a few tenths of a degree. The charging occurs in the early morning sector, but also very dramatically in the late night sector where LT is between 20 and 24. The charge levels are much lower here as well, dropping to -1.911 kV at LT = 6 and -1.844 kV at LT = 22. Additionally, the voltage stays below -1 kV for the entire sector between LT = 20 and 24. There is good intuition for the existence of high charging in the early morning sector due to the electron drift, but the strong charging in the late night sector is unexpected. Once again, the

fully sunlit voltages range between 5 and 10 V positive. Since one plate is always shaded and the plates are electrically disconnected one plate is always negative.

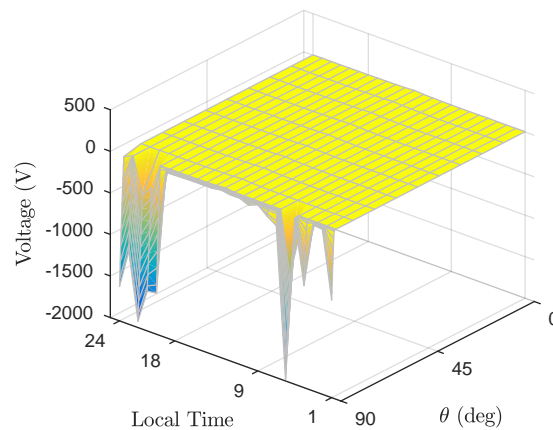**Figure 2.29:** *Equilibrium voltage for K_P = 8 as a function of sun incidence angle and local time*

These results for voltage must be taken with a grain of salt as they depend on a number of parameters. Firstly, the photoemission for aluminum is chosen as the round number of 40 μA/m^2 to match that used by Nascap. Second and most importantly, the model parameters for electron-induced SEE have a good amount of variability. The max yield used here of 0.97 and in Nascap is reported as 2.0 by Reference 34 and found experimentally to be near 2.5 by Reference 36. Additionally, Balcon et. al. found that the SEE parameters had strong dependence on the angle of incidence (an electron that has grazing incidence creates more secondaries since it deposits more energy close to the surface where the secondaries have a better chance or escaping). There is also dependance on the surface condition (smooth or rough) and the temperature of the sample.

If a maximum yield of of 2.0 is used, the most voltages range from 0 to 17 V positive even in shade. This is because the net electron yield is greater than 1, and the instant the spacecraft starts to charge negative the SEE current turns on and pushes it back to positive since the secondary electrons can now escape the system. With these much less dramatic voltages, the resulting electrostatic perturbations are much more subdued.

2.1.3.4   Propagation Model

Consider a small piece of torn off MLI 50 cm by 50 cm like that shown in Fig. 2.23. It is composed of just 3 layers: 2 layers of aluminized mylar 1/4 mil thick with a non-conducting piece of Dacron netting 0.16 mm thick in between. The total mass of this thin sheet is just 6.225 grams, but it's large surface area of 0.25 m^2 gives it an area to mass ratio (AMR) of 40.16 m^2/kg. All MLI parameters are taken from Reference 37. The center of mass is assumed to be offset from the center of pressure by [2.5, 2.5, 0] cm. The center of charge is assumed to be offset from the center of mass by [-2.5, -3.33, 0] cm. The inertia tensor is computed assuming constant density.

The primary force for macro sized objects in Earth orbit it the Earth's gravity. There are several small forces and torques which perturb the orbits of many small objects such as Solar Radiation Pressure (SRP), Earth's non point mass gravity, and the gravitational pull of the sun and moon. This work includes three new electromagnetic perturbations - the Lorentz force, the Lorentz torque, and Eddy current torques. All perturbations are listed in Table 2.9 with either the exact equation or a short description.

Table 2.9: *Forces and Torques acting on Space Debris*

Perturbation	Force	Torque
Earth gravity	Spherical Harmonics	$\boldsymbol{L} = \frac{3\mu}{R_c^5} \boldsymbol{R}_c \times [I]\boldsymbol{R}_c$
Lunar gravity	point-mass gravity	0
Solar gravity	point-mass gravity	0
SRP	ASD reflection	$\boldsymbol{L} = \boldsymbol{r}_{\text{sep}} \times \boldsymbol{F}_{\text{SRP}}$
Electrostatic	$\boldsymbol{F} = Q\boldsymbol{v} \times \boldsymbol{B}$	$\boldsymbol{L} = \boldsymbol{q}_{\text{sep}} \times (\boldsymbol{v} \times \boldsymbol{B})$
Eddy Currents	0	$\boldsymbol{L} = ([M](\boldsymbol{\omega} \times \boldsymbol{B})) \times \boldsymbol{B}$

The zonal and tesseral harmonics of Earth's gravity are used up to fourth order. The torque is given by the gravity gradient. Point mass gravity is used for lunar and solar gravity.

2.1.3.4.1 *Solar Radiation Pressure*

The magnitude of the SRP force is determined by the solar flux and the illuminated area. The direction is governed by the amount of light that is absorbed and reflected specularly and diffusely (ASD). The SRP force is given by Reference 38:

$$\boldsymbol{F} = p_{\text{SRP}} A \cos(\theta) \left[\rho_A \hat{\boldsymbol{s}} + 2\rho_s \cos(\theta)\hat{\boldsymbol{n}} + \rho_d(\hat{\boldsymbol{s}} + \frac{2}{3}\hat{\boldsymbol{n}}) \right] \tag{2.91}$$

Where θ is the angle between the sun-pointing line and the face normal, $\hat{s}$ is the sun-pointing vector, $\hat{n}$ is normal to the plane, and $\rho_A, \rho_S,$ and ρ_D are the absorptive, specular, and diffuse coefficients, respectively, which must sum to unity. In this analysis, $\rho_A = 0.5$, $\rho_S = 0.2$, and $\rho_D = 0.3$.

2.1.3.4.2 *Magnetic Field Models*

Both the Lorentz force and torque as well as the eddy torque depend on the strength and direction of the magnetic field. There are many approximations for Earth's magnetic field. The first, and simplest is the dipole approximation, next is the IGRF model, and the third is the Tsyangenko model which merges the IGRF with the solar wind.[39] The tilted dipole model is the lowest order version of the IGRF model, which is an expansion much like Earth's spherical gravity. There have been many versions and updates to the Tsyganenko model, but in this analysis the 2001 version is used with GEOPACK 2008[1] for coordinate transforms.

Since the magnetic field is position dependent, the model is run at each timestep. The time is assumed to be January 1, 2000, midnight, for all runs. The space weather parameters used are shown in Tab. 2.10, and are representative values that are used by the Community Coordinated Modeling Center (CCMC) on their single-run website[2]

This produces a magnetic field model that accounts for the solar wind and Earth's geodynamo. As shown in Fig. 2.30, the field is not well-modeled by a tilted dipole alone or the IGRF model. The positions where B is computed are taken from a geostationary orbit, and the magnetic field is shown in the units of 0.1 nT, so the magnitude is near 100 nT (10 units on the axis scale) for all models. The Tsyganenko model is very different from the other two, which makes sense since the

---

[1] http://ccmc.gsfc.nasa.gov/modelweb/magnetos/tsygan.html
[2] http://ccmc.gsfc.nasa.gov/requests/instant/tsyganenko.php

Table 2.10: *Space weather parameters used for Tsyganenko model*

Parameter	Value
Solar Wind Dynamic Pressure	4 nPa
Solar Wind Velocity	400 km/s
IMF B_y	6 nT
IMF B_z	-5 nT
DST	-30 nT
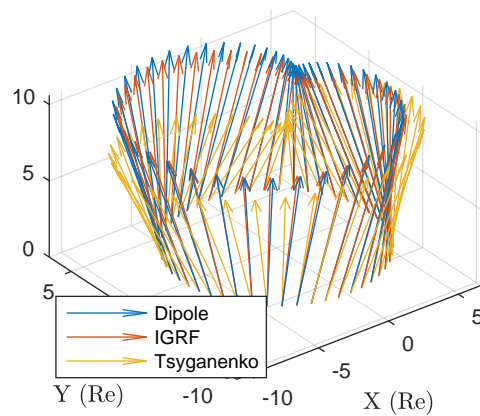
Figure 2.30: *ECI Magnetic field used in this study, Z axis is arbitrary*

tilted dipole is an approximation of the IGRF model and neither take the solar wind into account. The main differences between the IGRF and Tsygnaenko models is that Tsyganenko predicts a lower magnitude and more declination.

2.1.3.4.3 Electric Field Models

The magnetospheric convection electric field also contributes to the electric perturbations. The work uses the Volland-Stern[40,41] model as presented in Reference [42] which gives the voltage of a point in space as:

$$V = -bL^{\gamma} \sin(\phi) \tag{2.92}$$

Where b is a constant, γ is a constant, and $L = \frac{r/Re}{\sin^2(\theta)}$ is the magnetic L shell and ϕ is the magnetic local time referred to noon rather than midnight. The angle θ is the magnetic colatitude, which is measured downwards from the magnetic north pole. In this work $\gamma = 2$, and $b = 45 \, \text{V}/(1 - 0.159K_P + 0.0093 * K_P^2)^3$ is the overall strength as a function of K_P index.[43] To find the colatitude, first transform into the geomagnetic frame[44] which has it's 3rd axis aligned with Earth's north magnetic pole, then take the inverse cosine of $r(3)/||r||$. To find ϕ, project the satellite and sun position into the geomagnetic $x - y$ plane and find the angle with respect the the x axis for both and subtract them to find ϕ.

To find the E field, take the gradient in spherical coordinates $\boldsymbol{E} = -\nabla V$:

$$\boldsymbol{E} = -\nabla V = -\frac{\partial V}{\partial r}\hat{\boldsymbol{r}} - \frac{1}{r}\frac{\partial V}{\partial \theta}\hat{\boldsymbol{\theta}} - \frac{1}{r\sin(\theta)}\frac{\partial V}{\partial \phi}\hat{\boldsymbol{\phi}} \tag{2.93}$$

$$= \frac{V}{r}\left(-\gamma\hat{\boldsymbol{r}} + 2\gamma\cot(\theta)\hat{\boldsymbol{\theta}} - \csc(\theta)\cot(\phi)\hat{\boldsymbol{\phi}} \right) \tag{2.94}$$

Where $\hat{\boldsymbol{r}}$ points outward, $\hat{\boldsymbol{\theta}}$ points southward (magnetically, not geographically), and $\hat{\boldsymbol{\phi}} = \hat{\boldsymbol{r}} \times \hat{\boldsymbol{\theta}}$.

This potential and the electric field are shown in GSM coordinates below in Fig. 2.31(a) for $K_P = 3$. In the figure, the length of the arrow represents the field strength with 1 axis unit representing 2 mV/m. The field is points from dawn to dusk as expected. At this low K_P level the average field strength is 0.434 mV/m, but if K_P increases to 8 it grows to 2.87 mV/m. Figure 2.31(b) shows both the Lorentz field ($\boldsymbol{v} \times \boldsymbol{B}$) and the convection E field in the ECI $x - y$ plane for a geosynchronous orbit inclined to $16°$. The sun is nearly directly below in this figure.

The first thing to notice is that the average magnitude of the E field for this orbit is more than 10 times stronger than the Lorentz field even at $K_P = 3$ (0.431 mV/m vs 0.036 mV/m), at $K_P = 8$ the difference is even greater since the average E field strength grows to 2.85 mV/m. In all prior work by References [25], [26], [27] and [1], the convection E field has been completely ignored in favor of the B field, but it is actually the stronger of the two. In different orbits, specifically one in which there is greater ECEF velocity and is closer to Earth, the $\boldsymbol{v} \times \boldsymbol{B}$ field is stronger.

2.1.3.4.4 Electrostatic Force and Torque

2.1.3.4.4.1 General Development

The effective E-field is $\boldsymbol{A} = \boldsymbol{E} + \boldsymbol{v} \times \boldsymbol{B}$ where $\boldsymbol{v}$ is the velocity relative to the magnetic field. The differential force on a differential charge moving through this field is:[18]

$$\mathrm{d}\boldsymbol{F} = \mathrm{d}q\boldsymbol{A} \tag{2.95}$$
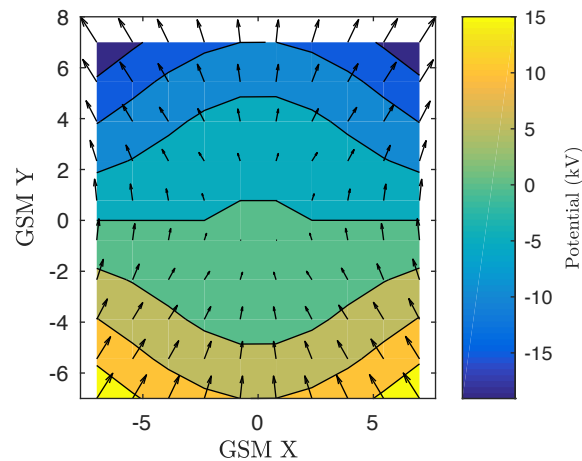
(a) Convection E field in GSM
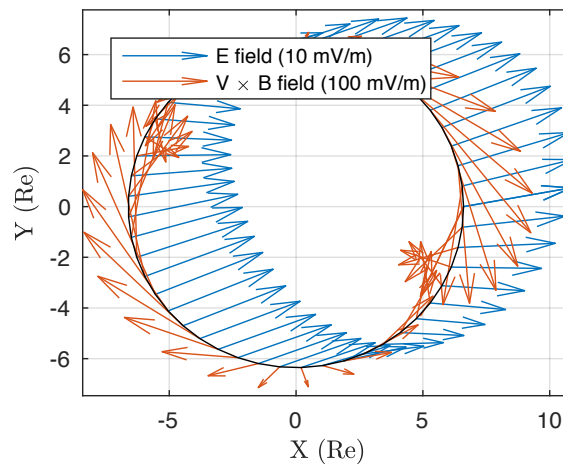
(b) E and V × B field for inclined GEO orbit

Figure 2.31: *Convection E field and Lorentz field comparison for $K_P = 3$*

The torque about the center of mass on a body is defined as $\int_B \boldsymbol{r} \times \mathrm{d}\boldsymbol{F}$, where $\boldsymbol{r}$ points from the center of mass to the volume element. Using the differential force to find the net force and torque on a body gives:

$$\boldsymbol{F} = \int_B \boldsymbol{A} \, \mathrm{d}q \tag{2.96}$$

$$\boldsymbol{L} = \int_B \boldsymbol{r} \times \boldsymbol{A} \, \mathrm{d}q \tag{2.97}$$

If a body is rotating, the velocity relative to the magnetic field will vary over the body and $\boldsymbol{A}$ will be dependent on the position. Assuming an orbit inclined at 16°, the relative velocity at GEO is ~1 km/s. If the body has a radius of 1 meter, and is rotating at 1 degree per second, the relative velocity from rotation is 10^{-5} times smaller than that from the orbit. In this analysis it is neglected and v is simply the translational orbital velocity.

Define the charge separation vector $\boldsymbol{q}$ and the total charge Q below to simplify the force and torque:

$$Q = \int_B \mathrm{d}q \qquad \text{and} \qquad \boldsymbol{q} = \int_B \boldsymbol{r} \mathrm{d}q \tag{2.98}$$

Using the definitions in Eq. (2.98) in the integrals in Eq. (2.96) and (2.97) gives the following results for force and torque:

$$\boldsymbol{F} = \boldsymbol{A}\,\boldsymbol{Q} \qquad \boldsymbol{L} = -\boldsymbol{A} \times \boldsymbol{q} \tag{2.99}$$

2.1.3.4.4.2 Susceptibilities of AFM Parameters

If the new variables Q and $\boldsymbol{q}$ were known at all times, Eq. (2.99) would be enough to predict force and torque, however, the charge distribution changes as the object rotates and changes voltage. This subsection quickly goes over how to predict the parameters Q and $\boldsymbol{q}$ using the plate voltages; a full explanation is given in Reference 17.

Using an elastance-based formulation, the voltage at every node $\boldsymbol{V}$ is given by

$$\boldsymbol{V} = [S]\boldsymbol{Q} \tag{2.100}$$

Where $[S]$ is the elastance matrix, and $\boldsymbol{Q}$ is the charge on each node. There are many ways to make $[S]$, including the Method of Moments (MoM)[13] as well as the Surface Multi-Sphere Method (SMSM).[2] In this work MoM is used, which gives the elements of $[S]$ for two parallel plates perpendicular to the z axis to be:

$$S_{i,j} = \int_{-\Delta y/2}^{\Delta y/2} \int_{-\Delta x/2}^{\Delta x/2} \frac{dx'\,dy'}{\sqrt{(x_c + x')^2 + (y_c + y')^2 + z_c^2}} \tag{2.101}$$

where x_c, y_c are the center-to-center x and y displacements for the two area elements i and j, and z_c is the displacement in the z direction. If $i = j$, x_c and y_c will both be zero. To perform this integration, use the u substitutions $u = x_c + x$, and $v = y_c + y'$:

$$S_{i,j} = \int_{-\Delta y/2 + y_c}^{\Delta y/2 + y_c} \int_{-\Delta x/2 + x_c}^{\Delta x/2 + x_c} \frac{\mathrm{d}u\,\mathrm{d}v}{\sqrt{u^2 + v^2 + z_c^2}} \tag{2.102}$$

Denote the double anti-derivative of this function by s, the elastance entry can be formed from the values of s on the four endpoints of $\mathrm{d}A$:

$$S_{i,j} = s(u_+, v_+) + s(u_-, v_-) - s(u_+, v_-) - s(u_-, v_+) \tag{2.103}$$

Where the $\pm$ subscripts determine the upper or lower limit of that variable. The double anti-derivative s is given below:

$$s(u,v) = \int\int \frac{\mathrm{d}u\,\mathrm{d}v}{\sqrt{u^2 + v^2 + z_c^2}} \tag{2.104}$$

$$= v \log(\sqrt{u^2 + v^2 + z^2} + u) \tag{2.105}$$

$$+ u \log(\sqrt{u^2 + v^2 + z^2} + v)$$

$$- z \tan^{-1}\left(\frac{uv}{z\sqrt{u^2 + v^2 + z^2}}\right) \tag{2.106}$$

$$+ z_c \tan^{-1}\left(\frac{v}{z}\right) - v \tag{2.107}$$

Where $\log()$ is the natural logarithm (base e). Once $[S]$ is known, the charge on each node can be found by solving the linear system. A process for predicting the total charge Q and the dipole $\boldsymbol{q}$ on two nearby conductors is introduced in Reference 17, however that work assumes the distance

between the conductors is larger than the conductors themselves. Thus modifications must be made for this case where the plates are 50 cm in length, and only 160 μm apart. To derive the capacitance matrix for two plates, look at the system in block form:

$$\begin{bmatrix} \boldsymbol{Q}_1 \\ \boldsymbol{Q}_2 \end{bmatrix} = \begin{bmatrix} [C_{S_1}] & [C_M] \\ [C_M^T] & [C_{S_2}] \end{bmatrix} \begin{bmatrix} \boldsymbol{V}_1 \\ \boldsymbol{V}_2 \end{bmatrix} \tag{2.108}$$

since both plates are conductors, the voltage is constant across both of them: $\boldsymbol{V}_1 = V_1 \mathcal{O}(n_1, 1)$ where n_1 is the number of elements used to model plate 1 and $\mathcal{O}(a, b)$ is a matrix consisting only of ones of size $[a, b]$. The total charges on each plate are given by $Q_1 = \sum_i^{n_1} \boldsymbol{Q}_1(i) = \mathcal{O}(1, n_1) \boldsymbol{Q}_1$, thus:

$$\begin{aligned} Q_1 &= \mathcal{O}(1, n_1)[C_{S_1}]\mathcal{O}(n_1, 1)V_1 + \mathcal{O}(1, n_2)[C_M]\mathcal{O}(n_1, 1)V_2 \\ &= C_{S_1} V_1 + C_M V_2 \end{aligned} \tag{2.109}$$

$$\begin{aligned} Q_2 &= \mathcal{O}(1, n_2)[C_M]\mathcal{O}(n_2, 1)V_1 + \mathcal{O}(1, n_1)[C_{S_2}]\mathcal{O}(n_2, 1)V_2 \\ &= C_M V_1 + C_{S_2} V_2 \end{aligned} \tag{2.110}$$

where the model for plate 2 contains n_2 elements. This shows that the elements of the capacitance matrix for two bodies are simply the sum of the elements of the blocks in the large capacitance matrix for every node. Because the two plates are exactly alike except for their relative positions, and because $[S]$ and $[C]$ are symmetric, $C_{S_1} = C_{S_2} = C_S$ and the mutual term C_M is the same. To find the susceptibilities of the dipoles, denote the positions of every node by

$$[R] = \begin{bmatrix} x_1 & x_2 & \dots & x_N \\ y_1 & y_2 & \dots & y_N \\ z_1 & z_2 & \dots & z_N \end{bmatrix} \tag{2.111}$$

for both plates R_1 and R_2. The dipole is given by

$$\boldsymbol{q} = \int_B \boldsymbol{r} \mathrm{d}q = \sum_{i=1}^N \boldsymbol{r}_i Q_i = [R]\boldsymbol{Q} \tag{2.112}$$

for a continuous charge and matrix formulation. Now combine with the form for $\boldsymbol{Q}$ from earlier:

$$\begin{aligned} \boldsymbol{q}_1 &= \boldsymbol{\chi}_{1,1}V_1 + \boldsymbol{\chi}_{1,2}V_2 \\ \boldsymbol{q}_2 &= \boldsymbol{\chi}_{2,1}V_1 + \boldsymbol{\chi}_{2,2}V_2 \end{aligned} \tag{2.113}$$

Where the χ parameters are given by:

$$\boldsymbol{\chi}_{1,1} = [R_1][C_{S_1}]\mathcal{O}(n_1, 1) \quad \boldsymbol{\chi}_{1,2} = [R_1][C_M]\mathcal{O}(n_1, 1) \tag{2.114}$$

$$\boldsymbol{\chi}_{1,2} = [R_2][C_M]\mathcal{O}(n_2, 1) \quad \boldsymbol{\chi}_{2,2} = [R_2][C_{S_2}]\mathcal{O}(n_2, 1) \tag{2.115}$$

For the specific case of two 50 cm plates separated by a 160 μm space, both with their centers of mass displaced by [-2.5, -3.33, 0] cm, the electrostatic parameters are given in Table 2.11:

Since the two plates are held together, only the total dipole $\boldsymbol{q} = \boldsymbol{q}_1 + \boldsymbol{q}_2$ and total charge $Q = Q_1 + Q_2$ need to be considered. Finally, the equations for $\boldsymbol{q}$ and Q can be combined with Eq. 2.99 to yield the Lorentz force and torque from the voltages only:

$$\begin{aligned} \boldsymbol{F} &= (C_S + C_M)(V_1 + V_2)\boldsymbol{A} \\ \boldsymbol{L} &= \big((\boldsymbol{\chi}_{1,1} + \boldsymbol{\chi}_{2,1})V_1 + (\boldsymbol{\chi}_{1,2} + \boldsymbol{\chi}_{2,2})V_2\big) \times \boldsymbol{A} \end{aligned} \tag{2.116}$$

Table 2.11: *AFM parameters for predicting Lorentz force and torque*

Parameter	Value
C_S	20.774 nF
C_M	-20.762 nF
$\chi_{1,1}$	[3.116, 0.692, 0.002] nFm
$\chi_{2,2}$	[3.116, 0.692, -0.002] nFm
$\chi_{1,2}$	[-3.114, -0.692, -0.002] nFm
$\chi_{2,1}$	[-3.114, -0.692, 0.002] nFm

2.1.3.4.5 Eddy Torques

Eddy current torque is included as well. When a conductor spins in a magnetic field, the mobile electrons move in loops because of induction. No net force is felt because the current path is closed, but an eddy current torque is felt.[45] recently developed a general method for calculating this torque through

$$\boldsymbol{L} = ([M](\boldsymbol{\omega} \times \boldsymbol{B})) \times \boldsymbol{B} \tag{2.117}$$

where $[M]$ is the magnetic tensor. For a flat plate, the matrix $[M]$ is given by

$$[M] = C_T \frac{\sigma e}{4} \boldsymbol{n} \boldsymbol{n}^T \tag{2.118}$$

where σ is the conductivity, C_T is a constant dependent on shape and size, and $\boldsymbol{n}$ is a unit vector normal to the plane. For a rectangle with length l greater than width w, C_T is found using St. Venant beam theory:

$$C_T \approx \frac{lw^3}{3(1 + 1.38(\frac{w^2}{l^2})^{1.6})} \tag{2.119}$$

in the cases considered, the normal axis of the plate is $\hat{z}$ which makes the torque equal to

$$\boldsymbol{L} = ([M](\boldsymbol{\omega} \times \boldsymbol{B})) \times \boldsymbol{B} = C_T \frac{\sigma e}{4}(\omega_1 B_2 - \omega_2 B_1) \begin{bmatrix} B_2 \\ B_1 \\ 0 \end{bmatrix} \tag{2.120}$$

For this application, $[M]$ is found using the length and width for one plate, and then doubled since there are two plates.

It is interesting to note that if the plate is spinning about its axis of maximum inertia, ω_3 will be large and ω_1 and ω_2 will be small or zero. The eddy torque will also be small, and the object's spin will be relatively unaffected. If the object is tumbling, only the spin rates about the body 1 and 2 axes are removed and it will eventually fall into a stable spin about its axis of major inertia.

2.1.3.5 Propagation Model Results

Now that all the forces and torques are detailed, the orbit of a HAMR object can be propagated. Once again the object is a 50 cm square piece of MLI with an area to mass ratio of 40.16 m^2/kg. This object is put in an initial orbit with $a = 42,164$ km, $e = 0.0001, i = 16°, \Omega = 0°, \omega = 242.3213°$, and $\nu = 85.05°$. The true anomaly ν is chosen so that the propagation begins at a local time of 4 hours, which subjects the plate to the most dramatic charging. The initial angular rates

are set to zero, and its initial attitude is aligned with the ECI frame ($\boldsymbol{\sigma} = [0, 0, 0]^T$) where $\boldsymbol{\sigma}$ is a Modified Rodriguez Parameter (MRP) to describe the attitude.[19] The orbit is propagated for 24 hours with a 3 second time step using a RK4 integrator, and the resulting altitude departure and longitude are shown in Fig. 2.32
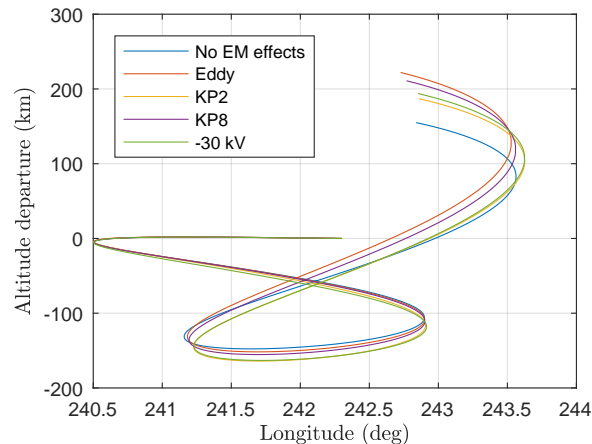

Figure 2.32: *Latitude and altitude departure caused by neglecting perturbations with one initial attitude*

In an unperturbed orbit, all the tracks would end in the same place as they began. However, they all are a few hundred kilometers higher in altitude, and have traversed over more than three degrees of longitude. For reference, the typical longitude spacing between satellites in GEO is $\sim 0.5°$. At the end of the propagation all 5 models predict different final positions. Using the model which only includes gravitational effects and SRP as a reference, including eddy torques gives a final position 109.48 km away. Including just electrostatics at $K_P = 2-$ and $K_P = 8$ gives final position differences of 35.98 and 77.32 km, respectively. Including just electrostatics with a worst case constant voltage of -30 kV gives a final position difference yields a final position difference of 40.23 km. These final positions are small numbers when compared to the orbit radius, but correspond to a few tenths of a degree which matters for telescope pointing.

Using these differences in final positions, it would seem that including eddy torques is the most important, since it leads to the largest position difference. Next would be electrostatics at $K_P = 8$, then a constant voltage of -30 kV, then $K_P = 2$. This is quite surprising since the electric disturbances are strongest at -30 kV, not at $K_P = 8$. To further investigate which perturbations cause the largest differences in position, the same propagation will be repeated, only changing the initial attitude to $\boldsymbol{\sigma} = [0.2, 0, 0]^T$. Again the altitude departure from the initial attitude and the longitude are shown in Fig. 2.33.

Here the object again follows a curving "figure 8" path, and changes altitude by ~ 400 km and longitude by $\sim 3°$. However, the orbits are drastically different from those computed those computed with the first attitude - for instance, the model that ignores all electromagnetic perturbations predicts a final altitude departure of more than 200 km with the first attitude, but less than 200 km with the second attitude. Additionally, the ordering of the relative impacts of the different perturbations is different. Choosing the model which ignores all electromagnetic effects as the reference, including eddy torques leads to a 14.58 km difference after 24 hours, electrostatics at $K_P = 2-$ and 8 lead to differences of 130.38 and 33.85 km, and a constant voltage of -30 kV leads to a final position difference of 62.26 km. While eddy current torque was the most significant at the first attitude, it is the *least* at this attitude. $K_P = 2-$ and $K_P = 8$ switch places, and the constant -30

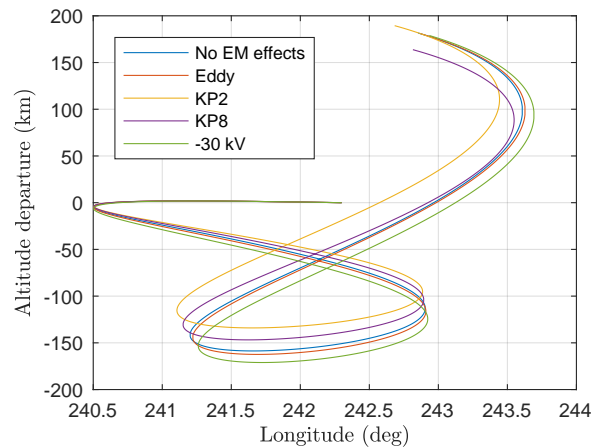kV case is now less significant than electrostatics at $K_P = 2-$.

Figure 2.33: *Latitude and altitude departure caused by neglecting perturbations at a different initial attitude*

These simulations results illustrate that the initial attitude *and* the propagation model used both have a strong influence on the orbit. Because even the relative ordering of how significant different electromagnetic perturbations are gets re-shuffled, it would appear that the initial attitude and the propagation model are coupled. This is not completely surprising, since the significant part of the electromagnetic perturbations is the torque, which changes the attitude, which "steers" SRP.[27] Either a small torque (such as from electromagnetics) integrated over time, or a different initial attitude will result in a different attitude, which changes SRP, which changes the orbit. It is prudent to remember that this behavior is due in most part to the strongly attitude-dependent cross sectional area of this flat plate. A sphere with the same area to mass ratio is nowhere near as sensitive.[26]

2.1.3.6 Statistical Analysis

The earlier section showed that the relative effect of different electromagnetic perturbations was not consistent for two different initial attitudes. This section looks at hundreds of initial attitudes to find which perturbations are the most significant. Additionally, the effect of including different electromagnetic perturbations is compared to initial uncertainty in attitude. To do this, the same 50 cm plate is propagated either with an initial attitude perturbation, or including electromagnetic perturbations and then compared to a plate that had neither an initial attitude perturbation or electromagnetic perturbations. This is shown schematically in Fig. 2.34.

For all cases, a plate is put into orbit with the initial orbit elements of $a = 42,164$ km, $e = 0.0001, i = 16°, \Omega = 0°, \omega = 242.3213°$, and $\nu = 85.05°$. The true anomaly ν is chosen so that the propagation begins at a local time of 4 hours, which subjects the plate to the most dramatic charging. A random initial attitude σ_i is generated from three uniformly distributed Euler angles. A plate with this attitude is propagated neglecting all electromagnetic effects for a period of time Δt and its final position r_{Ref} is recorded. Next, a perturbation or initial attitude difference is added. For the attitude difference, a rotation of magnitude θ_j about a randomly selected axis $\hat{u}$ where $\theta = [0.0001°, 0.001°, 0.01°, 0.1°, 1°]$ using the principle rotation vector $\gamma = \theta_j \hat{u}$ and the final position r_{Rotation} after Δt is recorded. For the perturbations, the plate is not rotated but either eddy torques, electrostatics at $K_P = 2-, K_P = 8$, or a worst-case constant voltage of -30 kV are included in the
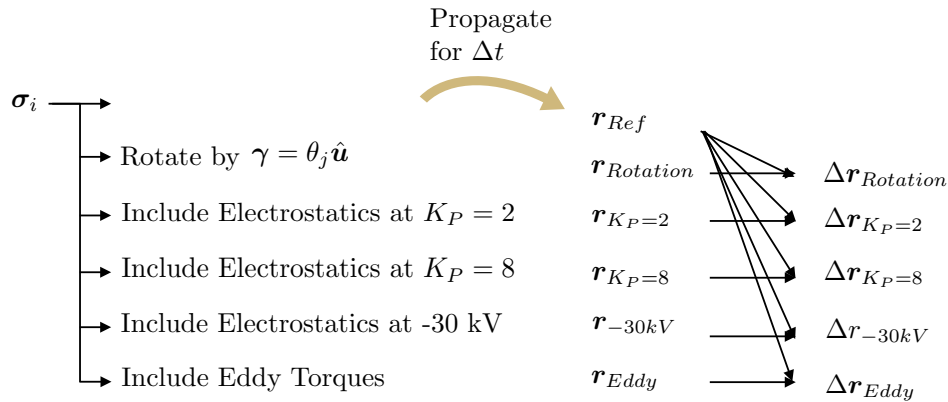
Figure 2.34: *Scheme for investigating relative effect of electromagnetic disturbances with random-ized initial attitude*

propagation and the final positions ($r_{K_P=2}, r_{K_P=8}, r_{-30kV}, r_{Eddy}$) are recorded. The electrostatic cases are run without eddy torques included. Finally the difference in final positions between the reference r_{Ref} and the cases that include electromagnetic perturbations or have a different initial attitude are computed ($\Delta r_{Rotation}, \Delta r_{K_P=2}, \Delta r_{K_P=8}, \Delta r_{Eddy}$). This process is repeated 500 times varying the initial attitude σ_i each time recording the Δr every 15 minutes for 3 hours in a master text file. The 10 cases, run for 3 hours of simulation time, for 500 different initial attitudes gives 15,000 hours of propagation time. The results of this propagation are shown in Fig. 2.35.

The statistics for the effect of an initial attitude difference or including an electromagnetic per-turbation are shown using violin plots. Violin plots are a way of looking at multiple histograms at once - the width of the bar represents how many counts are observed in the bin given by the position on the y axis. Violin plots can be thought of as a collection of histograms all rotated by 90°. The different ticks on the x axis represent different cases. For example, consider the 0.0001° case after 3 hours of propagation shown in Fig. 2.35(c). The position difference from this initial attitude change is either less than 1 cm, or in the hundreds of meters. Simply reporting the mean or median (shown in red and green, respectively) would lead one to believe that most of the initial attitudes lead to final position differences of ~1 m, when in reality almost none of them are.

At the 1 hour mark (Fig. 2.35(a)), including electrostatics with $K_P = 2-$ only causes position differences greater than a meter for very few initial attitudes, furthermore, it is *less* significant than a 0.0001° uncertainty in initial attitude, which is nearly impossible to get from a ground observation for a non-cooperative object. If $K_P = 8$, a significant fraction of the initial attitudes lead to position difference of dozens of meters after only an hour, and including or neglecting electrostatics is equivalent to a little less than 0.001° uncertainty in initial attitude. If the worst case is observed and both sides of the plate are charged to -30 kV, almost all the initial attitudes lead to position differences greater than a meter after only an hour with a few exceeding 100 m. This is more significant than 1° of attitude uncertainty. Including eddy torques also causes a large spread and is comparable to 1° of uncertainty.

Moving to the 2 hour mark of simulated orbit time, the distributions begin to look bi-modal. One population of initial attitudes leads to large position differences greater than 10 meters, while the other leads to much smaller position differences. This may be because some attitudes lead to "runaway" differences while others lead to stable spins about the axis of maximum inertia which are much harder to perturb and change the attitude in a way that affects SRP.[27] It is still the case that electrostatics at $K_P = 2-$ are less significant than 0.0001° of attitude uncertainty, at $K_P = 8$ including electrostatics is roughly equivalent to 0.001° of attitude uncertainty, the worst

(a) After 1 hour

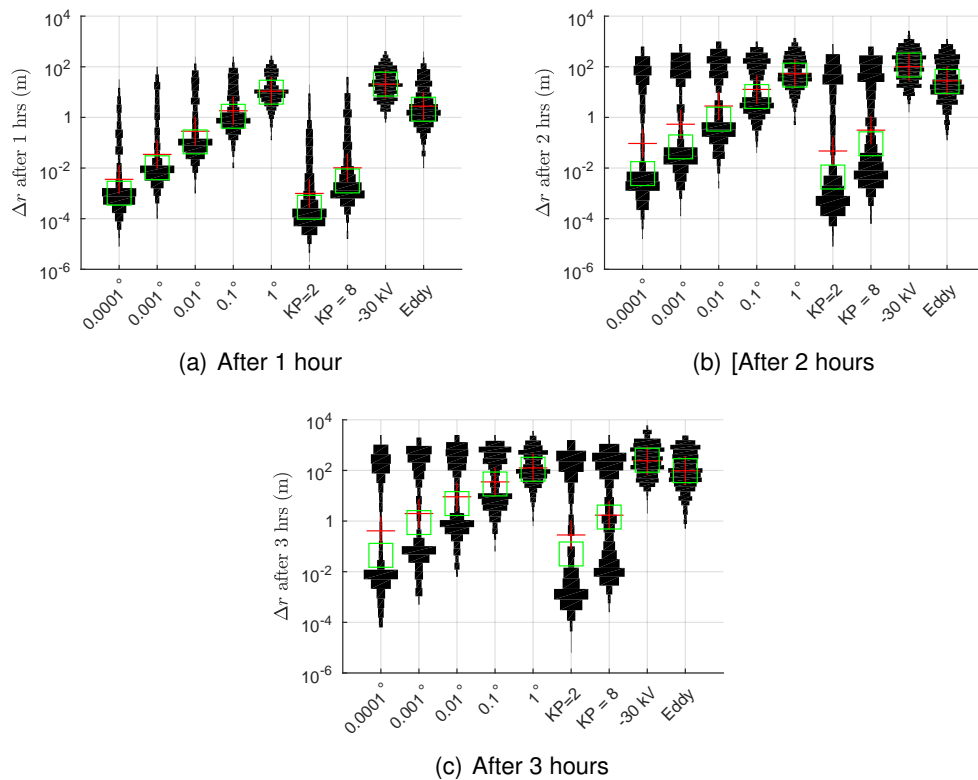(b) [After 2 hours

(c) After 3 hours

Figure 2.35: *Position differences caused by including electromagnetic perturbations or initial attitude uncertainty*

case is more significant than $1°$ of uncertainty, and that including eddy torques is similar to $1°$ of uncertainty.

Moving finally to 3 hours of simulated orbit time, now a very significant portion of all initial attitudes with all perturbations lead to position differences of more than 100 meters. The split between the runaway cases and the others is even more dramatic, causing many of the plots to take on a "dog-bone" shape. Surprisingly, including eddy torques, the -30 kV, and the $1°$ rotation nearly always causes at least a 1 meter position change, which removes the lower lobe. It is still the case that electrostatics at $K_P = 2-$ are less significant than $0.0001°$ of attitude uncertainty, at $K_P = 8$ including electrostatics is roughly equivalent to $0.001°$ of attitude uncertainty, the worst case is more significant than $1°$ of uncertainty, and that including eddy torques is similar to $1°$ of uncertainty. The maximum position difference is observed for the worst case -30 kV and is 5.77 km.

It is interesting to look at how the spread from including or neglecting a certain perturbation or attitude uncertainty changes with time. To do this, the 95% upper bound is found for each perturbation/attitude uncertainty at each time. This is done by sorting the Δr, and taking the 475th element since there are 500 entries. This gives an empirical estimate to the 2σ covariance bound that should be associated with the initial attitude uncertainty or the un-modeled perturbations. This covariance bound is plotted in Fig. 2.36 for all the perturbations and the limiting attitude uncertainties of $1°$ and $0.0001°$.

The worst case constant voltage of -30 kV causes the largest covariance, followed by the $1°$ attitude uncertainty, then eddy torques, then $K_P = 8$, then $K_P = 2-$ and the $0.0001°$ attitude uncertainty which are similar. All of the perturbations/attitude uncertainties lead to between 0.5
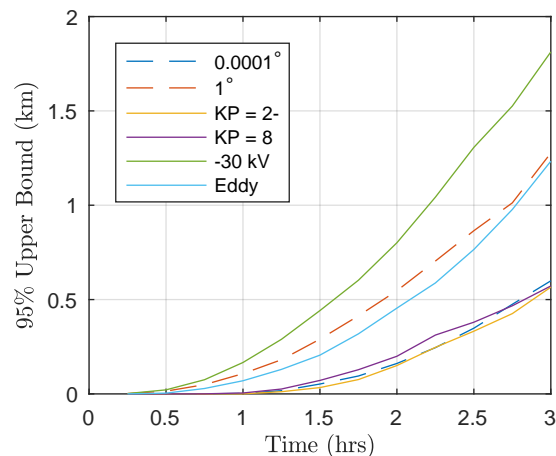
Figure 2.36: *95% covariance bounds for different perturbations and uncertainties*

and 2 km covariance after 3 hours, and seem to be accelerating. In the case of a solar storm at $K_P = 8$, the covariance bounds do not need to be drastically changed from the normal ones associated with attitude uncertainty. However, if the worst case charging is maintained, such as might happen considering deep dielectric charging, the covariance bounds need to be expanded beyond their normal values. Eddy torques, which act no matter what K_P is, always cause large covariances.

2.1.4 Heterogeneous SMSM Modeling

2.1.4.1 Motivation

In the Geosynchronous Earth Orbit (GEO) regime, satellites charge to very high voltages sometimes as dramatic as -19 kV.[46] This charging can cause dangerous arcing as well as small forces and torques on the body due to interactions with earth's magnetic field, which changes the orbits of some uncontrolled lightweight debris objects through the Lorentz force.[25–27,47] If nearby spacecraft use active charging such as electron and ion guns, larger forces and torques are felt between the crafts. This enables novel Coulomb formation flying missions.[48–50] These forces can also be used for touchless re-orbiting of GEO debris to its graveyard orbit in a matter of months using the Electrostatic Tractor (ET).[51] If a spacecraft has a non-symmetric charge distribution, it also experiences torques which can be harnessed for touchless de-spin before servicing or grappling.[21,52,53]

There are many separate challenges to electrostatic actuation such as prescribing the appropriate electron and/or ion beam current and voltage, sensing the voltage, position, and attitude of a passive space object, and designing control laws that perform well for either tugging or de-spinning. In order to design and implement stable and performant control laws in any of the above mission scenarios, accurate and fast methods are needed to predict the force and torque on both spacecraft using only in-situ measurements such as the voltage of each craft, and their relative separation and attitude. Accuracy is important because under or over prediction can seriously harm performance, or lead to a collision.[54] Speed is important because the force and torque must be predicted in real time by the flight computer.

The Multi-Sphere Method (MSM) is developed as a faster-than-realtime method for electrostatic force and torque prediction for conducting satellites.[3] MSM places equipotential spheres in the body of the spacecraft, then forms a simple elastance matrix, and solves for the charge. Once

the charges are found, the force and torque can be found by applying Coulomb's law between every pair of spheres on the two spacecraft. The size and location of the spheres are tuned to match the force and torque predicted by a higher-fidelity truth model. The process of placing and sizing the spheres is optimized in[5] and it is found that using only a few spheres, the force and toque can be predicted within a few percent error even at close distances. This process is further advanced in[55] with the advancement of fitting to the predicted E field rather than the force and torque, which makes the optimization much more robust.

Another addition to the MSM family is Surface MSM (SMSM) which places equal-radius spheres equidistantly along the surface of the spacecraft.[2] The sphere radius is then varied so that the model matches the self capacitance predicted by a higher-fidelity model. This model avoids nearly all of the difficulties with optimization since the sphere locations are prescribed and is more accurate than MSM, but it is much slower to evaluate due to the larger number of spheres.

Although developed independently, SMSM is very close in form to the Boundary Element Method (BEM)[56] and the Method of Moments (MoM). MoM is a general numerical method that can be used to solve a variety of electromagnetic problems.[57] MoM is similar to BEM in that it does not account for charge in the volume of interest, but rather just on the exterior, hence the name of "boundary" element method. MoM is similar to SMSM in that it inverts an elastance matrix to solve for the charge distribution, but it differs in how the elastance matrix is formed. In MSM, the elements are formed from the size and location of the spheres, which are tuned to match some truth file. In MoM, they are derived from first principles. Unlike FEA methods, the size of the element is considered which means that each element of the elastance matrix requires a double integral. This nesting of a model within model adds initial complexity, but means that fewer elements are needed than with FEA, since the MoM elements are "smarter". Recently, the MoM is used to estimate the capacitance of geometrically complex spacecraft and their components in.[58–60] This puts an upper bound on the size of arcs that can occur. This formulation has also been applied to conductors coated with dielectrics as well.[61]

This paper investigates the links from MoM to MSM and SMSM and uses these links to make more rigorous SMSM models and give MSM a stronger foundation. This is done by first deriving the MoM elements of the elastance matrix using a different coordinate system which allows for one of the integrals to be done analytically. Next, MSM models are made from MoM models for both homogeneous and non-homogeneous meshes. Finally, these models are compared in their execution time and accuracy.

2.1.4.2 Method of Moments Formulation

2.1.4.2.1 Review of Method of Moments Formulation

The MoM for electrostatics is based on Gauss' law:

$$V(\boldsymbol{r}) = \int \frac{\mathrm{d}q'}{4\pi\epsilon_0 ||\boldsymbol{r} - \boldsymbol{r}'||} \tag{2.121}$$

where $\boldsymbol{r}$ is the observation point and $\boldsymbol{r}'$ is the source point. The source in question is the infinitesimal charge $\mathrm{d}q$ and the voltage is being observed. If the source region is discretized into area elements A_i the voltage is

$$V(\boldsymbol{r}) = \frac{1}{4\pi\epsilon_0}\left(\int_{A_1}\frac{dA'}{|\boldsymbol{r}-\boldsymbol{r}'|}\sigma_1 + \int_{A_2}\frac{dA'}{|\boldsymbol{r}-\boldsymbol{r}'|}\sigma_2 + \dots\right) \tag{2.122}$$

where σ_i is the surface charge density on the ith area element. Now apply this equation to find the voltage of the centroid of each element to get the following matrix equation:

$$
\begin{bmatrix} V_1 \\ V_2 \\ \vdots \\ V_N \end{bmatrix} = \frac{1}{4\pi\epsilon_0} \begin{bmatrix} \int_{A_1} \frac{dA}{|\boldsymbol{r}_1 - \boldsymbol{r}'|} & \cdots & \int_{A_N} \frac{dA}{|\boldsymbol{r}_1 - \boldsymbol{r}'|} \\ \int_{A_1} \frac{dA}{|\boldsymbol{r}_2 - \boldsymbol{r}'|} & \cdots & \int_{A_N} \frac{dA}{|\boldsymbol{r}_2 - \boldsymbol{r}'|} \\ \vdots & & \vdots \\ \int_{A_1} \frac{dA}{|\boldsymbol{r}_N - \boldsymbol{r}'|} & \cdots & \int_{A_N} \frac{dA}{|\boldsymbol{r}_N - \boldsymbol{r}'|} \end{bmatrix} \begin{bmatrix} \sigma_1 \\ \vdots \\ \sigma_N \end{bmatrix} \tag{2.123}
$$

This large matrix in the center is known as the elastance matrix $[S]$. In order to match prior work in MSM, each element in $[S]$ is divided by the area of that element to give $[S]$ units of Farads^{-1} and put the charge per element $\boldsymbol{Q}$ on the right hand side rather than the surface charge density to give the expression $\boldsymbol{V} = [S]\boldsymbol{Q}$.
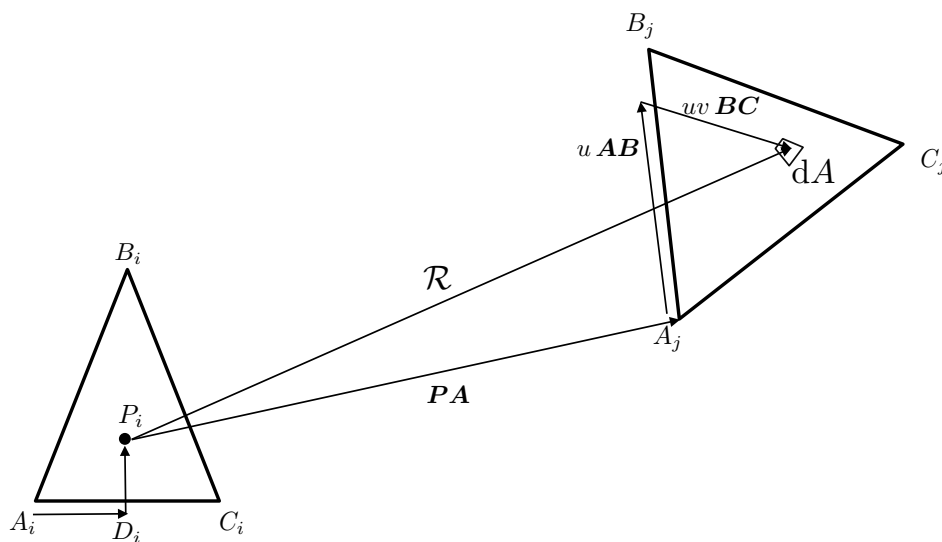
Figure 2.37: *Illustration of triangular coordinate system*

2.1.4.2.2 Implementation with Triangular Elements

Next, chose triangles as the basis area and parameterize the vector $\mathcal{R} = |\boldsymbol{r}_N - \boldsymbol{r}'|$. To simplify $\mathcal{R}$, consider two triangles i and j both formed from the corners $[\boldsymbol{A}, \boldsymbol{B}, \boldsymbol{C}]$ as shown in Fig. 2.37. The vectors of the form $\boldsymbol{XY}$ point from point $\boldsymbol{X}$ to point $\boldsymbol{Y}$. Now it is clear that the separation is given by

$$
\mathcal{R} = \boldsymbol{PA} + u\boldsymbol{AB} + uv\,\boldsymbol{BC} \tag{2.124}
$$

Where $u, v \in [0, 1]$. The u in the uv term keeps the $\boldsymbol{BC}$ vector from going its full length near point $\boldsymbol{A}$; without it, one would integrate a parallelogram rather than a triangle. Since the triangles are not necessarily right, $\boldsymbol{AB}$ and $\boldsymbol{BC}$ are not always right and therefore the set u, v is not orthogonal. The infinitesimal area with this definition for $\mathcal{R}$ is a trapezoid with

$$
\mathrm{d}A = u||\boldsymbol{AB} \times \boldsymbol{BC}||\mathrm{d}u\,\mathrm{d}v \tag{2.125}
$$

The elements of $[S]$ in this basis set are then given by

$$
S_{i,j} = \frac{1}{4\pi\epsilon_0 A_j} \int_A \frac{\mathrm{d}A}{\mathcal{R}} = \frac{1}{4\pi\epsilon_0 A_j} \int_0^1 \int_0^1 \frac{u||\boldsymbol{AB} \times \boldsymbol{BC}||\,\mathrm{d}v\,\mathrm{d}u}{||\boldsymbol{PA} + u\boldsymbol{AB} + uv\boldsymbol{BC}||} \tag{2.126}
$$

The denominator is expanded by dotting it with itself and then taking the square root. The first integral over v is

$$
S_{i,j} = \frac{||\boldsymbol{AB} \times \boldsymbol{BC}||}{4\pi\epsilon_0 bcA_j} \int_0^1 \log\left(bc\sqrt{u^2(ab^2 + 2\boldsymbol{AB}\cdot\boldsymbol{BC} + bc^2)} + u(2\boldsymbol{PA}\cdot\boldsymbol{AB} + 2\boldsymbol{PA}\cdot\boldsymbol{BC}) + pa^2 \right.
$$
$$
\left. - \log(bc\sqrt{ab^2u^2 + pa^2 + 2\boldsymbol{PA}\cdot\boldsymbol{AB}u} + \boldsymbol{AB}\cdot\boldsymbol{BC}u + \boldsymbol{PA}\cdot\boldsymbol{BC}) \right) + \boldsymbol{AB}\cdot\boldsymbol{BC}u + bc^2u
$$
$$
+ \boldsymbol{PA}\cdot\boldsymbol{BC}\,\mathrm{d}u \quad (2.127)
$$

where scalars of the form xy are the magnitude of vector $\boldsymbol{XY}$. An analytic solution to the second integral over u has not been found and so this integral is done numerically using an adaptive quadrature algorithm. When $i = j$, there is a special form for $\boldsymbol{PA}$:

$$
\boldsymbol{PA} = -\frac{2}{3}\boldsymbol{AB} - \frac{1}{3}\boldsymbol{BC} \quad (2.128)
$$

The integral now becomes:

$$
S_{i,i} = \frac{1}{4\pi\epsilon_0 A_i} \int_{A_i} \frac{\mathrm{d}A}{\mathcal{R}} = \frac{1}{4\pi\epsilon_0 A_i} \int_0^1 \int_0^1 \frac{u\,\boldsymbol{AB} \times \boldsymbol{BC}\,\mathrm{d}v\,\mathrm{d}u}{||(u - 2/3)\boldsymbol{AB} + (uv - 1/3)\boldsymbol{BC}||} \quad (2.129)
$$

The magnitude of $\mathcal{R}$ is once again found by taking the square root of the dot product of the vector with itself. The first integral over v is

$$
S(i,i) = \frac{||\boldsymbol{AB} \times \boldsymbol{BC}||}{4\pi\epsilon_0 bcA_i} \int_0^1 \log\left(bc\sqrt{ab^2(2 - 3u)^2 + (3u - 1)(\boldsymbol{AB}\cdot\boldsymbol{BC}(6u - 4) + bc^2(3u - 1))} \right.
$$
$$
+ (3u - 1)bc^2 + \boldsymbol{AB}\cdot\boldsymbol{BC}(3u - 2)bc) - bc^2 + \boldsymbol{AB}\cdot\boldsymbol{BC}(3u - 2
$$
$$
\left. - \log\left(bc\sqrt{ab^2(2 - 3u)^2 - 6\boldsymbol{AB}\cdot\boldsymbol{BC}u + 4\boldsymbol{AB}\cdot\boldsymbol{BC} + bc^2} \right) \right) \quad (2.130)
$$

Once again, this integral is done numerically using the adaptive quadrature algorithm. Although the function is singular when $u = 1/3$, the integral is still completed robustly. An alternative method for dealing with this singularity presented in Reference 59 is to divide the triangle into three smaller triangles with the singularity at their common point, and then use a Duffy transformation to remove the singularity. Once this is done the double integral is computed numerically. In contrast, the method presented here does not avoid the singularity as elegantly, but does one of the integrals analytically. In all subsequent computations, a relative error threshold for the adaptive quadrature integrator is 10^{-4}.

To validate this MoM implementation presented here, the self capacitance of a square plate is computed with increasing resolution. The self capacitance is shown as a function of the number of triangles in the mesh in Fig. 2.38(a). Beginning with a mesh consisting of only two triangles the self capacitance is near 33 pF, and it increases up to 40.26 pF with 722 triangles for the final run. This is very close to the value from other authors using different methods[62] and involves many fewer elements than would be needed in a FEA scheme. The final charge distribution is shown in Fig. 2.38(b). More charge accumulates at the corners of the plate, as expected.

2.1.4.3 E-Field Computation

Once the charges on all the triangles have been found, the E field at an arbitrary point $\boldsymbol{P}$ can be found.

$$
\boldsymbol{E}(\boldsymbol{P}) = \frac{1}{4\pi\epsilon_0}\left(\int_{A_1} \frac{\sigma_1\mathcal{R}}{\mathcal{R}^3}\mathrm{d}A + \int_{A_2} \frac{\sigma_2\mathcal{R}}{\mathcal{R}^3}\mathrm{d}A + ... \right) \quad (2.131)
$$

(a) Self Capacitance as a function of number of triangles used
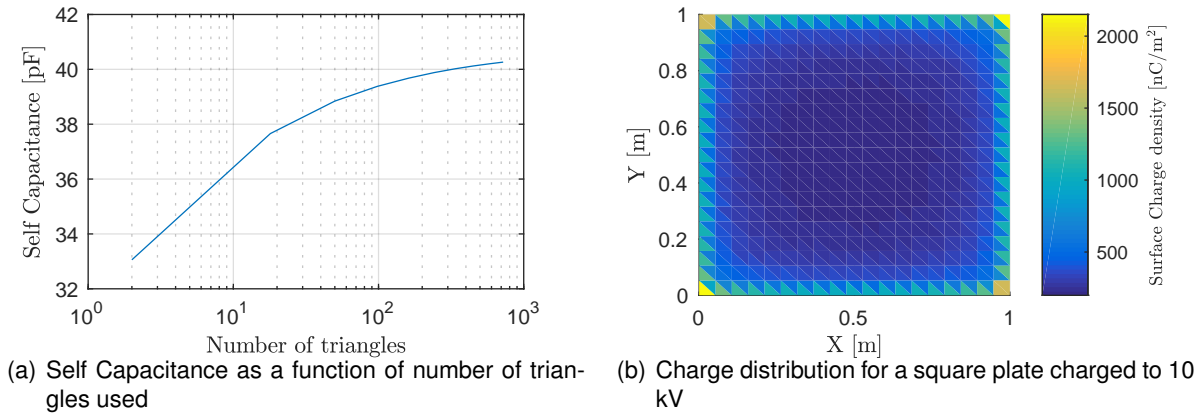

(b) Charge distribution for a square plate charged to 10 kV

Figure 2.38: *Validation of MoM implementation on a square plate*

where $\mathcal{R}$ once again points from the area element to point $\boldsymbol{P}$ and $\mathrm{d}A$ is still $u||\boldsymbol{AB} \times \boldsymbol{BC}||\mathrm{d}u\,\mathrm{d}v$. The E field contribution from each triangle is then:

$$\boldsymbol{E}(\boldsymbol{P}) = \frac{||\boldsymbol{AB} \times \boldsymbol{BC}||Q}{4\pi\epsilon_0 A} \cdot$$
$$\int_0^1 \int_0^1 \frac{u^2\boldsymbol{AB} + u^2v\boldsymbol{BC} + u\boldsymbol{PA}\mathrm{d}u\mathrm{d}v}{(u(ab^2u + 2v(\boldsymbol{AB} \cdot \boldsymbol{BC}u + \boldsymbol{PA} \cdot \boldsymbol{BC}) + bc^2uv^2 + 2\boldsymbol{PA} \cdot \boldsymbol{AB}) + pa^2)^{3/2}} \quad (2.132)$$

where A is the area of that triangle. This is integrated over v analytically to give:

$$\boldsymbol{E}(\boldsymbol{P}) = \frac{-||\boldsymbol{AB} \times \boldsymbol{BC}||Q}{4\pi\epsilon_0 A} \int_0^1 \frac{\mathrm{d}u}{((\boldsymbol{AB} \cdot \boldsymbol{BC}u + \boldsymbol{PA} \cdot \boldsymbol{BC})^2 - bc^2(u(ab^2u + 2\boldsymbol{PA} \cdot \boldsymbol{AB}) + pa^2))}$$
$$\left(\frac{\boldsymbol{BC}\left(u\left(u\left(ab^2 + \boldsymbol{AB} \cdot \boldsymbol{BC}\right) + 2\boldsymbol{PA} \cdot \boldsymbol{AB} + \boldsymbol{PA} \cdot \boldsymbol{BC}\right) + pa^2\right)}{\sqrt{u\left(u\left(ab^2 + 2\boldsymbol{AB} \cdot \boldsymbol{BC} + bc^2\right) + 2(\boldsymbol{PA} \cdot \boldsymbol{AB} + \boldsymbol{PA} \cdot \boldsymbol{BC})\right) + pa^2}} \right.$$
$$- \frac{(\boldsymbol{AB}u + \boldsymbol{PA})\left(u\left(\boldsymbol{AB} \cdot \boldsymbol{BC} + bc^2\right) + \boldsymbol{PA} \cdot \boldsymbol{BC}\right)}{\sqrt{u\left(u\left(ab^2 + 2\boldsymbol{AB} \cdot \boldsymbol{BC} + bc^2\right) + 2(\boldsymbol{PA} \cdot \boldsymbol{AB} + \boldsymbol{PA} \cdot \boldsymbol{BC})\right) + pa^2}}$$
$$\left. + \frac{(\boldsymbol{AB}u + \boldsymbol{PA})(\boldsymbol{AB} \cdot \boldsymbol{BC}u + \boldsymbol{PA} \cdot \boldsymbol{BC}) - \boldsymbol{BC}\left(u\left(ab^2u + 2\boldsymbol{PA} \cdot \boldsymbol{AB}\right) + pa^2\right)}{\sqrt{u\left(ab^2u + 2\boldsymbol{PA} \cdot \boldsymbol{AB}\right) + pa^2}} \right) \quad (2.133)$$

This integral over u is computed numerically because an analytic solution was not found. Keep in mind that this is the E field contribution of a single triangle. To compute the E field due to a full MoM model with many triangles, this expression must be computed for each triangle and summed. To compute the force between two models, the E field due to all triangles in the first model is computed at the centroid of each triangle in the second model and multiplied by the total charge on that triangle.

2.1.4.4 Multi-Sphere Method

The Multi-Sphere Method (MSM) was originally created as a fast way to predict the electrostatic force and torque between conductors.[3] It is very similar to the MoM, but rather than the elements of the elastance matrix being derived from first principles, they are hand-tuned to match force, torque, or E fields predicted by a higher fidelity model.
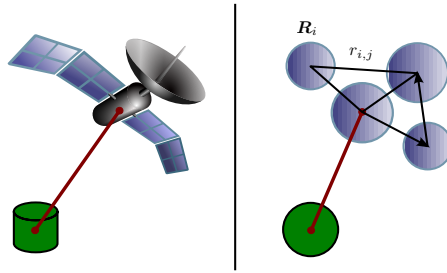
Figure 2.39: *Multi-Sphere Method concept*

As shown in Figure 2.39, MSM approximates a spacecraft as a collection of spheres with variable positions and radii. The voltage on any sphere is a function of both its own charge and the charge of all nearby spheres. If these spheres are far enough away to be approximated as point charges, the voltage is given by:[3]

$$V_i = \frac{1}{4\pi\epsilon_0}\frac{Q_i}{R_i} + \sum_{j=1, j\neq i}^{n}\frac{1}{4\pi\epsilon_0}\frac{Q_j}{r_{i,j}} \tag{2.134}$$

Where q_i and R_i are the charge and radius of the ith sphere, respectively, $r_{i,j}$ is the center-to-center distance between spheres i and j, and ϵ_0 is the permittivity of free space constant. If the voltages of each sphere are given by $\boldsymbol{V} = [V_1, V_2, ...V_n]^{\mathsf{T}}$ and the charges are given by $\boldsymbol{Q} = [Q_1, Q_2, ...Q_n]^{\mathsf{T}}$, the relationship between the two is

$$\boldsymbol{V} = [S]\boldsymbol{Q} \tag{2.135}$$

where $[S]$ is the elastance matrix defined below:

$$[S] = \frac{1}{4\pi\epsilon_0}\begin{bmatrix} 1/R_1 & 1/r_{1,2} & \cdots & 1/r_{1,n} \\ 1/r_{2,1} & 1/R_2 & \cdots & 1/r_{2,n} \\ \vdots & \vdots & \ddots & \vdots \\ 1/r_{n,1} & 1/r_{n,2} & \cdots & 1/R_n \end{bmatrix}\begin{bmatrix} Q_1 \\ Q_2 \\ \vdots \\ Q_n \end{bmatrix} \tag{2.136}$$

If the voltage is known, the linear system can be solved for the charges $\boldsymbol{Q}$. In either MSM or MoM, if there are two charged conducting bodies this matrix takes on a block form:

$$\begin{bmatrix} \boldsymbol{V}_1 \\ \boldsymbol{V}_2 \end{bmatrix} = \begin{bmatrix} S_1 & S_M \\ S_M^T & S_2 \end{bmatrix}\begin{bmatrix} \boldsymbol{Q}_1 \\ \boldsymbol{Q}_2 \end{bmatrix} \tag{2.137}$$

where S_M and S_M^T are the mutual blocks of the elastance matrix, and S_1 and S_2 are the diagonal blocks. To find the force and torque on either body apply the Coulomb law between every pair of spheres:

$$\boldsymbol{F}_1 = \frac{1}{4\pi\epsilon_0}\sum_{i=1}^{n}\boldsymbol{Q}_{1_i}\sum_{j=1}^{m}\frac{\boldsymbol{Q}_{2_j}\boldsymbol{r}_{j,i}}{r_{j,i}^3} \tag{2.138}$$

$$\boldsymbol{L}_1 = \frac{1}{4\pi\epsilon_0}\sum_{i=1}^{n}\boldsymbol{Q}_{1_i}\sum_{j=1}^{m}\boldsymbol{r}_i \times \frac{\boldsymbol{Q}_{2_j}\boldsymbol{r}_{i,j}}{r_{i,j}^3} \tag{2.139}$$

where $\boldsymbol{r}_{j,i}$ is a vector that points from sphere j in body 2 to sphere i in body 1 and $\boldsymbol{r}_i$ points from the center of mass of body 1 to sphere i.

MSM and MoM both place elements on the surface of the conductor and then use an elastance matrix to solve for the charge distribution. They differ in how they make the elements of the elastance matrix. With MoM, this is done using a double integral of one over the distance from the observation point to a source point in the other element. In MSM, it is one over the distance between the centroids. This is shown schematically in Fig. 2.40.
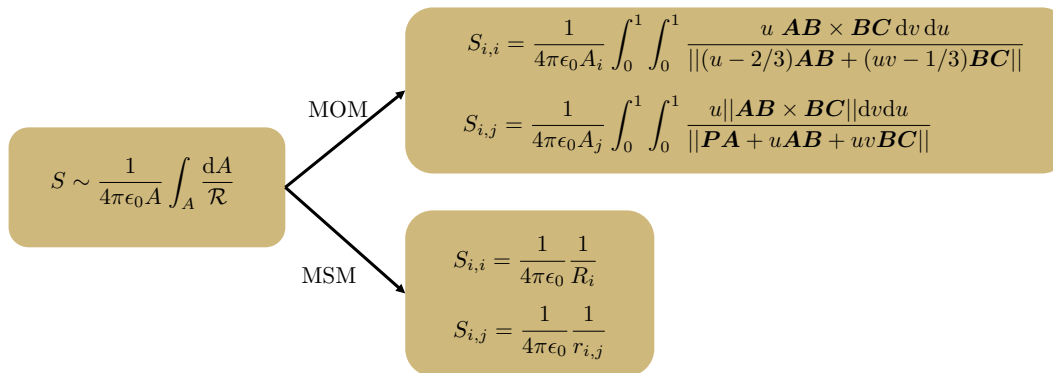

$$S \sim \frac{1}{4\pi\epsilon_0 A}\int_A \frac{\mathrm{d}A}{\mathcal{R}}$$

MOM

$$S_{i,i} = \frac{1}{4\pi\epsilon_0 A_i}\int_0^1\int_0^1 \frac{u\,\boldsymbol{AB}\times\boldsymbol{BC}\,\mathrm{d}v\,\mathrm{d}u}{||(u-2/3)\boldsymbol{AB}+(uv-1/3)\boldsymbol{BC}||}$$

$$S_{i,j} = \frac{1}{4\pi\epsilon_0 A_j}\int_0^1\int_0^1 \frac{u||\boldsymbol{AB}\times\boldsymbol{BC}||\mathrm{d}v\mathrm{d}u}{||\boldsymbol{PA}+u\boldsymbol{AB}+uv\boldsymbol{BC}||}$$

MSM

$$S_{i,i} = \frac{1}{4\pi\epsilon_0}\frac{1}{R_i}$$

$$S_{i,j} = \frac{1}{4\pi\epsilon_0}\frac{1}{r_{i,j}}$$

Figure 2.40: *Differences between MoM and MSM methods*

MSM approximates the integrals of $1/\mathcal{R}$ as either one over the radius of that sphere, or one over the distance to the other sphere. The center to center distance is similar to the vector $\boldsymbol{PA}$, which is the largest term in the denominator. The radius of the sphere is similar to the effective radius of the triangular element. Once again, the MSM spheres are positioned and sized to match force, torque, or E fields computed from a higher fidelity model, so the elements of the elastance matrix have limited physical and geometric significance.

To better understand how the MoM triangular element compares to the MSM sphere, consider a constant area isosceles MoM triangle shown in Fig. 2.41(a). When θ is small the triangle is very tall and skinny, when $\theta = 60°$ the triangle is equilateral, and when θ is near $180°$ it becomes very obtuse. The self elastance is plotted as a function of θ along with the constant self elastance of a MSM sphere with the same area ($R = \sqrt{A/4\pi}$) in Fig. 2.41(b). The assumption of equal area is often a very good assumption, especially for convex shapes.[63] This assumption is used in Reference [64] to calculate the self capacitance of many varied spacecraft shapes. The elastance of the triangle is very small when it is either very obtuse or very acute, and reaches a maximum when the angle is $60°$. This is because $\mathcal{R}$ takes on larger values when the triangle is long and skinny in either limit, although the elastance is smaller for a very obtuse triangle than a very acute one. The effective sphere always overestimates the self elastance if computed on the basis of equal area, and this is exaggerated for very acute or obtuse triangles.

Next consider the mutual elastance. For two MSM spheres, it is simply given by $1/4\pi\epsilon_0 d$ where d is the separation between the centroids. For two MoM triangles, it is the double integral over the area and is therefore attitude dependent. To investigate this one equilateral triangle is held with its centroid at the origin but has it's attitude free while another identical triangle moves along the z axis and stays parallel to the x, y plane. The mutual elastance for this pair of triangles is shown alongside the mutual elastance for a pair of spheres with the same centroid separation in Fig. 2.41(c). Special care is taken to ensure that the bottom triangle does not rotate so far that it intersects the upper triangle when the two triangles are close. The triangles both have all side lengths equal to 1 m and have their centroids on the z axis. For very close separations, the MSM is a little higher than the mean MoM solution but for far distances on the order of the edge length
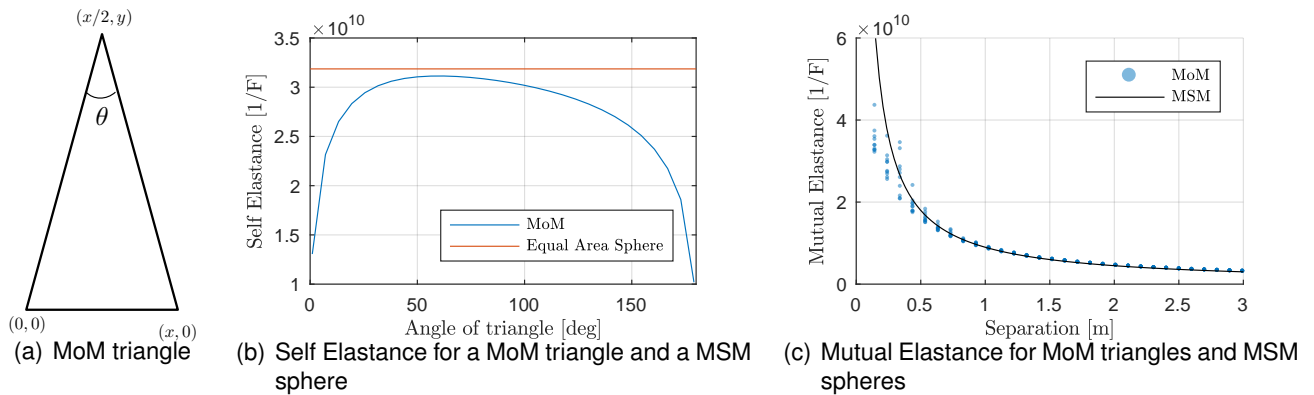
(a) MoM triangle

(b) Self Elastance for a MoM triangle and a MSM sphere

(c) Mutual Elastance for MoM triangles and MSM spheres

Figure 2.41: *Comparison of MoM and MSM elements*

MSM agrees very well with the MoM average, and the MoM variation becomes very small. This is because as the vector PA gets larger and larger, the small u and v terms matter less.

2.1.4.5 MoM inspired MSM models

To make a MSM model from a MoM model, the mutual terms do not need to be used because the MSM solution matches them quite well using the centroid assumption. However, the radii of the MSM spheres do not match well using the equal area assumption, and there is a lot of sensitivity to the type of triangle. Therefore, a mapping is created to find the radius of the MSM sphere that will match the diagonal in the MoM elastance matrix:

$$R_i = \frac{1}{4\pi\epsilon_0 S_{i,i}} \tag{2.140}$$

spheres with this radius are placed at the centroid of each triangle to create the SMSM model. In prior work, all SMSM spheres had the same radius, and it was varied in order to match self capacitance.[2] This approach allows for non-homogeneous radius SMSM models to be created. This process is illustrated on a homogeneous case where all MoM triangles (and therefore all SMSM spheres) are the same, and a non-homogeneous case where the MoM triangles are not the same size.

The first row in Fig. 2.42 shows the translation of a homogeneous MoM model to a SMSM model on a square plate. This model has 50 triangular elements and all triangles are identical which makes all spheres identical. Although the diagonal elements are matched perfectly, the self capacitances of the two models differ by about 0.3% because the self capacitance is a function of the non-diagonal elements as well. The second row in Fig. 2.42 shows the translation from a non-homogeneous MoM model with 494 elements to a SMSM model for a cylinder. The non-uniformity comes from the circular end caps where the triangles must change size and shape to mesh the surface completely. The area of the elements varies from 0.013 m^2 to 0.024 m^2, with the smallest triangle being at the very center. The diagonals of the MoM-derived elastance matrix are then transformed to sphere radii to create the non-homogeneous SMSM model shown in Fig. 2.42(e). The radii in this model vary from 3.3 cm to 4.5 cm, a smaller variation then the area of the MoM triangles. These two models only differ by 0.14% percent in self capacitance even though the off-diagonals are not matched.
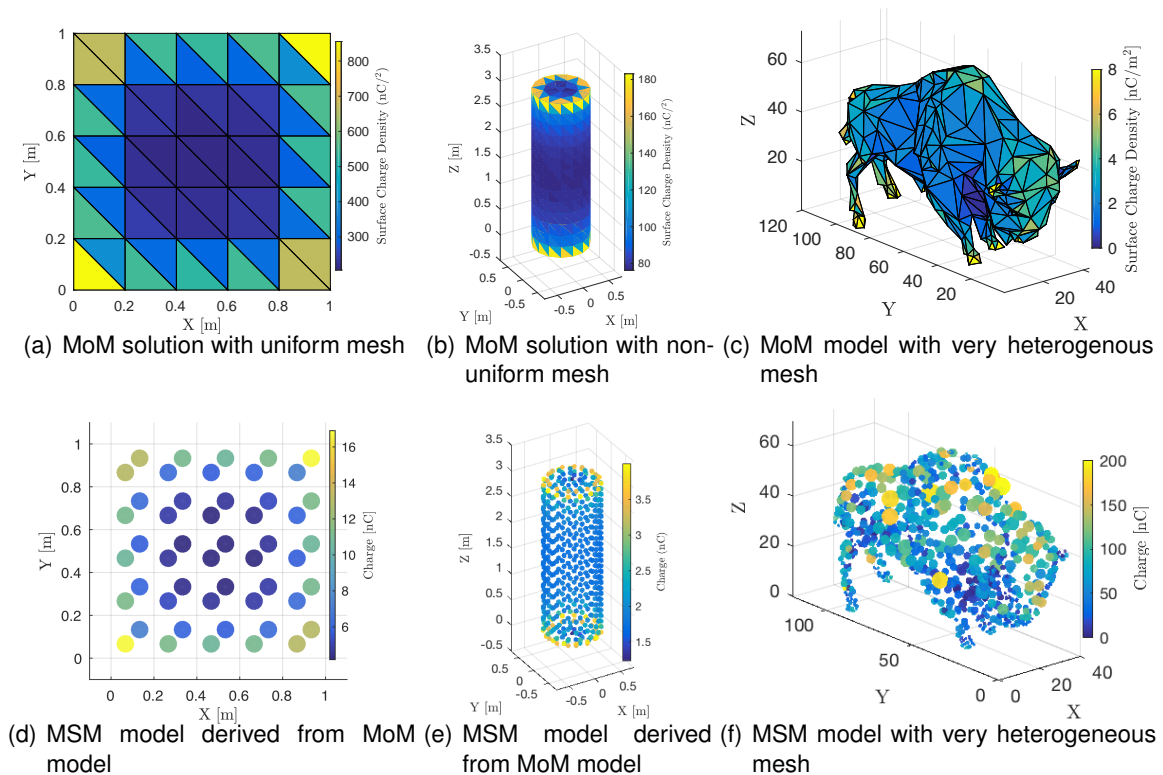
(a) MoM solution with uniform mesh

(b) MoM solution with non-uniform mesh

(c) MoM model with very heterogenous mesh

(d) MSM model derived from MoM model

(e) MSM model derived from MoM model

(f) MSM model with very heterogeneous mesh

Figure 2.42: *MSM model created from MoM model. Voltage is 10 kV in all plots*

2.1.4.6 Two Body Force and Torque

The self capacitance of simple shapes such as plates and cylinders when computed with MoM and MSM is a good proxy for how the two models compare, but it is not the only pertinent comparison. Close proximity electrostatic tugging is one driver of the need for accurate and fast electrostatic solvers so this section compares MoM to SMSM for the ET. The tug craft is modeled as a 1 m cube with two 2×1 m solar panels charged to +30 kV and is located at $r = [5, 2, 1]^T$ which puts it at a center to center distance of 5.48 m away from the debris object - a spent rocket stage modeled as a 3×1 m cylinder charged to - 30 kV. For some tug attitudes, the solar panels can come much closer to the cylinder. In most ET applications, the standoff distance is a more conservative 10-50 m so this case represents one of the harshest electrostatic situations to solve. The truth model for this situation is taken as a very high resolution (10 cm) MoM model which uses 2100 elements for the cylinder and 1656 elements for the tug and is shown in Fig. 2.43. The color scale is capped at 1000 nC/m^2 in this plot, but the actual charge density goes up to almost 4000 nC/m^2 at the corners of the solar panels. Since the electrostatic solution is highly attitude dependent, the force and torque on the cylinder are computed at 16 representative tug attitudes and stored in a master text file. For each of the 16 attitudes, more than 1.7 million numerical integrals are done to make the elastance matrix. then, this 3756×3756 matrix is solved for the charge on each element. Finally, almost 3.5 million numeric integrals are done to find the force and torque on both bodies.

Next, compute the force and torque using lower fidelity MoM and SMSM models while keeping track of the computation time. There are many modifications that can be made to both MoM and SMSM to make them faster and more accurate for the ET case that are also analyzed along with the standard ones. Firstly, since both the tug and debris are assumed to be rigid bodies, the two diagonal blocks in the elastance matrix shown in Eq. (2.137) do not have to be recomputed at
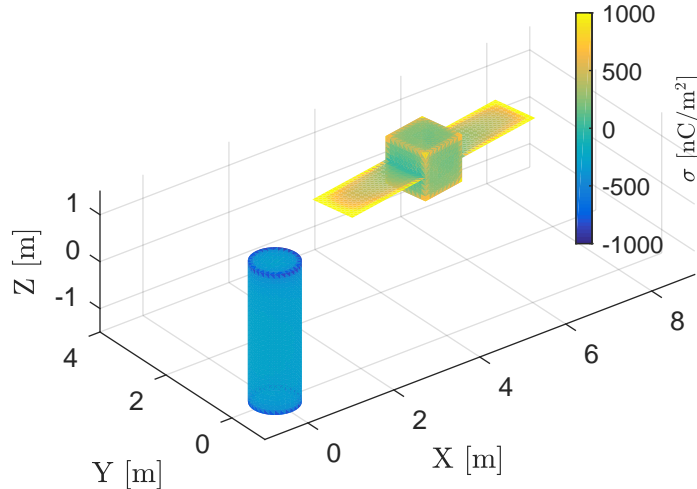
Figure 2.43: *High fidelity MoM truth model for close-proximity electrostatic tugging*

each time step. Second, the off diagonal blocks can be computed with SMSM using the centroid assumption even if the diagonal blocks are made using MoM. The off diagonal blocks can also not be counted at all which ignores all induced effects. The force and torque can be computed with either MoM of SMSM as well. Even a pure SMSM model can have all it's sphere radii varied to match the self capacitance of the truth model rather than from the MoM model that created it. In all, 7 different MoM/SMSM hybrid models are analyzed for this case. The name of each one and what make it unique is shown in Tab. 2.12.

Table 2.12: *MoM and SMSM variants used*

Name	Diagonal Blocks	Off-Diagonal Blocks	E-Field	Notes Notes
Full MoM	MoM	MoM	MoM	
Fast MoM	MoM	SMSM	MoM	executes in about 80% of Full MoM time.
Faster MoM	MoM	MoM	SMSM	executes in about 20% of Full MoM time
Fastest MoM	MoM	SMSM	SMSM	executes in less than 1% of Full MoM time
Self MoM	MoM	0	SMSM	no induced effects included
SMSM	SMSM	SMSM	SMSM	
Tuned SMSM	SMSM	SMSM	SMSM	sphere radius tuned to match C_S

For each model variant, the mesh is computed with either 258, 500, 830, 1236, or 1730 total elements and then compared to the truth model made with 3756 elements at each of the 16

attitudes. The performance of all 7 model variants is shown in Fig. 2.44. The error is computed as

$$\text{Error} = \frac{1}{2}\left(\frac{||\boldsymbol{F} - \boldsymbol{F}_T||}{||\boldsymbol{F}_T||} + \frac{||\boldsymbol{L} - \boldsymbol{L}_T||}{||\boldsymbol{L}_T||}\right) \tag{2.141}$$

where $\boldsymbol{F}, \boldsymbol{L}$ are the predicted force and torque and $\boldsymbol{F}_T, \boldsymbol{L}_T$ are the true force and torque. The execution time is found using Matlab's tic and toc functions. Despite the same math being performed, the execution time varies considerably. This variance would likely disappear and the overall time would decrease substantially on a more flight-computer-like system. Each dot in Fig. 2.44 represents the error and time for a different model variant with a different number of elements at at different attitude. The model variant is indicated by the color in the figure legend. The number of elements is shown by grouping - each shaded group of points have the same number of elements. Lines of the same color trace the means of both the error and execution time for each model variant. As the number of elements increases, the error drops and and the execution time increases - the groups of points with 258 elements are in the upper left corner of the plot and the groups with 1730 total elements are in the bottom right.
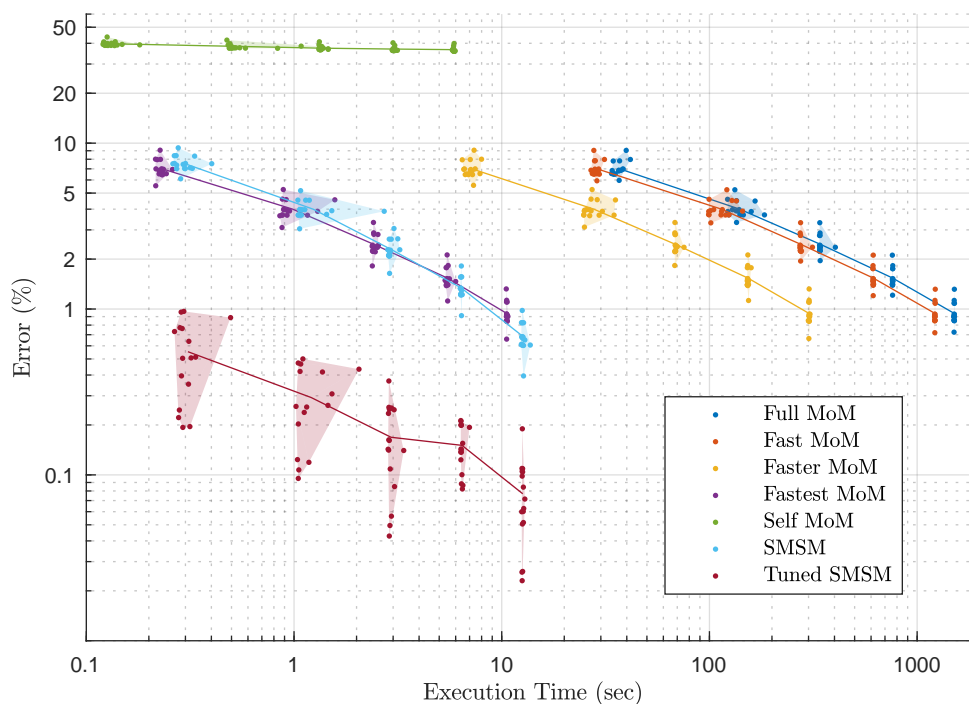

Figure 2.44: *Time and error shown for different force and torque prediction schemes*

    The Full MoM performance is shown in dark blue and is furthest to the right which means it is the slowest. If the number of elements is increased up to 3756, it would have exactly 0% error since that is how the truth model is made. Even with a relatively small (258) number of elements, the error is still below 10% even at this very close separation. The next model variant is the Fast MoM which uses the SMSM approximation for the off diagonal blocks of the elastance matrix. This simplification does not introduce significant errors, but saves a considerable (20%) amount of computation time. The next variant is "Faster MoM" which uses the SMSM approximation for the E field but not for the off diagonal blocks. This also does not introduce significant errors but saves

a lot (80%) of computation time. The next variant is Fastest MoM which uses SMSM for both the off diagonal blocks and the E field. This variant runs very fast when compared to the Full MoM solution and only gives up a very small amount of accuracy. The last MoM variant is the Self MoM which does not include any induced effects. Because of this, there are no mutual terms to compute and it runs the fastest of any model. However, it also has the worst errors ($\sim 40\%$) of any model. This shows just how important the mutual interaction is at this close distance. Further away, these errors would drop considerably. The next model is SMSM which is almost identical to Fastest MoM in both time and accuracy. Fastest MoM is slightly faster and more accurate, especially with a small number of elements. The last model variant is tuned SMSM. This model uses the centroids from the MoM model but uniformly sizes all spheres in order to match the self capacitance found from the truth model. The spheres are all the same size even though the triangles are different for the cylinder. This model is by far the most accurate, being almost an order of magnitude more accurate than any other model with the same number of elements.

2.2   Research Thrust 2: Flexible Shape MSM Applications

2.2.1   Motivation

In the severely resource-constrained environment of space, the concept of low-mass and fuel-less electrostatic actuation has been considered an attractive proposition throughout the space age. Initial studies, originating with Reference![65] in 1966, investigated electrostatic inflation of reflective membrane structures as a mass effective alternative to traditional deployable antennas. Later investigation of electrostatic membrane inflation has shown these forces to be sufficient to maintain inflation under orbital perturbations, with the assistance of mechanical structures to achieve a desired shape.[66,67] The use of mechanical constraints to shape the membrane eliminates the need to model the dynamics of the system, as experimental results demonstrated that the membrane will inflate satisfactorily given sufficient electrostatic pressure.

However, not all membranes subject to electrostatic inflation are constrained or designed to inflate in a predictable fashion. This is particularly relevant in the field of High Area-to-Mass Ration (HAMR) debris objects in high altitude orbits, especially in the geosynchronous region (GEO). The orbits of these objects are more influenced by electrostatic perturbations than other craft, and strongly subject to variations in solar radiation pressure resulting from attitude variation.[68] For the rigid flat plate considered by References [27] and [69], however, electrostatic forces are a far smaller influence on the orbit than attitude perturbations. Through the coupling with the solar radiation pressure they are shown to impact the orbital motion.[27,47]

One category of HAMR debris object is likely to see much larger orbital effects because of electrostatic perturbations: flexible materials, such as pieces of aluminized mylar. As the mylar flexes and changes its shape, the resulting solar radiation pressure will change accordingly. In Reference [70] the perturbed orbit of flexible mylar is investigated. However, the source of such flexing, which can include electrostatic charging, is not considered in this prior work. In GEO, the relatively hot plasma environment creates conditions that can charge conducting objects to potentials as high as -30 kV.[69] A crumpled sheet could become stretched out by electrostatic inflation under such conditions, dramatically changing its surface area, while Lorentz forces could decrease the surface area by crumpling a flat sheet. Such dramatic changes in area will significantly perturb the object's orbit by altering the effect of SRP and, in Low Earth Orbits (LEO), the atmospheric drag.

Modeling the motion of a flexible material under electrostatic actuation is challenging due to the
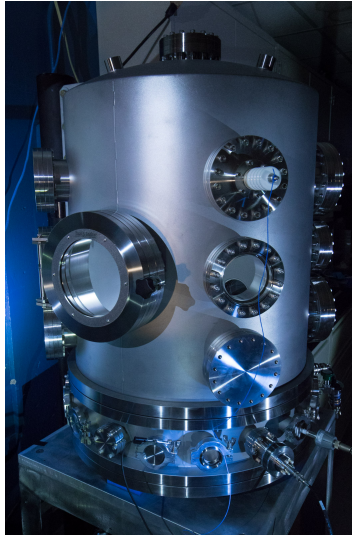
Figure 2.45: *The ECLIPS space environment simulation testbed*

complex electrostatic force interactions present. This work seeks to apply the Multi-sphere Method (MSM), a system originally developed for faster-than-realtime approximation of the electric field about a general rigid object, to estimate electrostatic forces and torques between close-proximity Resident Space Objects (RSOs). Thus far, MSM has been based on an assumption of a rigid object with a continuously conducting surface. Here, the fixed shape assumption is relaxed and the MSM methodology applied to simulating the electrostatic deflection of a flexible one dimensional structure in vacuum, which is approximated experimentally by a thin strip of aluminized mylar. The numerical simulation of the deformation is compared to experimental results. The Electrostatic Charging Laboratory for Interactions between Plasma and Spacecraft (ECLIPS) chamber located within the Autonomous Vehicle Systems (AVS) Laboratory at the University of Colorado Boulder (CU Boulder), illustrated in Figure 2.45, is used to create a high-vacuum environment for the experiments. The unforced strip is used to develop an MSM model, which is then used to simulate the behavior of the strip when an electrostatic charge is added to it and an electric field. The numerical results for the strip deflection are compared to the experimental results to assess the validity of the MSM method for simulating non-rigid bodies.

2.2.2   MSM Overview

MSM is an accurate, computationally efficient method of approximating the electrostatic interactions between conductors.The general shape is replaced with a series of body-fixed spheres whose radii are chosen such that the resulting electrostatic field closely approximates the true field generated by this shape. Two main categories of MSM exist: Volume MSM (VMSM) and Surface MSM (SMSM).[2] VMSM requires that both sphere radii and placement are optimized to match forces and torques,[3] capacitance,[5] or electric fields.[55] SMSM, on the other hand, places spheres equidistantly on the surface of the modeled object, and optimizes only the sphere radii to match any of the physical quantities listed above. For the investigation to follow, a SMSM model using capacitance matching is employed. This optimization method is chosen because capacitance matching is more reliable than force and torque matching.

   A significant challenge of applying MSM on-orbit is the development of MSM models for poorly-understood objects such as debris. Several solutions to this problem have been proposed. One

analyzes orbital perturbations due to Coulomb interactions between a servicer craft whose voltage is known and a debris object to determine the charge distribution on the debris and develop an MSM model.[71] Another uses a dual-Langmuir probe system on board a servicer craft to determine the proper MSM model for a rotating craft or object.[72]

Figure 2.39 depicts the MSM concept. The voltage on each of the spheres shown is related to the charge on that sphere by

$$V_i = k_c \frac{Q_i}{R_i} + k_c \sum_{j=1, j \neq i}^{n} \frac{Q_j}{r_{i,j}} \tag{2.142}$$

where $k_c = 8.99 \times 10^9$ Nm^2/C^2 is Coulomb's constant, R_j is the radius of the jth sphere, and $r_{i,j}$ is the distance between the ith and j^{th} spheres. These relations can be rewritten into a single matrix equation.

$$\begin{pmatrix} V_1 \\ V_2 \\ \vdots \\ V_n \end{pmatrix} = k_c \begin{bmatrix} 1/R_1 & 1/r_{1,2} & \dots & 1/r_{1,n} \\ 1/r_{2,1} & 1/R_2 & \dots & 1/r_{2,n} \\ \vdots & \vdots & \ddots & \vdots \\ 1/r_{n,1} & 1/r_{n,2} & \dots & 1/R_n \end{bmatrix} \begin{pmatrix} Q_1 \\ Q_2 \\ \vdots \\ Q_n \end{pmatrix}, \quad \mathbf{V} = [S]\mathbf{Q} \tag{2.143}$$

The matrix $[S]$ is called the elastance matrix. Another, well-known expression relating charge to voltage, $\mathbf{Q} = [C]\mathbf{V}$ indicates that the capacitance is the inverse of the elastance matrix.

$$\mathbf{Q} = [S]^{-1}\mathbf{V} \tag{2.144}$$

This form is preferable in the electrostatic force and torque evaluation process as the voltage is usually known and the dynamics are dependent on charge. For a single rigid structure, the capacitance matrix is constant. If multiple rigid bodies are modeled then diagonal blocks of the elastance matrix which — when inverted — represent the self-capacitance of each rigid body are constant, while the off-diagonal blocks very with time as the relative positions of these bodies varies.[2,3,55] Expansion to consider a flexible structure also requires a time varying elastance matrix. The MSM radii R_j are held constant, but the relative distances $r_{i,j}$ change as the object flexes. In contrast to prior work, even the self-capacitance matrix of such a flexible object will now vary with time.

This study presents the following hypothesis. To adjust the existing MSM electrostatic force and torque modeling technique to a body with a time varying shape, the body is first decomposed into a finite set of surface segments. The relative degrees of freedom between these surface elements are assumed to be known, i.e. how does one element rotate or hinge relative to another element. Next, either a VMSM or SMSM model is created for each shape element. These spheres are now on fixed locations relative to this element. As the shape changes and the relative position of the surface elements vary with time, the locations of the spheres must be updated at each time step. This creates a time varying elastance matrix that is readily setup using the MSM modeling technique. This modeling approach is justified as Poisson's electrostatic field equation allows for super-position of charge solution. This is how we are able to use MSM to model the electric field between neighboring rigid space objects. Losses in numerical accuracy occur because the MSM model is only an approximation of the true electric field about this shape segment. If two bodies have separation distances that are on the order of the spacecraft dimensions, prior work has shown that these approximations are as good as 1% or less.[55] To apply this to a flexible shape the segments are essentially docked with a flexible joint. The accuracy is thus determined through
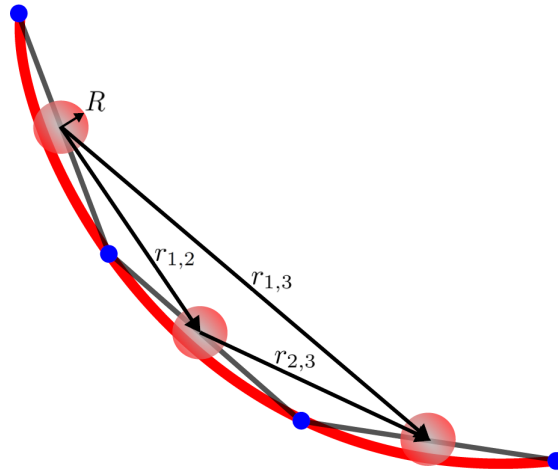
Figure 2.46: *MSM model of multi-link pendulum*

both the number of shape segments (i.e. the finite element meshing) and the number of spheres used to represent the electric field of an individual mesh.

To illustrate how this flexible shape MSM is set up, consider Figure 2.46. For this case, it is assume that the radii of the MSM spheres are all similar, but this is not a necessary condition. The charge-voltage relationship is then setup with the MSM formulation to yield the following elastance matrix.

$$
\begin{bmatrix} V_1 \\ V_2 \\ V_3 \end{bmatrix} = k_c \begin{bmatrix} 1/R & 1/r_{1,2} & 1/r_{1,3} \\ 1/r_{2,1} & 1/R & 1/r_{2,3} \\ 1/r_{3,1} & 1/r_{3,1} & 1/R \end{bmatrix} \begin{bmatrix} Q_1 \\ Q_2 \\ Q_3 \end{bmatrix}
\tag{2.145}
$$

The diagonal block elements of the elastance matrix remain constant as the body flexes, while the off-diagonal elements must be updated each time step with the current relative positions of the surface elements.

2.2.3 Comparison to Analytical Capacitance Solution

This paper applies this flexible MSM concept to a 1-dimensional, flexible conducting structure. For example, Figure 2.46 shows how a flexible wire is modeled as a multi-link pendulum with MSM spheres placed at the center of each link. The capacitance of a long, thin, straight wire is given by Reference 73.

$$
C = \frac{l}{k_c \Lambda} \left[1 + \frac{1}{\Lambda}(1 - \ln 2) + \frac{1}{\Lambda^2} \left(1 + (1 - \ln 2)^2 - \frac{\pi^2}{12} \right) + \mathcal{O}\left(\frac{1}{\Lambda^3} \right) \right], \quad \Lambda = \ln\left(\frac{l}{a} \right)
\tag{2.146}
$$

where l is the length of the wire and a is its radius. This equation is valid for large Λ, which requires that the wire length is much greater than the radius. This scalar value is used to optimize the radius R used in the model. The comparison to the capacitance described in Eq. (2.144) is accomplished by summing the members of the matrix capacitance as in Eq. (2.147).

$$
C_{\text{scalar}} = \sum_{j=1}^{n} \sum_{i=1}^{n} C_{i,j}
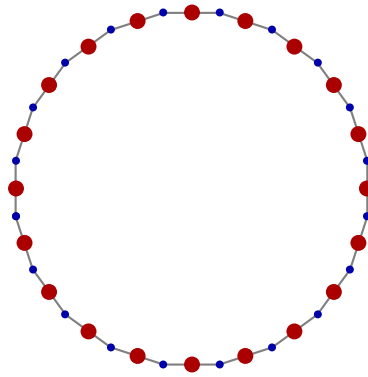\tag{2.147}
$$

Figure 2.47: *20-link SMSM model of an anchor ring. The blue circles indicate the hinge locations, while the red accurately represent the SMSM sphere radii optimized using Eq. (2.146)*

If the wire changes shape, Eq. (2.146) no longer holds. However, the optimization to generate the sphere radii on the diagonal of the elastance matrix is computationally expensive, and determining the nominal capacitance to which to optimize is non-trivial for complicated shapes such as a flexing wire. The error resulting from holding these diagonal components constant while letting the off-diagonal terms in Eq. (2.145) vary as the shape changes is investigated to determine if re-optimization is strictly necessary.

The case of an anchor ring is considered, as it is another configuration for which there an analytic capacitance has been determined. Reference 74 shows that the capacitance of an anchor ring whose cross sectional radius r is small compared to the ring radius ρ is

$$C = \frac{\pi \rho}{k_c \ln \left(8\rho/r \right)} \tag{2.148}$$

Two configurations of a 20-link system similar to that shown in Figure 2.46 are compared. First, the link is arrayed as a straight line and the SMSM sphere radii are optimized to match the capacitance in Eq. (2.146). The SMSM system is then rearranged into a ring shape without changing the SMSM sphere locations within each link, or the sphere radii to match the capacitance of the ring. The off-diagonal terms of the capacitance matrix account for this new geometry and the sum of all matrix elements is compared to the analytical result in Eq. (2.148).

The resulting non-optimized SMSM capacitance of the ring calculated using the elastance matrix is within 0.1% of the analytic solution given by Eq. (2.148) for a 20-link system. A portion of this error is due to the discrete nature of the ring in Figure 2.47. Figure 2.48 shows that the difference between the SMSM capacitance and that from Eq. (2.148) decreases with the number of links, but is still small for low-order systems. Therefore, the capacitance can be well-approximated by an SMSM model without re-optimizing at each time step.

2.2.4 Charged Wire Equations of Motion Using Flexible MSM

As illustrated in Figures 2.46 and 2.49, the flexible, conducting wire studied is approximated as a multi-link pendulum system with SMSM spheres placed at the center of each link. In Figure 2.49, a single force is shown at each sphere position for clarity, but in the model all three forces are applied at all three locations. The sphere position is held at link-center due to the symmetry of the simple shape segments. To account for the stiffness of the wire, torsional springs are simulated at the hinge points of the model. Damping is also applied at these points to account for energy being removed as the modeled wire flexes, though this is not explicitly labeled in Figure 2.49. The
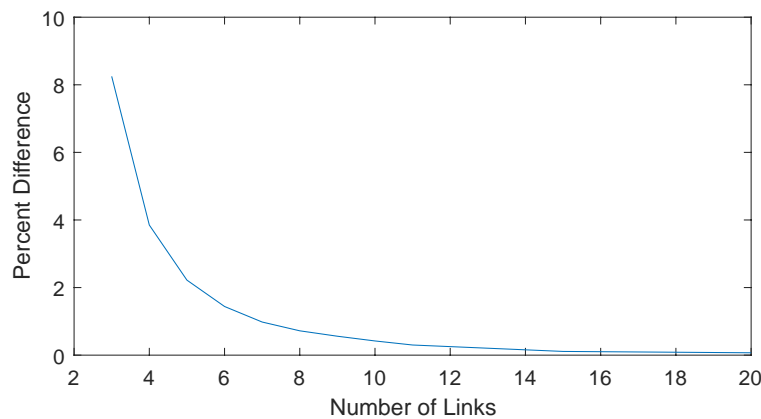
Figure 2.48: *Percent difference between SMSM and analytic anchor ring capacitance for various numbers of links*
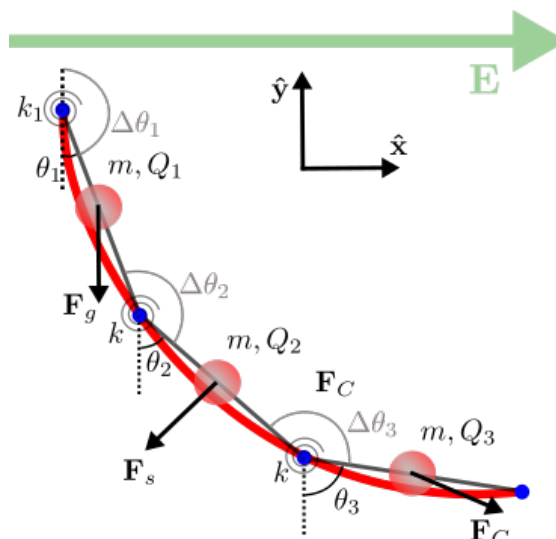

Figure 2.49: *SMSM model of a wire showing forces*

spring constants are the main tunable parameter of the flexible membrane structure, and empirical methods are applied in the next section to provide their nominal values. Note that in Figure 2.49, the first spring is labeled with a different spring constant, k_1, than the others. This accounts for an attachment mechanism in the model that affects only the first link. Another deviation from the normal material spring constant occurs at the point of the sharp bend introduced in the strip, as seen in Figure 2.51. This kink introduced near the center of the experimental strip facilitates a significant change in the shape of the strip, providing a more interesting shape to model. A schematic of the model and forces are shown in Figure 2.49. Note that the directions of the gravitational force $\mathbf{F}_g$ does not change, while the Coulomb and spring forces, $\mathbf{F}_C, \mathbf{F}_s$ change as the wire deforms. The direction of the Coulomb force changes in time because, in addition to the static electric field in the $\hat{x}$ direction, mutual Coulomb repulsion is applied at each sphere. This is accounted for in the direction of $\mathbf{F}_C$ in Figure 2.49.

The gravitational force and spring torque are related to the mass of a link m and the relative

angles between two links $\Delta\theta$, respectively.

$$\mathbf{F}_g = mg(-\hat{\mathbf{y}}) \tag{2.149a}$$

$$\boldsymbol{\tau}_s = k(\Delta\theta - \Delta\theta_0)(-\boldsymbol{\Delta\hat{\theta}}) \tag{2.149b}$$

Here g is the gravitational acceleration on Earth's surface, k is the spring constant of the torsional spring, $\Delta\theta_0$ is the equilibrium angle between the two links, and $\boldsymbol{\Delta\hat{\theta}}$ is the unit direction vector about which the two shape segments hinge. Assuming a perfectly vertical and constant gravitational field,the potential energy of each link relative to an initial vertical position can be expressed in the well known form

$$U_g = mg(y - y_0) \tag{2.150}$$

where $(y - y_0)$ is the height of the center of mass above the equilibrium position.The derivation of spring potential energy for the multi-link system is less obvious, but is clearly dependent on the difference in angles between any two links.

$$U_s = \frac{1}{2}k(\Delta\theta - \Delta\theta_0)^2 \tag{2.151}$$

The $\Delta\theta_0$ term is included in Equation Eq. (2.151) to account for the shape in Figure 2.51. As mentioned above, the spring constant k for the first and third hinge point of the model is varied from the other to account for the attachment mechanism and introduced kink, respectively. The kinetic energy of each link consists of two components: translation of the center of mass and rotation of a thin rod about its end.

$$T = \frac{1}{2}m\mathbf{v}_{\text{com}} \cdot \mathbf{v}_{\text{com}} + \frac{1}{2}\boldsymbol{\omega}^T I \boldsymbol{\omega} = \frac{1}{2}mv_{\text{com}}^2 + \frac{1}{6}ml^2\dot{\theta}^2 \tag{2.152}$$

Above, v_{com} is a link's center of mass velocity, l is the length of a link, and $\dot{\theta}$ is the inertial angular velocity of a link. The Lagrangian of the multi-link pendulum system is therefore

$$\mathcal{L} = T - U = \sum_{i=1}^{n}\left(\frac{1}{2}mv_{\text{com}_i}^2 + \frac{1}{6}ml\dot{\theta}_i^2 - mg(y_i - y_{0_i}) - \frac{1}{2}k_i[\Delta\theta_i - \Delta\theta_{0_i}]^2\right) \tag{2.153}$$

where n is the number of links. These n, coupled differential equations are numerically solved simultaneously. The dynamics of the system are determined from Lagrange's Equation.

$$\frac{\mathrm{d}}{\mathrm{d}t}\left(\frac{\partial\mathcal{L}}{\partial\dot{q}_i}\right) - \frac{\partial\mathcal{L}}{\partial q_i} = \mathcal{Q}_i \tag{2.154}$$

Here, q is a generalized coordinate — in this case the inertial angle of a link — and $\mathcal{Q}$ is the sum of generalized, non-conservative forces and torques on a given link. Only two such influences are included in this model: a velocity damping term and the Coulomb force. Velocity damping was chosen for computational efficiency — a significant challenge of this work — and because exercises with the model indicated that neither the type nor rate of damping affected the steady state of the experimental setup. Other damping terms would have been investigated if the transient behavior of the system were the focus of this work. The value of b is a scaling coefficient that determines the settling time of the system. As indicated previously, changing the settling time of the system does not affect the steady-state position of the multi-link system. It is therefore set to

a value that brings the modeled wire to its steady-state quickly, as some experiments took several minutes to settle.

The Coulomb force is applied as a generalized force because, generally, the charge on each sphere is allowed to vary. Under this condition, the force is not conservative. Since the capacitance matrix varies as the shape of the wire changes, the Coulomb force is not conservative and therefore must be implemented as a generalized force in the Lagrangian formalism. The forces and torques used to calculate the generalized force on each link are

$$\mathbf{F}_{C_i} = Q_i \left(\mathbf{E} + \sum_{j \neq i}^{n} \frac{Q_j}{(r_i - r_j)^3} (\boldsymbol{r}_i - \boldsymbol{r}_j) \right), \quad \boldsymbol{\tau}_{d_i} = -b v_i^2 \hat{\boldsymbol{v}}_i \tag{2.155}$$

In Eq. (2.155), Q is the charge on a given sphere and $\boldsymbol{r}$ its position vector; $\mathbf{E}$ is the background electric field; v is the velocity of a given link; and b is a scaling factor for the damping, as described above. For the experiments in this paper a flat, constant electric field is used. Superimposed upon this background electric field is the mutual repulsion of the strip which is included as the second term in the Coulomb force in Eq. (2.155). In the MSM framework, this is modeled as mutual repulsion between each MSM sphere. Therefore, the Coulomb force experience by each link varies not only as the charge on each strip does, but as the wire deforms and the relative distances between the MSM spheres change.

The equation for the generalized force on the ith sphere is

$$\mathcal{Q}_i = \sum_{j=1}^{n} \mathbf{F}_j \cdot \frac{\partial \mathbf{r}_j}{\partial q_i} \tag{2.156}$$

where j is a sum over all links within the system, i indicates the relevant equation of motion, and $\mathbf{r}_j$ is the position on the jth link at which the total force $\mathbf{F}_j$ is applied.

Mathematica is used to generate and solve the full equations of motion of the multi-link model. Numerical solutions to the equations of motion are used because, for large numbers of links, the analytical forms are extremely complex. Even without analytic evaluation, only a 5-link system could be used. The `NDSolve` function is given initial conditions derived from the experiments described in the next section and integrates the equations of motion to provide the inertial angles and their corresponding angular velocities at each time step.

2.2.5 Experimental Design & Analysis

2.2.5.1 Experimental Setup

Validation of the MSM system to flexible structures is achieved through comparison with experiment. A parallel plate capacitor is chosen to produce a flat electric field. This work expands on prior analysis performed in atmosphere, extending those experiments to vacuum. Experiments were conducted within the ECLIPS chamber pictured in Figures 2.45 and 2.50(a) at pressures below 10^{-6} Torr to avoid electrostatic discharge events. The desire for a more space-like environment motivated the vacuum experiments. Air drafts and ionization of ambient air in atmospheric tests complicated previous analyses.[75]

Figure 2.50(a) shows the experiment setup. The stand-in for a one-dimensional conducting structure is a thin strip of aluminized mylar, which consists of two coatings of 100 Å thick aluminum on either side of 7 μm mylar substrate. The aluminum coatings, which are normally isolated by the mylar are connected by placing sections of the multi-strand wire from the power supply on both
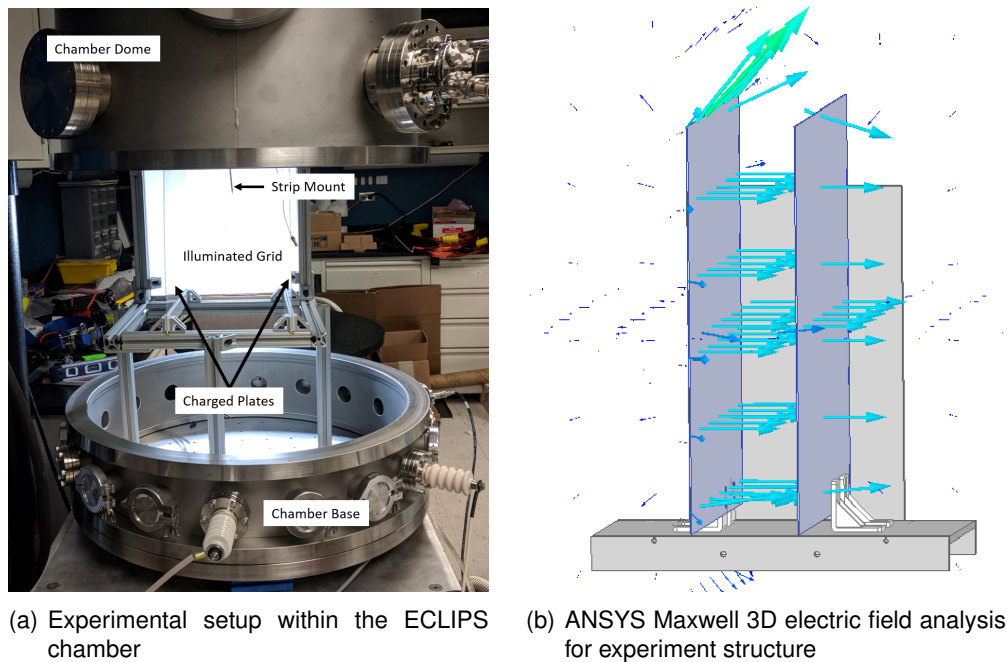
(a) Experimental setup within the ECLIPS chamber

(b) ANSYS Maxwell 3D electric field analysis for experiment structure

Figure 2.50: *Experimental Setup Illustration*

sides of the strip. This strip is suspended mid-way between the cathode and anode of the parallel plate capacitor. This allows the strip to be charged to different potentials than the plates. This mimics the space environment, as environmental currents to RSOs are not necessarily dependent on the local electromagnetic fields.

A Spellman CZE3000 high voltage power supply (HVPS) controlled by LabVIEW via a National Instruments USB data acquisition (DAQ) unit is used to put an excess of charge on the thin strip. The cathode of the parallel plate capacitor is attached to a SL300 HVPS, while the anode is connected to ground. A strip of dimension 7.2 cm $\times$ 0.1 cm was used for all experiments. A kink was introduced at the center of the strip to encourage a significant shape change — a more interesting situation to model than a flat strip merely bending at the attachment point.

The commercial finite element solver Maxwell 3D is used to verify that a flat, constant electric field is generated by the parallel plate capacitor used. Figure 2.50(b) shows the electric field of a modified experimental system from that shown in Figure 2.50(a) imported into Maxwell 3D with accurate material properties and a voltage drop of $\Delta V = 5$ kV across the plates. This simulation was run at several voltages to determine the electric field for a variety of test voltages. All matched the well-known parallel plate capacitor equation: $E = \frac{\Delta V}{d}$ where d is the plate separation. Note that Figure 2.50(b) shows that the electric field between the plates is flat everywhere except near edges. The aluminized mylar strip was therefore positioned near the middle of the setup, far from any edges in all experiments.

2.2.5.2 Experiment Analysis

To analyze the experiment as various voltages were applied to both the strip and the cathode of the parallel plate capacitor depicted in Figure 2.50(a), images were taken and loaded in MATLAB for each trial. Edge finding algorithms in MATLAB Image Processing toolbox were used to differentiate the wire from its surroundings. A grid of holes was drilled into a sheet of Delrin using a CNC
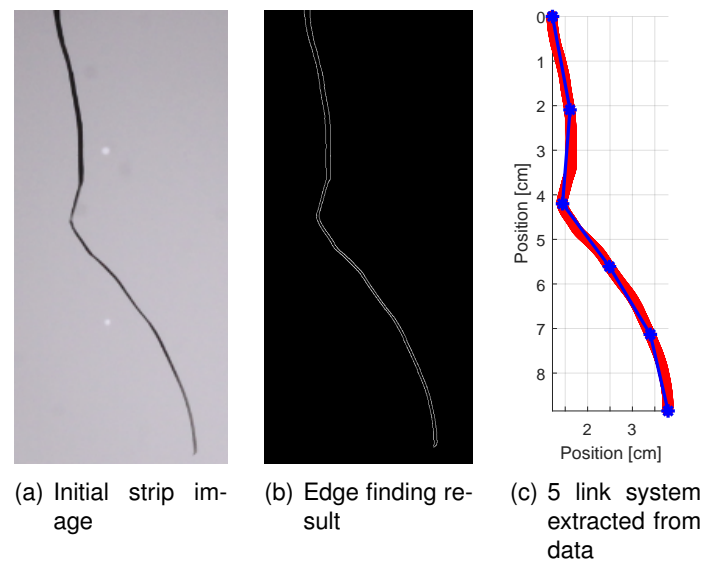
(a) Initial strip image

(b) Edge finding result

(c) 5 link system extracted from data

Figure 2.51: *Image analysis results*

machine and placed behind the wire to identify the conversion factor from pixels to inches. The orientation of the grid points in the Delrin sheet provided an arbitrary vertical axis to which the image can be aligned eliminating the need to align the camera itself. Furthermore, the grid points allowed for a comprehensive total alignment and warp analysis on the background Delrin sheet.

After isolating the strip edges as seen in Figure 2.51, the positions of the edges were averaged at each y-value to find the centerline. The resultant centerline data was smoothed to reduce high frequency noise prior to curve fitting using a Gaussian-weighted moving average filter. The data was then divided into two segments, split by the kink that had been introduced near the middle of the mylar strip. A piecewise cubit Hermite interpolating polynomial was then fit to the smoothed data on each side of the strip.

Once the interpolating function is obtained, it is used to develop a discrete, n-link system for comparison with the n-link model; here, $n = 5$, however this could be expanded to higher order systems in future work. The positions of the hinges found based on the curve fit were compared to steady state hinge positions for accuracy as shown in Figure 2.51. Moreover, the inertial and relative angles for each link in the n-link system are calculated to initialize the model and solve the equations of motion for the strip.

An analysis is performed on the grid points to quantify any camera misalignment and warp in the Delrin sheet in the background. Grid positions are found by calculating the center of mass of each grid point using the MATLAB's `regionprops` built-in function as they are shown in Figure 2.52. Once obtained, the distances between the grid points are used to derive the conversion factor from pixels to inches which was calculated to approximately $150 \text{ pixels}/\text{cm}$.

Finally, the standard deviation of the grid using the separation distances of the its intersections is calculated as the means to quantify any camera misalignment or warp in the Delrin sheet. The standard deviation came out to be 1.92 pixels which is significantly less than the pixel to cm conversion factor. This implies that the camera misalignment and warp in the Delrin sheet were negligible.
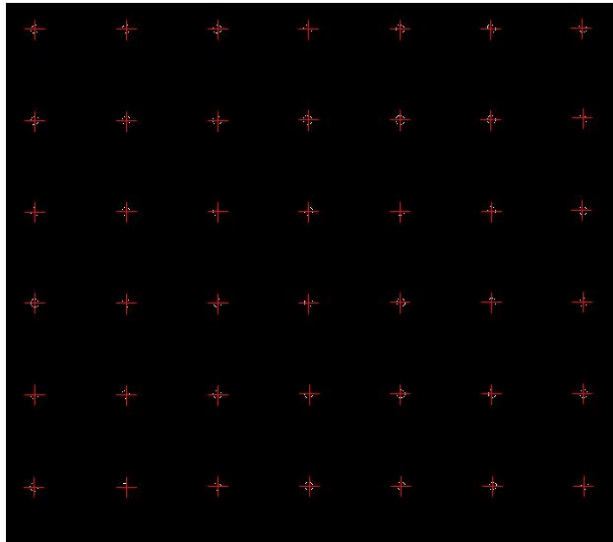
Figure 2.52: *Centers of the CNC grided points on the Delrin sheet detected using the Image Processing toolbox in MATLAB*

2.2.6   Results and Discussion

Table 2.13 shows the voltage levels for each experiment conducted. The plate voltage is applied to the cathode of the parallel plate capacitor while the anode is set to ground. Numerical simulations are compared to experimental data in Figure 2.53. Three separate spring constants are used to account for the attachment mechanism, kink, and the nominal portions of the strip. These values are tuned within the model to match the initial, unforced shape and position of the object to a Test 1. The spring forces determined from this exercise are used to initialize the model to an additional three experiments, each with different voltage parameters.

Figure 2.54 provides a quantitative indication of the position error between the hinge points in the model and those found from the experiment as shown in Figure 2.51.

It is clear from the figure that as the voltage gets farther from that in Test 1, the model match begins to degrade. Note however that the shape of the wire seems still to match that of the experiment. The SMSM model is developed to match Test 1, so having a good fit there is expected. When this same behavior was seen in previous atmospheric experiments, it was postulated that large strip voltages were ionizing the air, creating plasma that would then shield the strip from the background electric field. While this effect can't be ruled out completely as an actor in previous experiments, all experiments shown in Figure 2.53 were performed in vacuum, precluding this effect.

Table 2.13: *System voltages for experiments*

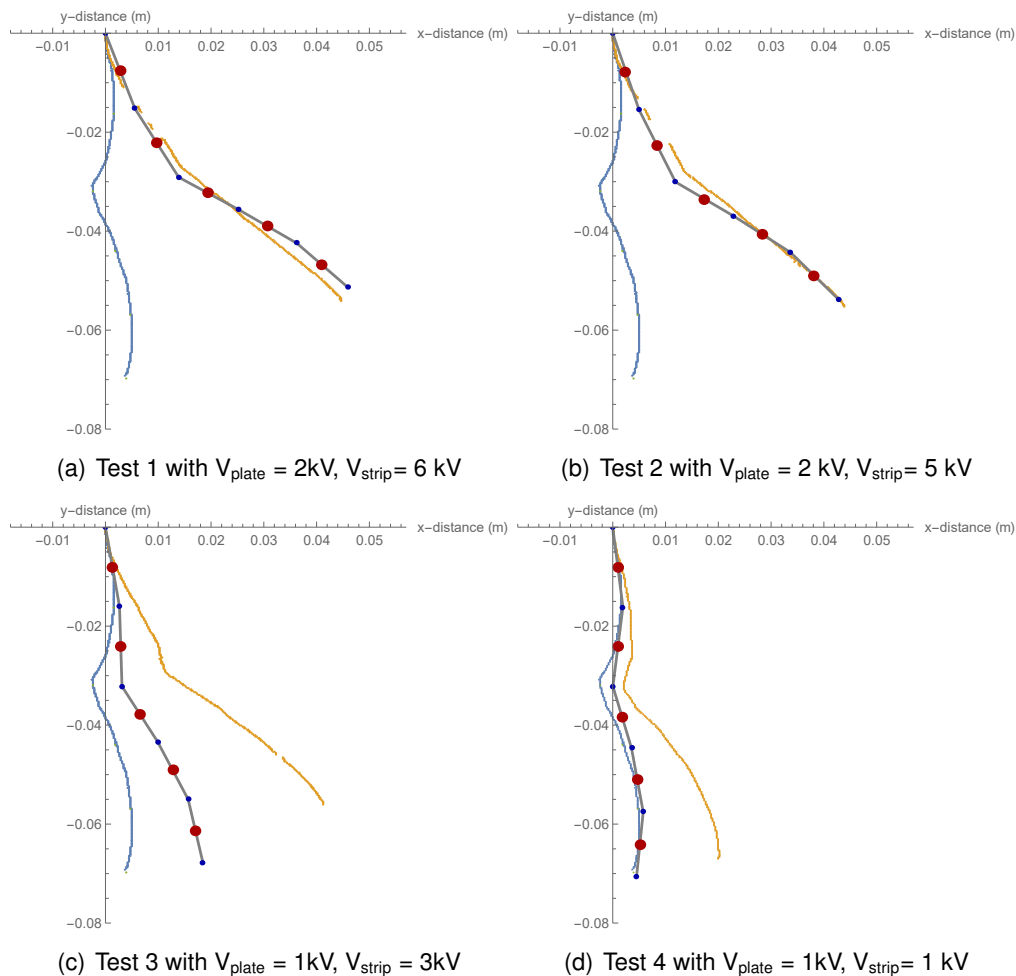| Test #	Plate Voltages (V)	Strip Voltages (V)
1	2000	6000
2	2000	5000
3	1000	3000
4	1000	1000

Two effects, illustrated in Figure 2.55, were observed and investigated which could be the

(a) Test 1 with V_{plate} = 2kV, V_{strip}= 6 kV

(b) Test 2 with V_{plate} = 2 kV, V_{strip}= 5 kV

(c) Test 3 with V_{plate} = 1kV, V_{strip} = 3kV

(d) Test 4 with V_{plate} = 1kV, V_{strip}= 1 kV

Figure 2.53: *Results of numerical simulations. The blue line represents initial, unforced wire shape while the yellow line represents steady-state experimental configuration. The gray line is the steady-state position calculated using the model described above. On this line, the red spheres represent the placement of the SMSM spheres as well as their actual radii, while the smaller, blue dots represent the hinges between each of the pendulums.*

cause of the modeling errors seen in Figures 2.53 and 2.54. Figure 2.55(a) shows that, under seemingly identical charging conditions, the strip feels different forces and torques. The yellow, right-most line represents the position of strip with V_{plate} = 1 kV and V_{strip} = 0 kV before the strip was charged. The lines to the left are its position under the same voltage settings after experiments in which the strip was charged to progressively higher voltages. This seems to indicate that the mylar, which is an insulator and therefore does not charge and discharge on the fast timescales upon which conductors do, was accumulating charge as consecutive experiments were performed. As the model did not account for this dielectric charging effect, it is unsurprising that Tests 2-4 deviate from experiments.

The second effect not accounted for in the model is the mutual capacitance of the strip and the plate. To illustrate how this occurs, consider the inverse of Eq. (2.145), but for three electrically
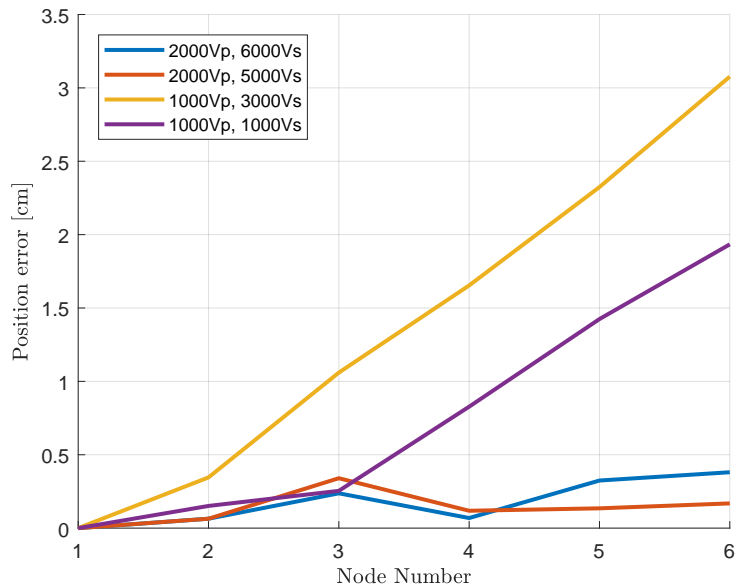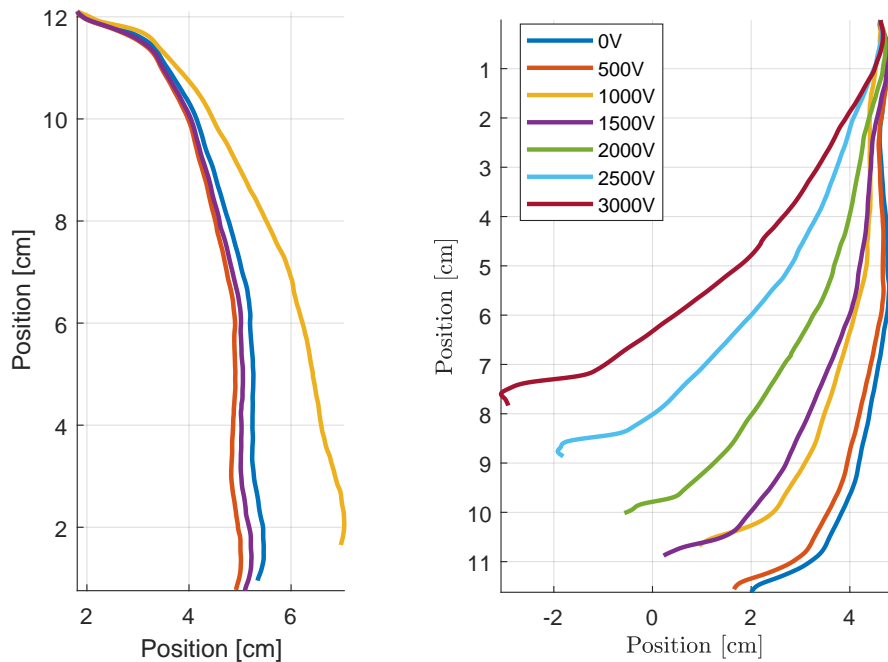
Figure 2.54: *Position difference between hinge positions between the model and experimental data for Tests 1-4*

(a) Position of experimental strip with V_{plate}= 1 kV, V_{strip} = 0 kV. The drift from the original test (yellow) to the left originated after successive charge cycles.

(b) Position of experimental strip with V_{plate} increased from 0 kV (far right) to 3 kV (far left) and V_{strip} = 0 kV.

Figure 2.55: *Indication of unmodeled physical phenomena of dielectric charging of the aluminized mylar strip as well as induced charging effects with the parallel plate capacitor generating the background electric field*

isolated spheres each charged by separate power supplies.

$$\begin{bmatrix} Q_1 \\ Q_2 \\ Q_3 \end{bmatrix} = \begin{bmatrix} C_{1,1} & C_{1,2} & C_{1,3} \\ C_{2,1} & C_{2,2} & C_{2,3} \\ C_{3,1} & C_{3,1} & C_{3,3} \end{bmatrix} \begin{bmatrix} V_1 \\ V_2 \\ V_3 \end{bmatrix} \tag{2.157}$$

It is immediately clear that even though there is no current flow between spheres, the charge Q_1 is dictated not only by its own voltage and capacitance but also by the proximity to the other two charged spheres.

$$Q_1 = C_{1,1}V_1 + C_{1,2}V_2 + C_{1,3}V_3 \tag{2.158}$$

While stray electric fields can be generated in the space environment due to plasma interactions, these are less common on Earth. Thus, this mutual capacitance effect can be mitigated, but not avoided in terrestrial experiments. Note in Eq. (2.158) that, if V_1 and V_2 are sufficiently small, $Q_1 \approx C_{1,1}V_1$.

For the case with the parallel plate capacitors, the plates are extremely large compared with the strip, meaning that the mutual capacitance is also large. This is why the majority of the experiments outlined in Table 2.13 have $V_{\text{strip}} > V_{\text{plate}}$. Note that Test 4 is fit most poorly by the model. This is in part because the charging due to mutual capacitance is large for that case.

Figure 2.55(b) shows deflection of the strip when grounded for various plate voltages. As the mutual capacitance between the strip and the plate is unknown and changes in time, this effect can't be incorporated into the model. Additionally, extremely low plate voltages necessitate excessive strip voltages to achieve significant shape change. This circumstance exacerbates the dielectric charging issue discussed previously. However the relative success of Tests 2 and 3 indicate that an object like aluminized mylar can be modeled with relative accuracy in certain circumstances.

2.3   Research Thrust 3: Dielectric Surfaces

2.3.1   Motivation

In the Geosynchronous Earth Orbit (GEO) regime, satellites charge to very high voltages sometimes as dramatic as -19 kV.[46] This charging causes small forces and torques on the body due to interactions with earth's magnetic field, which changes the orbits of some uncontrolled lightweight debris objects through the Lorentz force.[1,25,26,47] If nearby spacecraft use active charging such as electron and ion guns, larger forces and torques are felt between the crafts. This enables novel Coulomb formation flying missions.[48–50] These forces can also be used for touchless re-orbiting of GEO debris to its graveyard orbit in a matter of months using the Electrostatic Tractor (ET).[51] If a spacecraft has a non-symmetric charge distribution, it also experiences torques which can be harnessed for touchless de-spin before servicing or grappling.[21,52,53]

There are many separate challenges to electrostatic actuation such as prescribing the appropriate electron and/or ion beam current and voltage, sensing the voltage, position, and attitude of a passive space object, and designing control laws that perform well for either tugging or de-spinning. In order to design and implement stable and performant control laws in any of the above mission scenarios, accurate and fast methods are needed to predict the force and torque on both spacecraft using only in-situ measurements such as the voltage of each craft, and their relative separation and attitude. Accuracy is important because under or over prediction can seriously harm performance, or lead to a collision.[54] Speed is important because the force and torque must

be predicted in real time by the flight computer. This paper discusses how to predict electrostatic force and torque for a body that is composed of conductors and dielectrics as shown in Fig. 2.56.
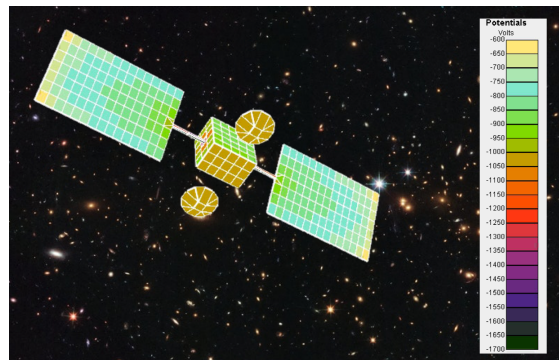

Figure 2.56: *Voltages of a spacecraft with conducting and dielectric surfaces. Computation done in NASCAP-2k*

There are many methods for force and torque prediction ranging from very accurate but much slower than realtime methods such as Finite Element Analysis (FEA), or faster and more scalable methods such as the Method of Moments (MoM)[13] or Boundary Element Method (BEM). Prior work explores using the Galerkin method to model forces between two dielectric spheres.[76] A relatively new scheme for electrostatic force and torque prediction is the Multi-Sphere Method (MSM).[3] MSM is very similar to the MoM in that an elastance matrix is populated and then inverted to find the charge distribution. The Coulomb force is applied from every discretized charge on one body to every discretized charge on the other body. MSM differs from MoM in that the elements of the elastance matrix are tuned to match force and torque created by a higher-fidelity method rather than from first principles. Because of this tuning, MSM can predict forces and torques with only a few percent error using only 3-4 spheres for a two craft system,[5,55] but requires a truth model from which to optimize. It is a robust method for force and torque prediction for conducting systems, however, not all spacecraft are continuously conducting. Recent work[77] investigates how to modify MSM to account for dielectrics and finds very small impacts when the dielectric lays directly on top of the conducting surface of the spacecraft.

Most spacecraft are built to be continuously conducting to avoid differential charging and arcing. However, some of the conducting covering may degrade with time and lose its conductivity. Two scenarios where this may occur is the coverglass coating on the solar panels and the Multi-Layer Insulation (MLI). Solar panels require a glass cover to protect from proton radiation, and there is usually a conductive clear coating over the glass, however, this coating may degrade or flake off and can leave sections of the non-conductive glass exposed. MLI also usually has a gold or aluminum coating, but this may flake off or otherwise degrade. Additionally, some spacecraft are not built fully conducting to begin with, and will have large dielectric portions. In the case of coverglass and MLI, there is a thin layer (10-100 μm) of dielectric sitting directly on top of a conductor connected to spacecraft ground. However, in an effort to save weight, some spacecraft have MLI wrapped around a skeleton frame with very little area of the MLI touching the conducting bus.

2.3.2 Method of Images Analysis

To gain some analytical insight into the first question of when dielectrics need to be accounted for, first consider a much simpler system using the Method of Images (MOI).[8,14,78] If a positive point

charge is held a distance z above a grounded infinite conducting plate, a negative induced charge will pool up beneath the point charge due to attraction. For the purposes of calculating the field above the plate, one can assume that there is a negative charge of equal magnitude z below the plate. In this situation, net charge is zero because the conductor "canceled out" the point charge.

If a finite sphere is considered rather than an infinite plate, the induced charge q' becomes smaller and moves closer to the surface. For a sphere with radius R, the induced charge is given by

$$q' = -\frac{R}{R+d}q \tag{2.159}$$

where d is the distance between the dielectric charge and the surface of the conductor, and Q_D is the dielectric charge as is shown in Fig. 2.57. When d is much smaller than R, the induced charge is nearly equal and opposite to the dielectric charge and will cancel out its effect on the total charge. However, when d is comparable to R, the effect of the dielectric charge on the total charge is much more significant.
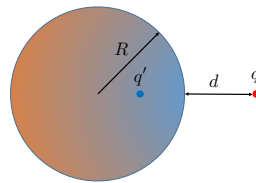

Figure 2.57: *Method of Images concept illustration*

There are many differences between the electric field in the vicinity of a point charge and conducting sphere, and the electric field in the vicinity of a charged solar panel and conducting spacecraft bus, but there is still some intuition to gain from this simple analysis. The MOI predicts that when the dielectric is very near the conductor, its charge will be mostly canceled out regardless of how charged it is. Dielectric coatings sitting directly over conductors will likely not cause any significant changes for this reason. If the dielectric is far from a conductor, like a solar panel might be, then the effects are more significant. To understand how this simple principle applies to more complex spacecraft, numerical studies are performed next.

2.3.3 Truth Model Development

The Method of Moments (MoM) is used to create a truth model of the electric field in the vicinity of the spacecraft for a simpler MSM model to match. Prior work[55] has found that MSM models that match the E field also match the force and torque very well, and matching E fields solves a number of other optimization issues as well.

This is done for four spacecraft under three separate charging conditions. The first spacecraft (Fig 2.58(a)) is a 3 m by 1 m box with a dielectric hovering 25.4 μm ($\sim$1 mil) above the top of the spacecraft. This serves as a model of the case where the MLI is stretched over the conducting exterior of the spacecraft. The small displacement off the surface is chosen to be a common thickness for MLI. The second spacecraft (Fig. 2.58(b)) is almost identical to the first but the top conductor is removed and the dielectric is shifted down to be flush so that it is stretched over the perimeter of the conductor like the surface of a drum. The third spacecraft (Fig. 2.58(c)) has three panels made of dielectric so that it has equal area of conductor and dielectric. The fourth and final spacecraft (Fig. 2.58(d)) is composed of 5 dielectric panels and a single conducting panel on the very bottom. All spacecraft are referred to with the shorthand "XcYd" where X is the number
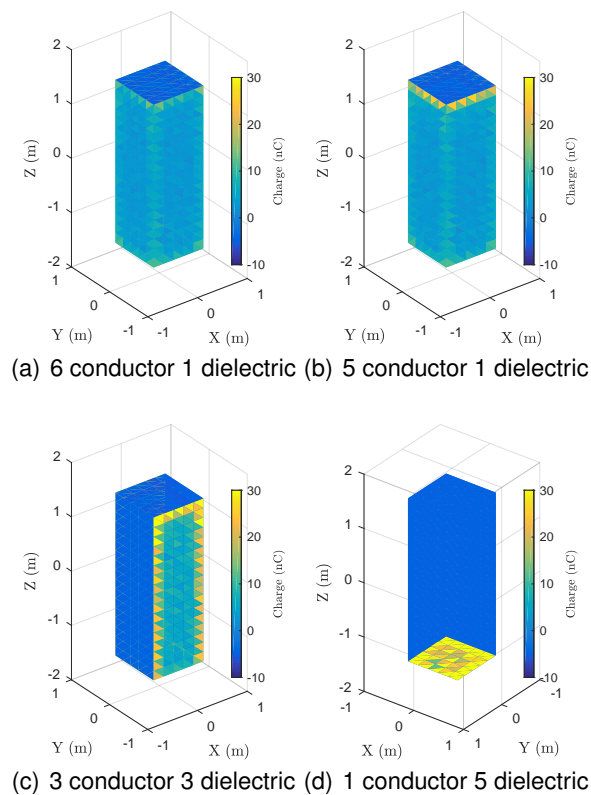
(a) 6 conductor 1 dielectric   (b) 5 conductor 1 dielectric

(c) 3 conductor 3 dielectric   (d) 1 conductor 5 dielectric

Figure 2.58: *Four template spacecraft truth models computed using the Method of Moments*

of conducting panels and Y is the number of dielectric panels, so the last spacecraft discussed can be indicated by 1c5d. These four spacecraft span the range from a small amount of dielectric completely on top of a conductor to almost all dielectric with very little conductor very far away.

In all subplots in Fig. 2.58 the conductor is charged to +30 kV and the dielectric to -250 nC/m^2. For some models (especially the 1c5d one), the peak charge per element goes up to 94 nC, but the color scale only extends up to 30 nC per element to better show the charge distribution. The positive charge concentrates near the negative dielectric in all cases. Consider the first two cases (Fig. 2.58(a) and Fig. 2.58(b)) which only differ by the inclusion of a conductor backing behind the dielectric. In the case without the backing, much more charge must accumulate on the side panels to cancel out the negative charge, while in the case with the backing all the charge accumulates on that backing and is not seen. The other two cases (Fig. 2.58(c) and Fig. 2.58(d)) have even more positive charge accumulate to cancel out the large negative panels.

In addition to solving for the charge distribution, the electric field in the vicinity of the spacecraft is also found. The E field is computed at 30 points uniformly spread across each of 12 different spherical shells ranging in radius from 3 to 25 meters. The E field is computed for 3 different cases as well - the first in which only the conductor is charged to +30 kV and the dielectric has no net charge (but has a high voltage due to its proximity to the dielectric), one in which the conductor is charged and the dielectric is additionally charged to -250 nC/m^2, and the last in which the conductor is grounded (0 V) and the dielectric is charged. These 30 points per shell across 12 different shells for 3 different charging scenarios for 4 different spacecraft represent 4320 individual E field computations.

2.3.4   Conductor Solutions

As a first attempt at modeling these spacecraft, the dielectric surfaces are ignored entirely and the optimization is done using a dataset where the dielectric is uncharged. This method has promise for the spacecraft with dielectrics close to conductors such as the 6c1d because of the image charges. A 3 sphere MSM model where all spheres are constrained to stay on the z axis, but can change their height and radius is optimized using only the conducting data for all spacecraft. The cost function is the average percent error of the E field the MSM model produces relative to the truth model. The final solution for the 3c3d spacecraft is shown in Fig. 2.59 with its three spheres constrained along the z axis. Since all three spheres have a tunable radius and height, there are 6 free parameters in this model.
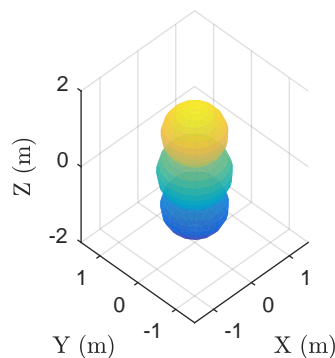

Figure 2.59: *Optimal MSM model for 3c3d spacecraft ignoring dielectrics*

This process of ignoring the dielectrics is applied to all four spacecraft and their performance in both the conducting and mixed charging regimes is shown in Fig. 2.60. All MSM models have only conducting spheres and are optimized using just the conducting dataset (+30 kV and no dielectric charge).

The performance of the 6c1d model is shown using a violin plot in Fig. 2.60(a). Violin plots are a good way to show a lot of data at once; they essentially show multiple histograms rotated by 90°. The width of each bar corresponds to the number of cases in the bin shown on the y axis for the case shown on the x axis. In the following violin plots, the cases correspond to how far away the E field is measured, the bins correspond to the percentage error (with reference to the MoM truth model), and the color corresponds to the charging scenario, with the dark blue being the conductor, (C) and the aqua being the mixed case (M). For the 6c1d spacecraft (Fig. 2.60(a)), the errors for the C and M case are incredibly similar, and both very good - they are almost always below 1% error, and after 10 m they are always better than 0.1% error. They are similar because the induced charge on the top plate of the conductor almost entirely cancels out the dielectric charge, making it as though the charged dielectric is not even there.

Moving to the 5c1d case (Fig. 2.60(b)), the conducting regime errors are almost unchanged, but the mixed charging regime errors are larger. This is because the two cases are no longer as similar due to the lack of a top conducting panel to cancel out the dielectric charge. Despite this, the conductor only model has only a few percent error in the M category, which is more than accurate enough for many missions. The 3c3d spacecraft (Fig. 2.60(c)) is slightly harder to model with mixed regime errors in the 10% range even though conductor errors are still very small. This is because much of the dielectric is much farther away from the conductor. Moving finally to the 1c5d case (Fig. 2.60(d)), the C errors are still very good, but the M errors have increased up to 200% error.
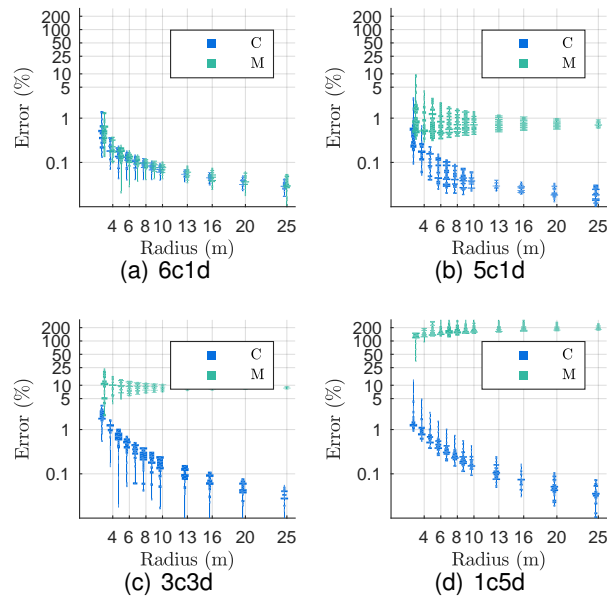
Figure 2.60: *Performance of a conductor-only MSM model in pure conducting (C) and mixed (M) charging regimes*

From this analysis, it seems that one would not bother to model dielectrics for the 6c1d or the 5c1d, but probably the 3c3d and definitely for the 1c5d. To expand this analysis to more continuous charging conditions, the dielectric charge density is swept from 1 - 1000 nC/m and voltage from 10V to 100 kV for each spacecraft. For each charging condition, compute the charge percentage error as $100 \left(Q_C - Q_T \right)/(Q_T)$ where Q_C is the total charge found if the dielectric is ignored and Q_T is the true total charge. This charge error correlates with the percentage error when computing force in the far field, and should be small to ensure accuracy. The charge error is always 100% when the voltage is zero because the conductor only solution will always predict $Q_C = 0$, even if the total charge Q_T is negligible. Thus, this method for judging the charge error can produce misleading results when the voltage is small. The charge errors are shown in Fig. 2.61 where the different colors indicate different spacecraft.
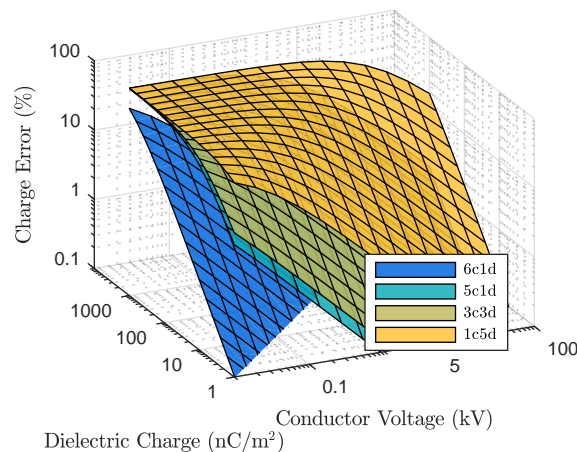

Figure 2.61: *Charge error as a function of voltage and dielectric charge density for four spacecraft*

In general, the charge errors grow as the dielectric charge is increased, which makes sense as the ignored charge becomes larger. The charge errors are also large when the voltage is low because they are percentage based. The 1c5d spacecraft has the worst errors, as expected since it is mostly dielectric, and has many panels which do not come close to the conductor. For this template spacecraft, errors will be large for almost all dielectric and conductor charge configurations. For the two intermediate spacecraft - the 3c3d and 5c1d, the performance is very similar. They both have charge errors larger than 10% if the dielectric charge is larger than 500 nC/m^2 when the voltage is 5 kV. The 6c1d spacecraft is the bounding case - neglecting dielectrics only introduces errors when the spacecraft is at very low voltages, at which the actual charge and resulting force and torque will be very small.

This manner of analysis can be used to quickly check if dielectrics ought to be considered in an analysis. First the self and mutual dielectric capacitances are found for the spacecraft in question. Next the voltage and dielectric charge ranges are found, and finally the charge error is computed for the voltage and dielectric charge ranges. If the charge error is higher than the acceptable error for that mission, dielectrics must be included. This answers the first question "when ought dielectrics to be considered?" Now, how best to model dielectrics is considered.

2.3.5   Dielectric MSM Methodology

Dielectrics charge on much slower timescales than conductors because of their large mutual capacitance. Because of this, they are treated as known point charges rather than a known voltages. To modify conducting MSM to include dielectrics, the model is broken into two parts for the conductor and dielectric:

$$\begin{bmatrix} \boldsymbol{V}_C \\ \boldsymbol{V}_D \end{bmatrix} = \begin{bmatrix} S_C & S_M \\ S_M^T & S_D \end{bmatrix} \begin{bmatrix} \boldsymbol{Q}_C \\ \boldsymbol{Q}_D \end{bmatrix} \tag{2.160}$$

where the C and D subscripts denote conductor and dielectric respectively, and the M is for mutual. Since the voltage of the conductor and the charge of the dielectric are assumed known and the charge distribution for the conductor is sought, the top line of this equation is rearranged to give

$$\boldsymbol{Q}_C = [S_C]^{-1}(\boldsymbol{V}_C - [S_M]\boldsymbol{Q}_D) \tag{2.161}$$

Then the total charge $\boldsymbol{Q}$ can be formed as $\boldsymbol{Q} = [\boldsymbol{Q}_C, \boldsymbol{Q}_D]^T$. The force, torque, or E field are then computed as discussed in the earlier section.

When modeling conducting bodies, the MSM optimization problem is fairly simple - change the position and size of the spheres to best match the force, torque, or E field from a truth model. With dielectrics, there are a few changes - now there are both conducting spheres and point charges which may be moved, and there are many different charging scenarios to consider when producing the truth model. With conductors, it does not matter what voltage is chosen for the truth model, as long as it is not zero. With dielectrics included, models that work well for a high voltage case can perform very poorly for a high charge case.

To address the problem of optimizing for just one charging regime, three charging scenarios are included in the truth file; one with just the conductor charged and no charge on the dielectric, one with both conductor and dielectric charged, and one with just the dielectric charged. Because using many point charges does not greatly slow down computation time, and to make the optimization easier, the point charges are uniformly distributed over the dielectric panels. This scheme is shown in Fig. 2.62.
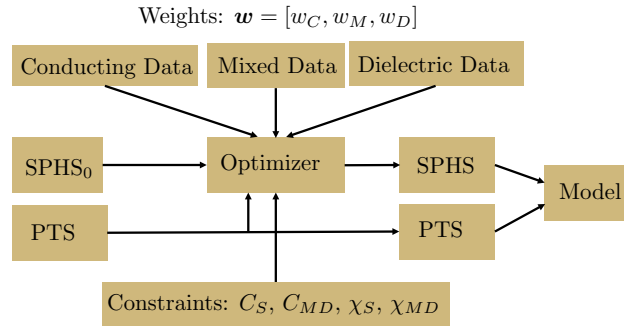
Weights: $\boldsymbol{w} = [w_C, w_M, w_D]$

Figure 2.62: *Optimization scheme for dielectric MSM*

An initial guess for the spheres location and radius is supplied to the optimizer. The optimizer uses the points model along with the spheres model to compute the E field at all 30 points in all of the 12 shells for all 3 charging scenarios. The cost is computed from the average percentage error for all three charging scenarios and the weights. A selection of constrains, discussed later, can also be used to ensure behavior in the far field. The final spheres model is combined with the prescribed points model to make the full model for that spacecraft.

2.3.6 Optimization Constraints

Prior work in optimizing MSM models for conductors[5, 55] has shown that enforcing that the MSM model have the same self capacitance as the object being modeled can make the optimization more robust and also provides a guarantee of correctly modeling the force in the far field. The self capacitance is a scalar parameter that determines how much charge is present at a given voltage. For a spacecraft with both dielectric and conducting components, the total charge is a function of both the conductor voltage and the dielectric charge. The total charge is the sum of the dielectric charge and the conductor charge:

$$Q = \mathbb{1}_{n_C}^T \boldsymbol{Q}_C + \mathbb{1}_{n_D}^T \boldsymbol{Q}_D \tag{2.162}$$

where the notation $\mathbb{1}_n$ indicates a column vector of ones with n elements and n_C and n_D denote the number of conducting and dielectric elements. Now substitute in Eq. (2.161) for $\boldsymbol{Q}_C$ and rearrange:

$$\begin{aligned}Q &= \mathbb{1}_{n_C}^T [S_C]^{-1} (\boldsymbol{V}_C - [S_M]\boldsymbol{Q}_D) + \mathbb{1}_{n_D}^T \boldsymbol{Q}_D \\ &= C_S V_C + C_{MD} Q_D\end{aligned} \tag{2.163}$$

where the self capacitance C_S and mutual dielectric capacitance C_{MD} are defined as

$$C_S \equiv \mathbb{1}_{n_C}^T [S_C]^{-1} \mathbb{1}_{n_C} \tag{2.164}$$

$$C_{MD} \equiv (1 - \mathbb{1}_{n_C}^T [S_C]^{-1} [S_M] \mathbb{1}_{n_D}^T / n_D) \tag{2.165}$$

The self capacitance determines how sensitive the total charge is to the voltage on the conductor, and the mutual dielectric capacitance determines how sensitive the total charge is to the dielectric charge. If $C_{MD} = 1$, then adding charge to the dielectric adds exactly that much to the total charge. If $C_{MD} = 0$, then adding charge to the dielectric adds no charge at all to the total charge because the induced charge cancels it out. Referencing back to the MOI solution $C_{MD} \approx 1 - R/(R + d)$. So when the dielectric is close to the conductor $(d << R)$, C_{MD} will be close to zero, and the

dielectrics will have minimal effects. When the dielectric is far from the conductor ($d \sim R$), C_{MD} will be close to one and dielectrics will play a larger role. Unlike the self capacitance which has units of Farads, C_{MD} is dimensionless and is always between 0 and 1.

The total charge is 0th order moment of the charge distribution. The first order moment of the charge distribution is the dipole ($\boldsymbol{q}$). The dipole is a 3×1 vector formed by multiplying the total charge by a vector pointing from the center of the coordinate system (usually at the center of mass) to the center of the charge and is discussed in greater detail in Reference.[17] MSM models that match the total charge and the dipole will correctly predict the torque as well as the force in the far field.

For a MSM model with both dielectric and conducting parts, the dipole is a combination of the dipole from both the dielectric and conducting portions:

$$\boldsymbol{q} = \boldsymbol{\chi}_S V + \boldsymbol{\chi}_{MD} Q_D \tag{2.166}$$

where the parameters $\boldsymbol{\chi}_S$ and $\boldsymbol{\chi}_{MD}$ are the self and mutual susceptibilities defined by:

$$\boldsymbol{\chi}_S \equiv [R_C][S_C]^{-1}\mathbb{1}_{n_C} \tag{2.167}$$

$$\boldsymbol{\chi}_{MD} \equiv \frac{[R_D]\mathbb{1}_{n_D}}{n_D} - \frac{[R_C][S_C]^{-1}[S_M]\mathbb{1}_{n_D}}{n_D} \tag{2.168}$$

where $[R_C]$ and $[R_D]$ are matrices containing the location of every sphere/point in an MSM model or the centroid of every triangle in a MoM model for both the conductor and dielectric:

$$[R] = \begin{bmatrix} x_1 & \ldots & x_N \\ y_1 & \ldots & y_N \\ z_1 & \ldots & z_N \end{bmatrix} \tag{2.169}$$

The self susceptibility determines how sensitive the total dipole is to the conductor voltage, and the mutual susceptibility determines how sensitive it is to the dielectric charge. If the mutual susceptibility is small, the charge on the dielectric will not influence the dipole strongly. Once again the units differ because the two susceptibilities multiply different quantities.

These four parameters, $C_S, C_{MD}, \chi_S,$ and $\chi_{MD},$ are all intrinsic and unchanging properties of a given spacecraft geometry. These constraints are enforced during optimization to understand how they affect the performance. Since these four constrains can be enforced in groups, there are 16 different unique sets of constraints that can be used. For each constraint set, the MSM solution is optimized for the 3c3d spacecraft using a prescribed points model for the dielectric which uses 36 points and a seven sphere MSM model which has 3 spheres on each of the conductor panels and one along the central axis.

The results are shown in Fig. 2.63. The MSM solution for one of the 16 cases is shown in Fig. 2.63(a). This particular optimization was constrained to match the self capacitance and self susceptibility, but not either of the mutual terms. The performance of this model is shown as a triple violin plot in Fig. 2.63(b). The errors for all three scenarios decreases with distance, dropping below 1% at around 10 m for the dielectric case and near 7 m for the conductor and mixed case. The maximum error is near 10% but that is only for the dielectric only case at the closest distance. Since it would be tedious to show a triple violin plot for each of the 16 different constrain cases, the performance is reduced to two scalar values - first the cost function which is the mean of the errors for each field point at each radius and each charging condition. This value is shown for all of the 16 constraint cases in Fig. 2.63(c).

The first thing to notice is that the errors are all very good regardless of the constraints used. The maximum mean error is 1.35%, which is less than all the other uncertainties in the system are

likely to be. The lowest error is found with no constrains at all, which is expected as the optimizer has access to more solutions than the constrained solutions. In general, the leftmost and third-from-left columns are similar to each other and darker than the rest, indicating that the optimizer picks MSM models that match self capacitance even if that constraint is not enforced. The first and third rows also have lower error than the other rows, especially when combined with the first and third columns. This indicates that C_S and χ_S are the most important parameters to match. Looking at the outside edge near the upper left corner shows the effects of including just one constraint at a time. No constraints at all gives a mean error of 1.11 %, just χ_S gives 1.14 %, χ_{MD} gives 1.16 %, C_{MD} gives 1.17 %, and C_S gives the same 1.11%. This analysis of looking at the constraints one at a time supports the idea that C_S and χ_S are the most important parameters to match.

(a) MSM solution matching C_S and χ_S

(b) MSM solution perfomance

	None	C_{MD}	C_S	Both
None	1.11	1.17	1.11	1.20
χ_{MD}	1.16	1.21	1.18	1.19
χ_S	1.14	1.22	1.15	1.28
Both	1.23	1.29	1.24	1.35

First-order constraints / Zeroth-order constraints

(c) Mean Error

	None	C_{MD}	C_S	Both
None	0.18	0.31	0.17	0.28
χ_{MD}	0.17	0.27	0.17	0.27
χ_S	0.12	0.28	0.12	0.26
Both	0.17	0.26	0.17	0.26

First-order constraints / Zeroth-order constraints
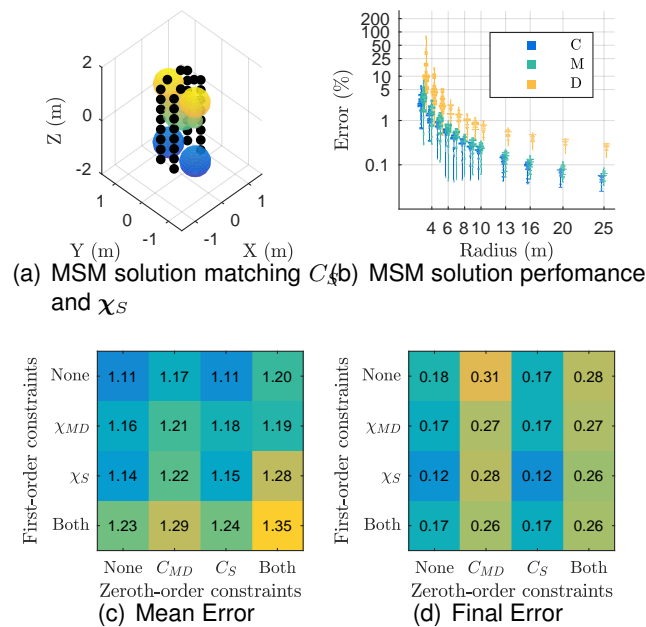
(d) Final Error

Figure 2.63: *Effects of enforcing constraints*

The second scalar value to draw from the violin plots is the mean error for all charging conditions at 25 meters. This final error should be more sensitive to enforcing constraints due to its distance and is shown in Fig. 2.63(d). The first and third column are even more dramatically better than the rest than in the mean error, as is the third row. Here, the lowest error comes from enforcing the self susceptibility constraint either with or without the self capacitance. The mean and final error analysis both show that C_S and χ_S are the most important constraints to enforce for this spacecraft. Enforcing both only hurts the mean error by 0.04%, and provides a guarantee of performance in the far field.

This particular seven sphere, 36 point model has 8 free parameters, which makes it possible to enforce any combination of constraints and still have many free parameters to tune for optimality. Despite this, it is still a very difficult optimization requiring very precise initial conditions. For more simple MSM models with fewer free parameters, it is not possible to enforce all of these constraints depending on the number of free parameters. It is also possible that the constrains are not compliant for some MSM models — for example a MSM model that had all spheres constrained on the z axis would never be able to match any non-zero x and y components of χ_S. For this model, constraints aid the solution since they are compliant. For other models, they are detrimental or impossible to enforce.

2.3.7   Performance and Time Analysis

The earlier section investigated the effect of constraints while keeping the model (3c3d spacecraft with 7 spheres and 36 points) constant. This section uses no constraints, but investigates the E field fitting performance while changing the spacecraft and its sphere and points model. For all spacecraft, the points are distributed equidistantly across the dielectric panels as shown in Fig. 2.63(a). This model has two rows which results in 36 points, one row gives in 11 points while 3 rows will give 75 points. For dielectric-heavy spacecraft (such as the 1c5d) there are naturally many more points than for conductor-heavy spacecraft (such as the 6c1d).

For all spacecraft, the spheres model uses a few spheres placed either along the z axis or in the plane of the conducting panels. The simplest model uses two spheres where both spheres have variable radii and position along the z axis. The next most complicated model has 3 spheres with variable radii and height for 6 total parameters. More advanced models have one sphere free to move along the z axis and a few rings of spheres centered on the panels that can change height and radius. Fig. 2.63(a) shows a model for the 3c3d spacecraft with three rings of spheres along the vertical panels and one central sphere along the z axis for a total of seven spheres. For the 1c5d spacecraft, none of the above models work well, so 1, 4, and 5 sphere models are made which keep all spheres in the $z = -1.5$m plane. In total, 10 separate sphere and 9 separate point models are considered for a total of 53 optimizations which are shown in Fig. 2.64. If no points are used, the dielectric dataset is ignored because it will always give 100% error.
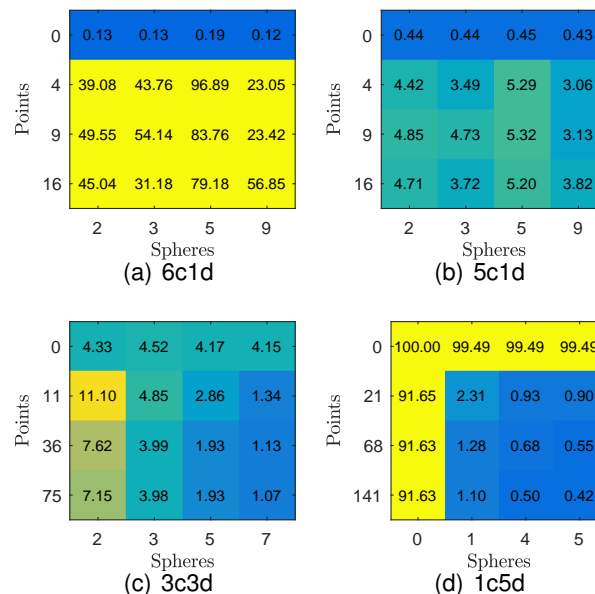

Figure 2.64: *Mean error of E field fitting for different sphere and point models*

The first plot (Fig. 2.64(a)) shows how well different designs model the E field surrounding the 6c1d spacecraft. Earlier analysis found that dielectrics did not need to be modeled, and this analysis confirms that and additionally finds that that adding points actually hurts the solution. If no points are used, the mean errors are all less than 0.2%, but if points are added they jump up to at least 20% and sometimes almost 100%. Among the conductor-only solutions, there is very little variation, with more spheres helping in general except for the 5 sphere model.

Moving to the 5c1d spacecraft (Fig. 2.64(b)), adding points still makes the solution worse but not by as much as the 6c1d. Ignoring the dielectric gets errors near 0.5%, but including them gets

errors near 5%. In general, more spheres helps, with the exception of the 5 sphere model, which appears to be an all-around bad model regardless of the number of points used on both the 6c1d and 5c1d spacecraft. For both of these spacecraft, one ought to ignore the dielectrics entirely.

The 3c3d spacecraft (Fig. 2.64(c)) has equal area of conductor and dielectric and has slightly smoother behavior. Ignoring dielectrics results in mean errors near 4%, and including them can either help or hurt this solution. For instance, including points makes the solution nearly 3 times worse for a two sphere model, but nearly 3 times better for a 7 sphere model. For any models with more than 3 spheres, dielectrics ought to be included. Except for the first row, more spheres and points both help the solution. Since the columns are more distinct than the rows, one can conclude that the number of spheres is more important than the number of points, although the jump from 0 to 11 and 11 to 36 points is significant.

Finally, the 1c5d spacecraft mean error is shown in Fig. 2.64(d). Since this spacecraft is virtually all dielectric, a points only solution is also considered. Both the points and only spheres cases preform poorly with errors near 100%. For the cases with both spheres and points, the errors are much better, and decreases as spheres and points are added. In contrast to the 3c3d spacecraft, the rows are just as distinct as the columns, which indicates that adding points for this spacecraft is more valuable than on the 3c3d, which makes sense since the dielectric is larger and plays a larger part in the E field.

Overall, the two spacecraft for which dielectrics ought not be included are the easiest to model with errors always less than 0.5%. The 3c3d spacecraft provides an intermediate case where the number of spheres being used determines whether points ought to be used. For all spacecraft, a model exists which keeps the average error below 1.5%, which is likely lower than other errors expected in the system.

Many of the proposed applications of electrostatic force modeling must evaluate quickly as well as accurately. To investigate the trade space between accuracy and time, the number of arithmetic operations needed is found. For an MSM model with n conducting spheres and m dielectric point charges, the number of operations N required to find the charge at each node (using Eqn. (2.161)) is

$$N = \frac{2}{3}n^3 + \frac{11}{2}n^2 - \frac{25}{6}n + 2mn \qquad (2.170)$$

if using Gauss-Jordan elimination for the matrix inverse.

This measure is not the full number of computations that must occur to compute the electrostatic force or torque, but is the most time-intensive step. All other steps will involve the number of points and spheres in both models and are therefore more difficult to include without introducing unnecessary complexity.

The mean error function is plotted in Fig. 2.65 for all spacecraft and all models as a function of operations, which are a proxy of computer time. The small numbers indicate which model is used – a pair of i, j indicates a model with i spheres and j points, and the color indicates the spacecraft. For the 6c1d and 5c1d spacecraft, only the conductor-only solution is shown since the others have poor performance. For the other two spacecraft, all the designs are shown with lines indicating models with the same number of spheres. Additionally, a boundary line and shading is used to indicate the likely Pareto front.

It is now clear that the 3c3d spacecraft is the least accurate, but still has mean error below 10% for all but one design. The 1c5d spacecraft follows a much tighter boundary and is more accurate while requiring roughly the same computational effort. Lastly, the two conductor only spacecraft are not strong functions of the computational effort but are very accurate no matter which model
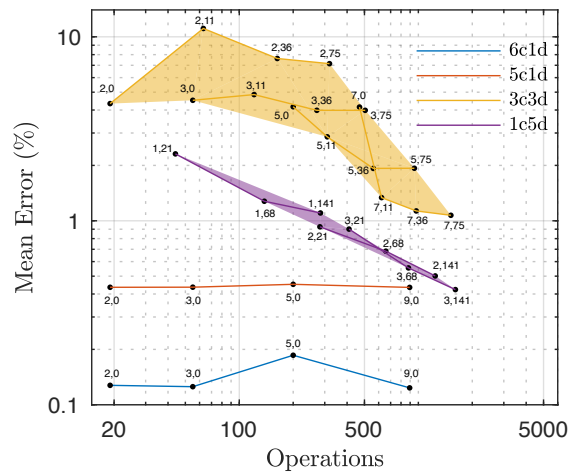
Figure 2.65: *Mean error for all spacecraft as a function of arithmetic operations*

is used. This plot, or others like it, could be used to decide which model to use for a particular mission with known accuracy and speed constraints.

Chapter 3

Project Conclusions

The 3-year project successfully developed novel electrostatic force and torque models that are very fast to numerically evaluate and suitable to model electrostatic disturbances. The spacecraft geometry is represented through a series of body-fixed conducting spheres using a technique called the Multi-Sphere Method or MSM. The work entailed analytical, numerical and experimental components. A new E-field matching technique provided a more robust Volume MSM or VMSM which was applied to general three-dimensional shapes. The technique performed very well, and we are able to demonstrated that if two objects are separated by at least 2-3 craft radii, the VMSM technique provides very accurate electrostatic force and torque approximations with errors less than 1-2%. The key insight is that even with very non-spherical shapes using 2-3 MSM spheres is often sufficient to reach such accuracies.

A non-numerical electrostatic modeling approach called the Appropriate Fidelity Models (AFMs) was developed as well. The electrostatic fields are expanded in a manner related to the multi-pole method, but setup for a multi-spacecraft configuration. These formulations provide analytical insight into the coupled multi-body forces and torques and were compared to earlier electrostatic force models developed based on experimental and numerical data. However, the computational efficiency was found to be less then the MSM models studied in this project. These models were applied to high area-to-mass ratio objects, illustrating for the first time how the electrostatic torques can create large departures on the order of 100s of kilometers. However, this perturbation is also shown to be very sensitive to the initial orientation, as well as the exact center of charge location. This information would be very challenging to obtain for actual space objects.

The Surface MSM or SMSM model assumes that the spacecraft surface is populated with a homogenous distribution of equal spheres. This results in a higher number of spheres being used compared to the VMSM technique, but it can provide much higher E-force modeling accuracies if the craft are within 2-3 craft radii. This is of interest for high-fidelity modeling requirements, as well as docking and close proximity operations. The project compared the SMSM technique to the Method of Moments (MoM) method and shows how they are related. The SMSM approach can provide a simpler setup technique if MoM tools are not available, and provides better accuracy versus speed results. In particular, using MoM a mathematical foundation is provided that justifies when the original homogenous SMSM technique is justified. Further, a new heterogeneous SMSM technique is developed, as well as some hybrid SMSM-MoM techniques.

The original MSM concept was developed with the assumption that the the spacecraft has a conducting outer surface, as well as a rigid shape. The study successfully relaxed both of these assumptions by considering MSM models with time varying shapes or dielectric surface components. To include dielectric surface components the MoM solver was custom developed for

this project to generate a truth model to compare against the MSM solutions. The dielectric charge densities are modeled through a series of point charges. Key results of this study include when dielectric begin to significantly impact the E-force approximations, and when they can be ignored. The dielectric MSM is studied for a prototype spacecraft shape where the surfaces are varied to be either conducting or dielectric.

To account for time varying shapes a modified MSM formulation is hypothesized. Here the surface is decomposed into a sequence of connected surface components. Each surface element then has a MSM developed for it whose sphere locations are locked relative to this surface element. As the surface deforms, the element MSM spheres thus move in a known manner. This study demonstrates that this flexible MSM approach can successfully approximate the E-field about a time varying shape by comparing the models to analytical answers. The fidelity can be tuned with either the number of surface elements, as well as the order of the MSM model of an element. The flexible MSM models were tested in vacuum chamber electrostatic deflection experiments using charged aluminum coated Mylar sheets. The thin mylar sheet proved to be a very challenging time varying structure to test. These objects represent our best understanding of HAMR or High Area to Mass Ratio geosynchronous objects. With these experiments we were able to determine that while the kilo-volt levels of charging can cause shape changes, we also observed electron discharge events that cause sharp deflections. This illustrated just how complex the challenge is to numerically simulate the electrostatic forces on such objects. The discharge behavior is subject to the edge properties, as well as the dielectric mylar material between the aluminum coated outer surfaces.

Thus, the 3-year project completed the original goals on time and on budget. The MSM models will be very useful in future research that studies charged astrodynamics and how charging can perturb space object motion. Further, these models are also enabling new techniques being developed to touchlessly measure the potential, as well as possibly the material properties, of a neighboring space object using the surface response to electron radiation. The MSM models allow us to implement faster-than-realtime modeling to study such systems, but also can be used in the sensor processing technique.

Bibliography

[1] Hughes, J. and Schaub, H., "Charged Geosynchronous Debris Perturbation Using Rapid Electromagnetic Force and Torque Evaluation," *Advanced Maui Optical and Space Surveillance Technologies Conference*, Maui, Hawaii, Sept. 20–23 2016.

[2] Stevenson, D. and Schaub, H., "Optimization of Sphere Population for Electrostatic Multi Sphere Model," *IEEE Transactions on Plasma Science*, Vol. 41, No. 12, Dec. 2013, pp. 3526–3535, doi:10.1109/TPS.2013.2283716.

[3] Stevenson, D. and Schaub, H., "Multi-Sphere Method for Modeling Electrostatic Forces and Torques," *Advances in Space Research*, Vol. 51, No. 1, Jan. 2013, pp. 10–20, doi:10.1016/j.asr.2012.08.014.

[4] Smythe, W. R., *Static and Dynamic Electricity*, McGraw–Hill, 3rd ed., 1968.

[5] Chow, P., Hughes, J., Bennett, T., and Schaub, H., "Automated Sphere Geometry Optimization For The Volume Multi-Sphere Method," *AAS/AIAA Spaceflight Mechanics Meeting*, Napa Valley, California, Feb. 14–18 2016, pp. 2223–2240, Paper No. AAS-16-472.

[6] Schaub, H., "Faster-than-Realtime Electrostatic Force and Torque Modeling for SSA Applications," AFOSR Annual Report, University of Colorado, Aerospace Engineering Sciences Department, Boulder, CO, September 14 2016.

[7] Maxwell, J., *A Treatise on Electricity and Magnetism*, Oxford University Press, 1893.

[8] Lekner, J., "Electrostatics of two charged conducting spheres," *Proceedings of the Royal Society of London A: Mathematical, Physical and Engineering Sciences*, Vol. 468, No. 2145, 2012, pp. 2829–2848, doi:10.1098/rspa.2012.0133.

[9] Bauer, R., "Distriubtion of Points on a SPhere with Applicaiton to Star Catalogs," *AIAA Journal of Guidance, Control, and Dynamics*, Vol. 23, No. 1, 2000, pp. 130–137, doi:10.2514/2.4497.

[10] Grafarend, E., ENgles, J., and Varga, P., "The temporal variation of the spherical and Cartesian multipoles of the gravity field: the generalized MacCullagh representation," *Journal of Geodesy*, 2000.

[11] Hou, X., Scheeres, D. J., and Xin, X., "Mutual potential between two rigid bodies with arbitrary shapes and mass distributions," *Celestial Mechanics and Dynamical Astronomy*, 2016, pp. 1–27.

[12] Scheeres, D. J., *Orbital Motion in Strongly Perturbed Environments*, Springer, Berlin, 2012.

[13] Gibson, W. C., *The method of moments in electromagnetics*, Chapman & Hall, November 28 2007.

[14] Jackson, J. D., *Classical Electrodynamics*, John Wiley & Sons, 1999.

[15] Price, S. L., Stone, A. J., and Alderton, M., "Explicit Formulae for the Electrostatic Energy, Forces and Torques between a Pair of Molecules of arbitrary symmetry," *Molecular Physics*, Vol. 52, No. 4, 1984, pp. 987–1001, doi:10.1080/00268978400101721.

[16] Hughes, J. and Schaub, H., "Appropriate Fidelity Electrostatic Force Evaluation Considering a Range of Spacecraft Separations," *AAS/AIAA Spaceflight Mechanics Meeting*, Napa Valley, California, Feb. 14–18 2016, pp. 3417–3434, Paper No. AAS-16-486.

[17] Hughes, J. and Schaub, H., "Spacecraft Electrostatic Force And Torque Expansions Yielding Appropriate Fidelity Measures," *AAS Spaceflight Mechanics Meeting*, San Antonio, TX, Feb. 5–9 2017, Paper AAS 17–441.

[18] Griffiths, D. J., *Introduction to Electrodynamics*, Prentice Hall, 3rd ed., 1999.

[19] Schaub, H. and Junkins, J. L., *Analytical Mechanics of Space Systems*, AIAA Education Series, Reston, VA, 4th ed., 2018, doi:10.2514/4.105210.

[20] Giancoli, D. C., *Physics for Scientists and Engineers*, Pearson Prentice Hall, 2008.

[21] Bennett, T. and Schaub, H., "Touchless Electrostatic Three-Dimensional Detumbling of Large GEO Debris," *Journal of Astronautical Sciences*, Vol. 62, No. 3, Sept. 2015, pp. 233–253, doi:10.1007/s40295-015-0075-8.

[22] Fennell, J. F., Koons, H. C., Leung, M., and Mizera, P., "A review of SCATHA satellite results: Charging and discharging," Tech. report, Space Division Air Force Systems Command, Los Angeles Air Force Station, Aug. 1985.

[23] Mullen, E. G., Gussenhoven, M. S., Hardy, D. A., Aggson, T. A., and Ledley, B. G., "SCATHA Survey of High-Voltage Spacecraft Charging in Sunlight," *Journal of Geophysical Research*, Vol. 91, No. A2, 1986, pp. 1474–1490, doi:10.1029/JA091iA02p01474.

[24] Ferguson, D., Hoffmann, R., Cooper, R., and Hughes, J., "1997-2002 Solar Array String failures revisited," *Journal of Spacecraft and Rockets*, Vol. 54, No. 3, 2017, pp. 542–553.

[25] Früh, C., Ferguson, D., Lin, C., and Jah, M., "The Effect of Passive Electrostatic Charging on Near-Geosyncronous High Area-To-Mass Ratio Objets," *International Astronautical Congress*, Vol. 64, 2013.

[26] Paul, S. N. and Früh, C., "Space Debris Charging and its Effect on Orbit Evolution," *Journal of Guidance, Control, and Dynamics*, Vol. 0, 2017, pp. 1–19.

[27] Hughes, J. and Schaub, H., "Rapid Charged Geosynchronous Debris Perturbation Modeling of Electrodynamic Disturbances," *Journal of Astronautical Sciences*, Vol. 65, No. 2, 2018, pp. 135–156, doi:10.1007/s40295-017-0127-3.

[28] Schildknecht, T., Muscia, R., Plonera, M., Beutlera, G., Fluryb, W., Kuuselac, J., de Leon Cruzd, J., and de Fatima Dominguez Palmerod, L., "Optical observations of space debris in GEO and in highly-eccentric orbits," *Advances in Space Research*, 2004, pp. 901–911.

[29] Wiesel, W. E., "Estimating Nongravitational Accelerations on High Area-to-Mass Ratio Objects," *AIAA Journal of Guidance, Control, and Dynamics'*, Vol. 39, No. 6, 2016, pp. 1438–1443, doi:10.2514/1.G001464.

[30] Schildknecht, T., Musci, R., Frueh, C., and Ploner, M., "Color Photometry and Light Curve Observations of Space Debris in GEO," *Procedings of the Internaitonal Astronautical Congress*, 2008.

[31] Dever, J. A., de Groh, K. K., Townsend, J. A., and Townsend, J. A., *Mechanical Properties Degradation of Teflon FEP returned from the Hubble Space Telescope*, American Institute of Aeronautics and Astronautics, 1998.

[32] Davis, V. and Mandell, M. J., "Plasma Interactions with Spacecraft. Volume 2, NASCAP-2K Scientific Documentation for Version 4.1," Tech. report, Science Applications International Corp, 2011.

[33] Denton, M., Thompsen, M., Jordanova, V., Henderson, M., Borovsky, J., Denton, J., Pitchford, D., and Hartley, D., "An empirical model of electron and ion fluxes derived from observations at geosynchronous orbit," *AGU Space Weather*, Vol. 13, 2015, pp. 233–249.

[34] Lin, Y. and Joy, D. C., "A New Examination of Secondary Electron Yield Data," *Surface and Interface Analysis*, Vol. 57, 2005, pp. 895–900.

[35] Lai, S. T., *Fundamentals of Spacecraft Charging: Spacecraft Interactions with Space Plasmas*, Princeton University Press, 2011.

[36] Balcon, N., Payan, D., Belhaj, M., Tondu, T., and Inguimbert, V., "Secondary Electron Emission on Space Materials: Evaluation of the Total Secondary Electron Yield From Surface Potential Measurements," *IEEE Transactions on Plasma Science*, Vol. 40, No. 2, 2012.

[37] Finckenor, M., "Multilayer Insulation Material Guidelines," Tech. report, NASA Marshall Space Flight Center, 1999.

[38] Wie, B., *Space Vehicle Dynamics and Control*, AIAA Education Series, Reston, VA, 2nd ed., 2008.

[39] Tsyganenko, N. A., "A Magnetospheric magnetic field model with a warped tail current sheet," *Planetary and Space Science*, Vol. 37, 1989, pp. 5–20.

[40] Volland, H., "A semiemperical Model of Large-Scale Magnetospheric Electric Fields," *Journal of Geophysical Research*, Vol. 78, No. 1, 1973.

[41] Stern, D. P., "the Motion of a Proton in the Equatorial Magnetosphere," *Journal of Geophysical Research*, Vol. 90, No. 4, 1975.

[42] Korth, H., Thomsen, M. F., Borovsky, J. E., and McComas, D. J., "Plasma sheet access to geosynchronous orbit," *Journal of Geophysical Research*, Vol. 104, No. A11, 1999, pp. 25047–25062, doi:10.1029/1999JA900292.

[43] Chen, N. M. A., "Isolated Cold Plasma Regions: Observations and Their Relation to Possible Production Mechamisms," *Journal of Geophysical Research*, Vol. 80, No. 7, 1975.

[44] Bhavnani, K. H. and Vancour, R., "Coordinate Systems for Space and Geophysical Applications," Tech. report, Phillips Laboratory, Air Force Systems Command, 1991.

[45] Gómez, N. O. and Walker, S. J., "Eddy currents applied to de-tumbling of space debris: Analysis and validation of approximate proposed methods," *Acta Astronautica*, Vol. 114, 2015, pp. 34–53, doi:10.1016/j.actaastro.2015.04.012.

[46] Olsen, R. C., "The record charging events of ATS-6," *Journal of Spacecraft and Rockets*, Vol. 24, No. 4, 1987, pp. 362–366.

[47] Hughes, J. and Schaub, H., "Space Weather Influence on Electromagnetic Geosynchronous Debris Perturbations Using Statistical Fluxes," *Space Weather*, Vol. 16, No. 4, 2018, pp. 391–405, doi:10.1002/2017SW00176.

[48] Berryman, J. and Schaub, H., "Analytical Charge Analysis for 2- and 3-Craft Coulomb Formations," *AIAA Journal of Guidance, Control, and Dynamics*, Vol. 30, No. 6, Nov.–Dec. 2007, pp. 1701–1710, doi:10.2514/1.23785.

[49] Hogan, E. and Schaub, H., "Collinear Invariant Shapes for Three-Craft Coulomb Formations," *Acta Astronautica*, Vol. 12, March–April 2012, pp. 78–89, doi:10.1016/j.actaastro.2011.10.020.

[50] Inampudi, R. and Schaub, H., "Optimal Reconfigurations of Two-Craft Coulomb Formation in Circular Orbits," *AIAA Journal of Guidance, Control, and Dynamics*, Vol. 35, No. 6, Nov. – Dec. 2012, pp. 1805–1815, doi:10.2514/1.56551.

[51] Schaub, H. and Moorer, D. F., "Geosynchronous Large Debris Reorbiter: Challenges and Prospects," *The Journal of the Astronautical Sciences*, Vol. 59, No. 1–2, 2014, pp. 161–176, doi:10.1007/s40295-013-0011-8.

[52] Bennett, T., Stevenson, D., Hogan, E., McManus, L., and Schaub, H., "Prospects and challenges of touchless electrostatic detumbling of small bodies," *Advances in Space Research*, Vol. 56, No. 3, Aug. 2015, pp. 557–568, doi:10.1016/j.asr.2015.03.037.

[53] Bennett, T. and Schaub, H., "Capitalizing On Relative Motion In Electrostatic Detumbling Of Axi-Symmetric Geo Objects," *6th International Conference on Astrodynamics Tools and Techniques (ICATT)*, Darmstadt, Germany, March 14–17 2016.

[54] Hogan, E. and Schaub, H., "Relative Motion Control for Two-Spacecraft Electrostatic Orbit Corrections," *AIAA Journal of Guidance, Control, and Dynamics*, Vol. 36, No. 1, Jan. – Feb. 2013, pp. 240–249, doi:10.2514/1.56118.

[55] Ingram, G., Hughes, J., Bennett, T., Reilly, C., and Schaub, H., "Autonomous Volume Multi-Sphere-Model Development Using Electric Field Matching," *AAS Spaceflight Mechanics Meeting*, San Antonio, TX, Feb. 5–9 2017, Paper AAS 17-451.

[56] Stevenson, D., *Remote Spacecraft Attitude Control by Coulomb Charging*, Ph.D. thesis, University of Colorado Boulder, 2015.

[57] Harrington, R., *Field Computation by Moment Methods*, Wiley IEEE, 1968.

[58] Alad, R. H. and Chakrabarty, S., "Electrostatic Analysis of an Artificial Orbiting Satellite for Absolute Charging," *IEEE Transactions on Plasma Science*, Vol. 43, No. 9, September 2015, pp. 2887 – 2893.

[59] Balsami Karthikeyan, V. K. H. and Sanyal, S., "Estimation of Free Space Capacitance and Body Potential of a Spacecraft for Charging Analysis," *IEEE Transactions on Plasma Science*, Vol. 41, No. 12, December 2013, pp. 3487 – 3491.

[60] Chakrabarty, S., "Absolute charging analysis of space-craft bodies using method of moments (MoM)," *IEEE Applied Electromagnetics Conference (AEMC)*, 2015, doi:doi: 10.1109/AEMC.2015.7509140.

[61] Mehta, P. D. and Chakrabarty, S. B., "Capacitance of Dielectric-Coated Metallic Bodies Isolated in Free Space," *Electromagnetics*, Vol. 31, No. 4, 2011, pp. 294 – 314.

[62] Reitan, D. K. and Higgins, T. J., "Accurate Determination of the Accurate Determination of the Capacitance of a Thin Rectangular Plate," *Transactions of the American Institute of Electrical Engineers, Part I: Communication and Electronics*, Vol. 75, No. 6, 1957, pp. 761–766.

[63] Chow, Y. and Yovanovich, M., "The shape factor of the capacitance of a conductor," *Journal of Applied Physics*, Vol. 53, No. 8470, 1986.

[64] Schaub, H. and Jasper, L. E. Z., "Orbit Boosting Maneuvers for Two-Craft Coulomb Formations," *AIAA Journal of Guidance, Control, and Dynamics*, Vol. 36, No. 1, Jan. – Feb. 2013, pp. 74–82, doi:10.2514/1.57479.

[65] Cover, J. H., Knauer, W., and Maurer, H. A., "Lightweight Reflecting Structures Utilizing Electrostatic Inflation," US Patent 3,546,706, October 1966.

[66] Stiles, L. A., Schaub, H., Maute, K., and Moorer, D. F., "Electrostatic Inflation of Membrane Space Structures," *AAS/AIAA Astrodynamics Specialist Conference*, Toronto, Canada, Aug. 2–5 2010, AIAA-2010-8134.

[67] Stiles, L. A., Schaub, H., Maute, K. K., and Moorer, D. F., "Electrostatically inflated gossamer space structure voltage requirements due to orbital perturbations," *Acta Astronautica*, Vol. 84, Mar.–Apr. 2013, pp. 109–121, doi:10.1016/j.actaastro.2012.11.007.

[68] Paul, S. N. and Früh, C., "Space Debris Charging and its Effect on Orbit Evolution," *AIAA/AAS Astrodynamics Specialist Conference*, Long Beach, CA, Sept. 12–15 2016.

[69] Früh, C., Ferguson, D. C., Lin, C., and Jah, M. K., "The effect of passive electrostatic charging on near-geosynchronous high area to mass ratio objects," *64th International Astronautical Congress*, Sept. 23–27 2013, Paper No. IAC-13-A6.2.8.

[70] Channumsin, S., Ceriotti, M., Früh, C., and Radice, G., "Orbital Dynamics of Lightweight Flexible Debris," *64th International Astronautical Congress*, Sept. 23–27 2013, Paper No. IAC-13-A6.2.7.

[71] Bennett, T. and Schaub, H., "Electrostatically Charged Spacecraft Formation Estimation Using Linearized Relative Orbit Elements," *AAS Spaceflight Mechanics Meeting*, San Antonio, TX, Feb. 5–9 2017, Paper AAS 17–483.

[72] Engwerda, H., Hughes, J., and Schaub, H., "Remote Sensing for Planar Electrostatic Characterization using the Multi-Sphere Method," *Final Stardust Conference*, ESTEC, Nederland, Oct. 31 – Nov. 4 2016.

[73] Jackson, J. D., "Charge density on thin straight wire , revisited Charge density on thin straight wire , revisited," *American Journal of Physics*, Vol. 789, No. 68, 2000, doi:10.1119/1.1302908.

[74] Thomas, T., "The Capacitance of an Anchor Ring," *Australian Journal of Physics*, Vol. 7, 1954, pp. 347, doi:10.1071/PH540347.

[75] Maxwell, J. and Schaub, H., "Applicability Of The Multi-Sphere Method To Flexible One-Dimensional Conducting Structures," *AAS/AIAA Astrodynamics Specialist Conference*, Stevenson, WA, Aug. 20–24 2017, Paper No. AAS-17-618.

[76] Feng, J. Q., "Electrostatic interaction between two charged dielectric spheres in contact," *Physical Review E*, Vol. 62, No. 2, 2000.

[77] Hughes, J. and Schaub, H., "Effects of Charged Dielectrics on Electrostatic Force and Torque," *International Workshop on Spacecraft Formation Flying*, 2017.

[78] Metzger, P. and Lane, J., "Electric Potential Due to a System of Conducting Spheres," *The Open Applied Physics Journal*, Vol. 2, 2009, pp. 32–48.